Spring 1-1-2012

Dust Aerosols Investigated Using an Integrated Microphysical- Climate-Radiation Model

Lin Su
University of Colorado at Boulder, sul@colorado.edu

Dust Aerosols Investigated Using an Integrated Microphysical-Climate-Radiation Model

by

Lin Su

B.S., Nanjing Institute of Meteorology, 1997

M.S., Institute of Atmospheric Physics, 2000

A thesis submitted to the

Faculty of the Graduate School of the

University of Colorado in partial fulfillment

of the requirements for the degree of

Doctor of Philosophy

Department of Atmospheric and Oceanic Sciences

2012

This thesis entitled:

Dust Aerosols Investigated Using an Integrated Microphysical-Climate-Radiation Model

written by Lin Su

has been approved for the Department of Atmospheric and Oceanic Sciences

_____

Dr. Owen B. Toon

_____

Dr. Cora E. Randall

Date: _____

The final copy of this thesis has been examined by the signatories, and we find that both the content and the form meet acceptable presentation standards of scholarly work in the above mentioned discipline.

Su, Lin (Ph.D., Atmospheric and Oceanic Sciences)

Dust Aerosols Investigated Using an Integrated Microphysical-Climate-Radiation Model

Thesis directed by Professor Owen B. Toon

I have developed a three-dimensional coupled microphysical-climate-radiation model based on the National Center for Atmospheric Research (NCAR) Community Atmospheres Model (CAM3.0 and CAM5.0) and the University of Colorado/NASA Community Aerosol and Radiation Model for Atmospheres (CARMA2.3 and CARMA3.0). The model has been used to investigate the sources, removal processes, transport, optical properties, and radiative effects of Asian dust aerosols on climate.

In the initial project, a A Weibull distribution is implemented to estimate the sub-grid scale wind speed variability. The dust AOD agrees well with AERONET data and the timing of dust events is comparable to the National Institute for Environmental Studies (NIES) lidar data in Beijing and Nagasaki.

In the second project, the simulated properties of atmospheric dust from the Saharan deserts and the Asian deserts are compared using data from CALIPSO and AERONET during 2006 and 2007. In my model the yearly horizontal dust flux just downwind of the African dust source is about 1088 Tg (10S-40N, 10W) and from the Asian dust source it is about 355 Tg (25N-55N, 105E) in 2007. I find the difference in dust flux is mainly due to the larger area over which dust is lifted in Africa than Asia. However, Africa also has stronger winds in some seasons. Some previous studies suggested that the observed descent of Saharan dust is due to sedimentation of the particles, but my work and satellite data show instead it is dominated by meteorology. I find the size distributions of Asian and African dust are similar when the dust is lifted,

but the mode size can differ and secondary size modes can develop probably due to differences in vertical wind velocities during transport.

The importance of the uncertainty in the single scattering albedo (SSA) to the radiative effects of dust on the climate of China is explored in my final project through two case studies based on the modeled and observed solar diffuse fluxes/irradiances at the surface. We employ Mie theory and the refractive indices of Shi et al. (2005) as an initial case, but then scale the refractive indices to consider more absorbing aerosols as suggested in Ge et al. (2011). The different SSA based on the scattering theory over East Asia are derived, which directly result in negative (case-Shi) or positive (case-Ge) shortwave fluxes at the Top of the Atmosphere (TOA). The shortwave heating rates in the atmosphere are also different due to dust radiative forcing. The integrated three-dimensional microphysical-climate-radiation model used in this study allows us to consider interactions with the local surface albedo and emissivity, evolution of the size distribution in time, the vertical distribution of the dust as well as transport of dust aerosols vertically and horizontally.

Acknowledgements

After I got my master degree in Atmospheric Sciences in 2000, I decided to travel around and stay at home. When my daughter was 1 year old in 2005, I decided to go back to school for my PhD study in Atmospheric Sciences. Then one day I tried to send an email to the Chair of the Department of Atmospheric and Oceanic Sciences (ATOC) in University of Colorado at Boulder, Dr. Owen B. Toon, but I didn't expect any response. However, I got the response very soon and was encouraged to apply the ATOC PhD program if I am interested in it. I appreciate that Dr. Toon always respects others no mater what status they are. As my PhD advisor, Dr. Toon has been a great example for me not only on the enthusiasm, insights, and deep knowledge on Atmospheric Sciences, but also on how to be a nice and responsible person in the society. He not only sees the bright sides of his students, but also points out the issues that should be improved and how to improve them in a way you feel comfortable. I appreciate that Dr. Toon has been always responding to my emails promptly and has always had time to discuss my research with me. I also appreciate that Dr. Toon has supported me for numerous conferences and seminars that provide a better chance for me to communicate with other scientists from all over the world.

I also want to thank my group people, especially Chuck Bardeen, Tianyi Fan, and Pengfei Yu, who have helped me on the coupled microphysical-climate-radiation model for my PhD study. I want to thank Jason English, who is one-step ahead of me for defense and work, and has provided lots of useful information and made the processes easier than it would have been without him. Many thanks also go to Laurie, Susan, and Caroline from ATOC and LASP, who have kindly assisted me as needed during my PhD study and defense.

The discussion with the following scientists during my PhD study has helped me at the early stage of my research: Peter Colarco, Atsushi Shimizu, Zhaoyan Liu, and Tao Zhang. Thanks to Paul Ginoux for sending the globally distributed soil erodibility factor to me. The discussions with all of my following PhD committee members are very inspiring and supportive: Andrew Gettelman, Gregory Frost, David Noone, Cora Randall, Peter Pilewiske (Former), and Tomas Warner (Former).

I appreciate the friendship with Jill, Shelley, and Stephanie. I learned from them to look for the positives in everything you do and see. This has helped me in my PhD study and will continue to affect me in my future life. I also appreciate my kindly neighbors, who have provided me free babysitting whenever I need their help.

Finally, I give my thanks to my family. My mother and mother-in-law are two great ladies, whose endless love to their children and family has encouraged me in my PhD study. Thanks for your support, Tao! Thanks for the power you give to me, Gracie!

This project is partly supported by the NASA Earth and Space Science Fellowship Program-Grant 10-Earth10R-10. NSF grants ATM—0856007 also supported this work, as did the CALIPSO science team under NN07AR13G. The CALIPSO program data were obtained from the NASA Langley Research Center Atmospheric Science Data Center. I want to thank AERONET staff for establishing and maintaining the sites used in this investigation of the AERONET data. I would like to acknowledge high-performance computing support provided by NCAR's Computational and Information Systems Laboratory, sponsored by the National Science Foundation.

CONTENTS

List of Tables

List of Figures

Chapter 1

Introduction

Mineral dust is an important component of atmospheric pollution [VanCuren, 2003] and affects climate through its impact on the radiation budget [Sokolik and Toon, 1996; Kaufman et al., 2001]. The mineral dust mass flux from Asia is about 100-200 Tg per year, which is approximately 10% of the total annual global dust emissions [IPCC, 2001]. IPCC [2007] reported about 800 Tg/year of Asian dust emissions, of which 30% is removed very near the dust sources and 70% is subject to regional and long-range transport. The Taklamakan and Gobi Desert are the two major sources of Asian dust emissions [Uno et al., 2005]. Asian dust can be transported over global scales [Clarke et al., 2001; Grousset et al., 2003]. Satellite images (such as from SeaWiFS and MODIS) often reveal dust plumes being transported over intercontinental distances [Husar et al., 2001; Hsu et al., 2006]. Thus Asian dust affects the regions downwind of the dust sources, such as the populated areas of China, Japan and Korea. Studies also have shown that Asian dust influences elevated sites in the Western United States [VanCuren, 2003].

Dust plays an important role in the atmospheric global circulation (Dunion and Velden, 2004; Wu, 2007), air pollution (Prospero, 1999; VanCuren, 2003), biogeochemical processes (Duce et al., 1991; Martin et al., 1994; Shinn et al., 2000), radiative budget (Sokolik and Toon, 1996; Kaufman et al., 2001), and human health (IPCC, 2007). Dust varies over short time scales and geologic time (Rea et al., 1985).

Numerous model simulations of Asian dust storms have been conducted over the past two decades and several limitations have been identified based on comparisons of the existing modeling results and observations. For example, simulations with a regional scale meteorology and dust transport model applied to Asia have indicated the difficulty in

capturing the timing and magnitude of known dust events [Uno et al., 2005]. A comparison of eight dust emission/transport models over Asia showed great discrepancies among the models of the dust emission fluxes over Asian dust source regions (e.g., Taklamakan Desert and Mongolia) [Uno et al., 2006]. Uno et al. [2006] also indicated the modeling of dust transport and deposition processes between China and Japan needs to be improved and a better understanding of dust long-range transport is needed.

My goal in the first part of this study is to use our best understanding of dust emission, transport, and deposition processes to simulate the downwind distributions of Asian dust using a new numerical model that combines a three-dimensional coupled climate model (CAM3) [Collins et al., 2004] and a microphysical model (CARMA2.3) [Toon et al., 1988; Jensen et al., 1994; Ackerman et al., 1995]. We test this new model primarily against data on the dust optical properties, such as aerosol optical depth (AOD), single scattering albedo (SSA), and vertical extinction, which are essential to properly simulate the aerosol impact on Earth's radiation budget and climate. Our focus here is primarily on in situ data. We plan a later comparison with satellite observations, many of which are not available for the time frame of this study.

In the first part of this study, I use a three-dimensional coupled climate model (CAM3) and a microphysical model (CARMA2.3) [Bardeen et al., 2008] to simulate the evolution of the mineral dust aerosols primarily during the fourth Aerosol Characterization Experiments (ACE-Asia field campaign). I run CAM3 in an offline mode in this study. Several dust transport models have been used to investigate the dust aerosols from the ACE-Asia field campaign [e.g., Chin et al., 2003, 2004; Uno et al., 2002, 2004; Carmichael et al., 2003; Gong et al., 2003; Shimizu et al., 2004]. CAM3 has previously been used to study dust transport, in the context of climate simulations using a small number of size bins [Mahowald et al., 2006]. The sectional aerosol model (CARMA2.3) allows us to define as many particle size bins as needed. The model is

driven by assimilated meteorology from the NCEP/NCAR reanalyses [Kalnay et al., 1996]; that is, the model is driven by observed wind fields to study the real-time Asian dust storm events. We validate the simulations against observations from ACE-Asia [Huebert et al., 2003].

We incorporate the Ginoux et al. [2001] dust source scheme into the coupled CAM3/CARMA2.3 model. The Ginoux et al. [2001] dust source function is one of a class of dust lifting schemes in which the dust vertical emission rate is parameterized in terms of the wind speed [Tegen and Fung, 1994; Mahowald et al., 1999; Ginoux et al., 2001]. Another type of model parameterizes the dust vertical flux in terms of friction velocity [Marticorena et al., 1997; Schulz et al., 1998; Zender et al., 2003a]. These dust emission schemes account for the dust particle size distribution and also parameterize dust emission by the saltation-sandblasting process. Saltation is the process that initiates a bouncing motion of coarse particles (the saltators) along the ground. These particles are too large to be suspended, but they eject smaller particles. The latter process is called sandblasting [Gomes et al., 1990; Shao and Raupach, 1993; Alfaro et al., 1997; Alfaro et al., 1998; Shao and Lu, 2000; Alfaro and Gomes, 2001; Grini and Zender, 2004]. We modified the Ginoux et al. [2001] dust source function by replacing the 10-m wind speed with the friction velocity, which is directly related to the surface wind stress that controls mineral dust lifting. We also account for various factors important in sandblasting, such as soil moisture.

The Saharan desert is the largest and most continuous dust source in the world. Saharan dust can be transported across the tropical North Atlantic and into the Caribbean region as well as into Europe (Prospero and Carlson, 1972; Prospero, 1996; Colarco et al., 2002; Colarco et al., 2003a,b; Toon, 2003; Liu et al., 2008; Generoso et al., 2008). Especially in summer large amounts of Saharan dust are transported across

the Atlantic Ocean, which is dominated by the Azores High, and arrive in the Caribbean Sea (Doherty et al., 2008).

The Taklimakan and Gobi deserts are the major dust sources in Asia (Uno et al., 2005). Asian dust can be transported over the North Pacific Ocean and reach Midway and North America (Duce et al., 1980; Shaw, 1980; Betzer et al., 1988; Clarke et al., 2001; Husar et al., 2001; Tratt et al., 2001; Huang et al., 2008; Eguchi et al., 2009; Su and Toon, 2009). Asian dust also can be transported over global scales (Clarke et al., 2001; Grousset et al., 2003; Uno et al., 2009).

In the second part of this study, we refer to all of the major dust lifting regions in Africa and Asia as Saharan or Asian deserts. These dust lifting regions for Asia can be seen from the dust flux maps given in Su and Toon (2009).

Recently, special attention has been paid to Saharan dust in field campaigns such as the Puerto Rico Dust Experiment (PRIDE) (Reid et al., 2002; Reid et al., 2003b; Maring et al., 2003; Colarco et al., 2003a,b), the Dust And Biomass EXperiment (DABEX) (Osborne et al., 2008), the SAharan Mineral dUst experiMent (SAMUM) (Heintzenberg, 2008; Knippertz et al., 2008; Muller et al., 2008), the African Monsoon Multidisciplinary Analysis (AMMA) (Rajot et al., 2008; Heese and Wiegner, 2008; Haywood et al., 2008), and the GERB Intercomparison of Longwave and Shortwave radiation (GERBILS) (Haywood et al., 2005; Marsham et al., 2008). Saharan dust has been studied through model simulations (Marticorena et al., 1997; Colarco et al., 2002; Colarco et al., 2003a,b; Maring et al., 2003; Liu et al., 2008; Generoso et al., 2008), and satellite retrievals (Liu D. et al., 2008; Liu Z. et al., 2008b; Generoso et al., 2008; Cuesta et al., 2009).

Several field campaigns have been also conducted regarding Asian dust aerosols including the Aerosol Characterization Experiments (ACE-Asia) (Huebert et al., 2003; Seinfeld et al., 2004), the Indian Ocean Experiment (INDOEX) (Ramanathan et

al., 2001, Rasch et al., 2001]), the TRAnsport and Chemical Evolution over the Pacific experiment (TRACE-P) (Carmichael et al., 2003; Jacob et al., 2003), the Intercontinental Chemical Transport Experiment Phase B (INTEX-B) (Arellano et al., 2007; McKendry et al., 2008), and the PACific Dust EXperiment (PACDEX) (Stith et al., 2008). Asian dust also has been investigated through model simulations (Tegen and Fung, 1994; Schulz et al., 1998; Mahowald et al., 1999, 2006; Ginoux et al., 2001; Uno et al., 2002, 2004, 2008, 2009; Carmichael et al., 2003; Chin et al., 2003, 2004; Gong et al., 2003; Zender et al., 2003a; Shimizu et al., 2004; Shao and Dong, 2006; Huang et al., 2009; Su and Toon, 2009), and satellite retrievals (Huang et al., 2007; Huang et al., 2008; Liu et al., 2008; Uno et al., 2008).

Most studies have focused on either Saharan dust or Asian dust. Here we investigate the differences and similarities in dust lifting, dust removal processes, seasonal variations, transport mechanisms, and physical properties between Saharan dust and Asian dust using satellite data such as CALIPSO, ground-based data such as AERONET, and numerical models.

Numerous satellite observations have been made of Saharan and Asian dust. Here we focus on data from the Cloud-Aerosol Lidar and Infrared Pathfinder Satellite Observation (CALIPSO). CALIPSO was launched in April 2006 (Liu et al., 2006; Winker et al., 2007). The Cloud –Aerosol Lidar with Orthogonal Polarization (CALIOP), on CALIPSO, is a two-wavelength (532 and 1064 nm), polarization-sensitive (at 532 nm) instrument. CALIOP provides substantial and unique information on vertical and geographical distributions of clouds and aerosols. CALIOP conducts nearly continuous observations of height-resolved attenuated backscatter over the globe (Sassen 2000; Winker et al., 2003; Winker et al., 2010).

The Aerosol Robotic NETwork (AERONET) is a globally distributed remote sensing aerosol-monitoring network of ground-based sun photometers that measure sun

and sky radiances in 16 spectral channels (340-1640 nm) (Holben et al., 1998). AERONET provides observations of aerosol optical depth (AOD), inversion products such as size distribution and single scattering albedo, and precipitable water. We use the cloud-screened and quality-assured AERONET Level 2.0 data in this study (Smirnov et al., 2000).

Numerical modeling of dust aerosols is essential for climate studies, and to better understand the behavior of the dust aerosols in the atmosphere. We use a coupled three-dimensional climate-microphysical sectional model, which is capable of simulating the mineral dust aerosols (Su and Toon, 2009) to explore the differences between atmospheric dust from the Saharan deserts and from the Asian deserts.

The various observations and models have led to a number of questions about Asian and African dust. It is clear from satellite observations that the dust optical depth is generally larger over the Atlantic, than over the Pacific. Is this difference due to more dust being lifted over Africa, to more dust being removed over the Pacific, to seasonality in dust lifting, or to other factors? Is the size distribution of dust downwind of African or Asian dust sources different, or the same so that it can be modeled using the same dust source functions? Are the dust optical properties different between Asian and African dust, and if so are the differences related to dust composition, or to particle size? Do the same mechanisms control dust transport in the two regions of the world? For instance, Saharan dust is observed to descend when crossing the Atlantic. Is this descent due to sedimentation, so Asian dust should also descend, or to air motions which may differ? Does the different meteorology of Africa and Asia lead to differences in the vertical distribution of the two types of dust? We seek to answer these questions in the second part of this study.

East Asia has high aerosol optical depths that result partly from air pollution, and partly from desert dust. In the third part of this study, we explore the role that dust plays

in the climate and radiation budget of China, and the surrounding countries. There are large uncertainties in estimating the radiative effects of dust on climate. Dust affects both the longwave and shortwave radiation because dust particles are relatively large. The net radiative forcing could be either negative or positive depending on the surface albedo, dust vertical distribution, and various optical properties of dust aerosols (Liao and Seinfeld, 1998). Dust generation responds to changes in weather and climate since wind speed and soil moisture are critical in controlling dust lifting. Likewise, it is possible that weather and climate may respond to dust amount. We use a microphysical-climate-radiation model to attempt to limit some of these uncertainties and gain a better understanding of the role of dust in the climate of China.

Several studies have previously considered the effects of dust on the radiation budget of China, and have identified the single scattering albedo (SSA) as especially critical to quantifying the radiation budget. Huang et al. (2009) used data from Cloud-Aerosol Lidar and Infrared Pathfinder Satellite Observations (CALIPSO) and Cloud and the Earth's Energy Budget Scanner (CERES) to constrain radiative transfer calculations and found the net radiative heating rate could reach 5.5 K day^{-1} at 5 km with a typical value of 1-3 K day^{-1} in dust layers over the Taklimakan desert in Asia. They also found that the net radiative forcing at the top of the atmosphere (TOA) was positive (warming) and that longwave radiation contributed two-thirds of the radiative forcing. About 90% of the atmospheric warming was contributed by shortwave radiation. There were the similar radiative effects at the surface where longwave warming offset about one third of the shortwave cooling.

Huang et al.'s (2009) conclusion that TOA net forcing is positive depends on assuming a relatively low value of SSA of about 0.89 at a wavelength of 0.67 um over the Taklimakan desert. Ge et al. (2011) used ground-based instruments to determine that the single scattering albedo was about 0.83, which is even lower than suggested by

Huang etal. (2009). These SSA values are much lower than suggested in previous studies of desert dust around the world. Forster et al. (2007) suggested a global mean SSA of 0.96 for desert dust based on spectrally dependent, simultaneous remote and in situ observations. Dubovik et al. (2002) gave an average SSA of 0.95 at 0.67um based on long-term AERONET observations over the Saharan desert. Mikama et al. (2006) suggested a SSA value of 0.93 over the Asian desert during the Aeolian Dust Experiments on Climate (ADEC). Su and Toon (2011) used a small set of AERONET observations to suggest the SSA of the Saharan dust may be about 0.035 lower than Asian dust. The values in the study of Su and Toon (2011) at 0.67 μm were about 0.96 for Asian dust. However, the single scattering albedo is wavelength dependent and reaches much lower values below 0.5 μm. All these relatively high SSA will result in different shortwave radiative forcing compared with Huang et al. (2009) and Ge et al. (2011).

An alternative approach to determining the SSA instead of using optical observations, is to use wavelength dependent refractive indices measured for dust samples together with scattering theory to determine the SSA for different sized particles. Generally, climate models use this approach since the radiative properties are usually not available for all possible circumstances. For example, the SSA is directly dependent on dust size distributions that vary in space and time. Dust optical properties are very sensitive to small dust particles (0.1-1.0 um diameter) because of their larger scattering and absorbing cross sections per unit mass relative to large particles (Claquin et al., 1998; Seinfeld and Pandis, 1998). Su and Toon (2009, 2011) reproduced observed dust size distributions using the coupled climate-microphysical model, CAM3/CARMA2.3, with 16 dust size bins having central radius covering the range from 0.1 to 10 μm. Using refractive indices from AERONET observations, the computed

wavelength dependent SSA were close to those derived by AERONET. Claquin et al. (1998) argued that using the refractive indices for a few wavelength or using wavelength averaged ones would bring large errors in calculating radiative fluxes so computing wavelength dependent values is important. The refractive indices depend on composition, which can vary between various regions (Sokolik and Toon, 1996; Claquin et al., 1998; Shi et al., 2005). Shi et al. (2005) provided an updated dataset of refractive indices for a wide spectral range (about 0.1 to 100 μm) representing East Asia dust based on the dust collected from the Taklimakan desert. Shi et al. (2005) used a simple single radiative-convective model to simulate dust radiative fluxes with specified dynamics and surface albedo. Their size distribution and refractive indices yield SSA near 0.94, which is on the high side of the range that is suggested by observations.

In the third part of this study, I explore the importance of the uncertainty in the SSA to the radiative effects of dust on the climate of China. I employ Mie theory and the refractive indices of Shi et al. (2005) as an initial case, but then scale the refractive indices to consider more absorbing aerosols as suggested in Ge et al. (2011). The integrated three-dimensional microphysical-climate-radiation model used in this study allows us to consider interactions with the local surface albedo and emissivity, evolution of the size distribution in time, the vertical distribution of the dust as well as transport of dust aerosols vertically and horizontally.

Chapter 2

Numerical Simulations of Asian Dust Storm Using a Coupled Climate-Aerosol Microphysical Model

2.1 Introduction

This chapter focuses on modeling the emission, transport, removal, and optical properties of dust aerosols over Asian area. The work has been published as Su and Toon (2009). Mineral dust is an important component of atmospheric pollution [VanCuren, 2003] and affects climate through its impact on the radiation budget [Sokolik and Toon, 1996; Kaufman et al., 2001]. The mineral dust mass flux from Asia is about 100-200 Tg per year, which is approximately 10% of total annual global dust emissions [IPCC, 2001]. IPCC [2007] reported about 800 Tg/year of Asian dust emissions, of which 30% is removed very near the dust sources and 70% is subject to regional and long-range transport. The Taklamakan and Gobi Desert are the two major sources of Asian dust emissions [Uno et al., 2005]. Asian dust can be transported over global scales [Clarke et al., 2001; Grousset et al., 2003]. Satellite images (such as from SeaWiFS and MODIS) often reveal dust plumes being transported over intercontinental distances [Husar et al., 2001; Hsu et al., 2006]. Thus Asian dust affects the regions downwind of the dust sources, such as the populated areas of China, Japan and Korea. Studies also have shown that Asian dust influences elevated sites in the Western United States [VanCuren, 2003].

Numerous model simulations of Asian dust storms have been conducted over the past two decades and several limitations have been identified based on comparisons of the existing modeling results and observations. For example, simulations with a regional scale

meteorology and dust transport model applied to Asia have indicated the difficulty in capturing the timing and magnitude of known dust events [Uno et al., 2005]. A comparison of eight dust emission/transport models over Asia showed great discrepancies among the models of the dust emission fluxes over Asian dust source regions (e.g., Taklamakan Desert and Mongolia) [Uno et al., 2006]. Uno et al. [2006] also indicated the modeling of dust transport and deposition processes between China and Japan needs to be improved and a better understanding of dust long-range transport is needed.

Our goal in this chapter is to use our best understanding of dust emission, transport, and deposition processes to simulate the downwind distributions of Asian dust using a new numerical model that combines a three-dimensional coupled climate model (CAM3) [Collins et al., 2004] and a microphysical model (CARMA2.3) [Toon et al., 1988; Jensen et al., 1994; Ackerman et al., 1995]. We test this new model primarily against data on the dust optical properties, such as aerosol optical depth (AOD), single scattering albedo (SSA), and vertical extinction, which are essential to properly simulate the aerosol impact on Earth's radiation budget and climate. Our focus here is primarily on in situ data. We plan a later comparison with satellite observations, many of which are not available for the time frame of this study.

In this chapter, we use a three-dimensional coupled climate model (CAM3) and a microphysical model (CARMA2.3) [Bardeen et al., 2008] to simulate the evolution of the mineral dust aerosols primarily during the fourth Aerosol Characterization Experiments (ACE-Asia field campaign). We run CAM3 in an offline mode in this study. Several dust transport models have been used to investigate the dust aerosols from the ACE-Asia field campaign [e.g., Chin et al., 2003, 2004; Uno et al., 2002, 2004; Carmichael et al., 2003; Gong et al., 2003; Shimizu et al., 2004]. CAM3 has previously been used to study dust transport, in the context of climate simulations using a small number of size bins [Mahowald et al., 2006]. The sectional aerosol model (CARMA2.3) allows us to define as

many particle size bins as needed. The model is driven by assimilated meteorology from the NCEP/NCAR reanalyses [Kalnay et al., 1996]; that is, the model is driven by observed wind fields to study the real-time Asian dust storm events. We validate the simulations against observations from ACE-Asia [Huebert et al., 2003].

We incorporate the Ginoux et al. [2001] dust source scheme into the coupled CAM3/CARMA2.3 model. The Ginoux et al. [2001] dust source function is one of a class of dust lifting schemes in which the dust vertical emission rate is parameterized in terms of the wind speed [Tegen and Fung, 1994; Mahowald et al., 1999; Ginoux et al., 2001]. Another type of model parameterizes the dust vertical flux in terms of friction velocity [Marticorena et al., 1997; Schulz et al., 1998; Zender et al., 2003a]. These dust emission schemes account for the dust particle size distribution and also parameterize dust emission by the saltation-sandblasting process. Saltation is the process that initiates a bouncing motion of coarse particles (the saltators) along the ground. These particles are too large to be suspended, but they eject smaller particles. The latter process is called sandblasting [Gomes et al., 1990; Shao and Raupach, 1993; Alfaro et al., 1997; Alfaro et al., 1998; Shao and Lu, 2000; Alfaro and Gomes, 2001; Grini and Zender, 2004]. We modified the Ginoux et al. [2001] dust source function by replacing the 10-m wind speed with the friction velocity, which is directly related to the surface wind stress that controls mineral dust lifting. We also account for various factors important in sandblasting, such as soil moisture.

2.2 Model Description

2.2.1 Model Configuration

We have developed a three-dimensional coupled microphysical/climate model, which combines CARMA 2.3 and CAM3. The model we are using includes mineral dust sources, as well as dust removal and transport processes. CAM3 is a three-dimensional climate model that can be driven by off-line winds to simulate particular dust storms. The dynamical model is from NCAR and it has been applied previously to study the impact of mineral aerosols on climate [Mahowald et al., 2006]. The model includes three different solutions for the dynamical equations: Eulerian spectral, semi-Lagrangian, and Finite-Volume formulations. In this study, we choose the Finite-Volume (FV) dynamical core of CAM3 for the Asian dust simulations. The FV horizontal discretization is based on the flux-form semi-Lagrangian scheme, which is a conservative dynamical scheme for tracers as described by Lin and Rood [1996].

CARMA2.3 is a bin based aerosol model. By incorporating CARMA2.3 into CAM3, we allow binned microphysics studies within the CAM3 framework. Here we configure CARMA2.3 as a column model and treat the CARMA2.3 domain with the same grid as CAM3. Once we turn on the CARMA2.3 flag, the model advances the microphysics state one time step, and the new values from the CARMA2.3 state are then stored in the CAM3 state, and so on and so forth. CARMA2.3, as a non-interactive physics package in MATCH (NCAR Model for Atmospheric Transport and Chemistry) [Rasch et al., 1997], has been used for Sahara dust simulations including the dust source, transport, deposition and optical properties [Colarco et al., 2002; Colarco et al., 2003a, b].

We have also coupled the new version of the Community Land Model 3.0 (CLM3.0) [Dickinson et al., 2006] from NCAR into our dust model. A new formulation

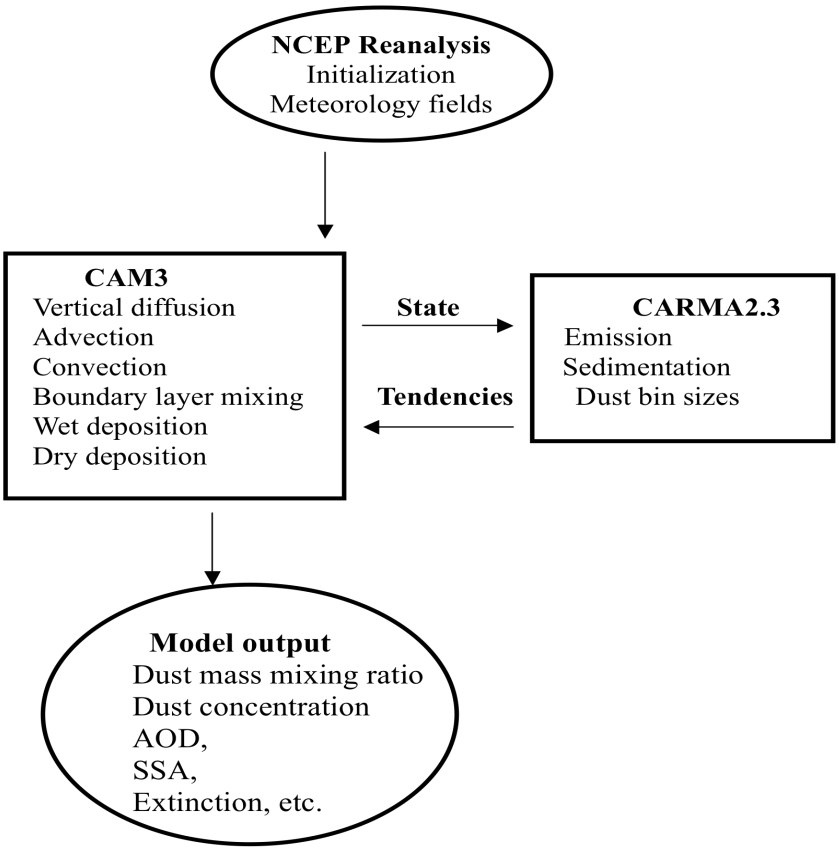

was implemented in CLM3.0 that provides for variable aerodynamic resistance with canopy density, which is related to the dry deposition velocity calculations in our dust model.

Figure 2.1 Model flow chart used in this study. We configured the coupled CAM3/CARMA2.3 model with a horizontal resolution of 2^{o} x 2.5^{o} and 28 vertical model layers. We also set eight dust size bins from 0.1 to 10 μm to parameterize the Ginoux et al. [2001] dust source function. These dust size bins are defined as advected constituents in CAM3.

Figure 2.1 shows the flow chart for the model used in this chapter. We configured the coupled CAM3/CARMA2.3 model with a horizontal resolution of 2^o x 2.5^o, and 28 hybrid vertical model layers from the surface to around 40 km. We also used eight dust size bins with central radius spanning the range from 0.1 to 10 μm to parameterize the Ginoux et al. [2001] dust source function as discussed below. The concentrations of the dust in these size bins are defined as advected constituents in CAM3. CAM3 is responsible for the vertical diffusion, advection, convection, boundary layer mixing, wet deposition and dry deposition. CARMA2.3 simulates dust emission, dust particle sedimentation and sets up the dust size bins. The model output includes the dust mass mixing ratio, which is calculated from CAM3. We added the dust concentration, dust AOD, dust SSA, and vertical extinction as output parameters for comparison with data. All these variables are computed online in the model run.

To study the dust events during the ACE-Asia period, we drive the coupled CAM3/CARMA2.3 model with data from the NCEP reanalyses. We use the prescribed (or offline) meteorological fields, rather than compute the dynamical fields from first principles. The NCEP data update every 6 hours, and then CAM3 interpolates the meteorological fields to CAM3 for each time step (every 30 minutes in this study).

2.2.2 Surface Stress and 10-m Wind in Dust Flux Expressions

Dust lifting is not physically driven by the wind at 10-m, but by the surface stress, often represented in terms of the friction wind velocity. The relationship between 10-m wind speed and friction velocity depends on (i) atmospheric stability and (ii) surface characteristics (e.g., roughness length). The motion of dust particles is initiated when the wind exceeds some threshold such that the force exerted by the wind overcomes the gravitational force and inter-particle cohesive forces on the grains [Marticorena and

Bergametti, 1995]. The parameterization of dust emission should be based on wind erosion theory and the saltation-sandblasting process. The dust source formulation should include land surface conditions (such as the surface roughness features) and atmospheric stability effects. A previous study [Liu and Westphal, 2001] compared two model simulations using friction velocity and the 10-m wind for the dust lifting. This study indicated that some dust lifting events would be missed using the 10-m wind. To further explore this issue, we parameterize the Ginoux et al. [2001] dust source scheme (see equation (1) and (2)) both using 10-m wind speed (called the 10m wind case) and friction velocity (called the ustar case) in this study.

$$F_s = C \cdot S \cdot s_s \cdot u^2(u - u_t) \quad \text{if } u > u_t \qquad (2.1)$$

$$F_s = 0 \quad \text{otherwise} \qquad (2.2)$$

where F_s is the dust flux at a particle size s, C is a dimensional factor, and which is model dependent, S is the dust source erodibility factor, s_s is a function that partitions the mass lifted into the size bins, u is the 10-m wind speed, and u_t is the threshold velocity. Note that C can be adjusted to bring the model into general agreement with data, as discussed later in this chapter. Colarco et al. [2003a] choose C by tuning the total emissions to match the expected total mass for Sahara dust. We chose a C value of 0.12 $\mu g s^2 m^{-5}$ for the case we refer to below as the friction velocity with Weibull wind distribution case (called C_{wbl}). This choice of C_{wbl} gives a total dust emission in Asia during the spring of 2001 of about 210 Tg. This mass is in the same range found by Gong et al. [2003]. The total dust emission in Asian area is 83.90 Tg in April of 2001 for friction velocity with Weibull wind distribution case. We also tuned the total dust emission of the 10m-wind case and the ustar case over Asian area to 83.90 Tg in April of 2001 (Figure 2.2) to determine C values both for the 10-m wind case (called C_{u10}) and the

ustar case (called C_{u*}). We have the following relationship for the three C values: $C_{u10} = 2.39C_{u*} = 9.59C_{wbl}$.

Our land surface model from CAM3 has spatially varying surface roughness length (Figure 2.3). Accordingly, CAM3 calculated the friction velocity based on the bulk aerodynamic algorithm [Zeng et al., 1998; Zeng and Dickinson, 1998]. Basically, this algorithm accounts for two major factors: turbulent stability functions and roughness lengths. Stability in turn depends on factors such as wind speed gradient, temperature gradient, and humidity gradient. To introduce the friction velocity we replace the 10 meter wind in the Ginoux formulation with the neutral stability formalism for the 10-m wind in terms of the friction velocity from CAM3, independent of stability that affect the 10-m wind (see equation (3) and (4) [Stull, 1988; Masson et al., 2003]).

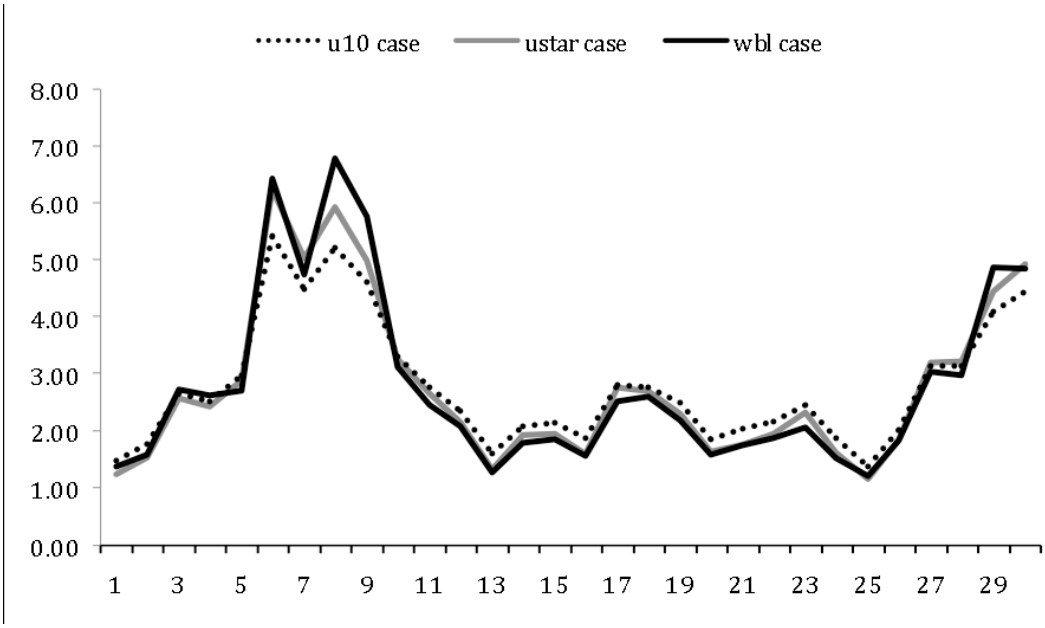

Figure 2.2 Daily accumulated total dust emission simulated by the model over the Asian area (30_N–50_N, 75_E–130_E) in April 2001. The total dust emission in the Asian area is 83.90 Tg in April 2001 for the 10-m wind case, the friction velocity case, and the friction velocity with Weibull wind distribution case, respectively.

Hence in our model a given friction velocity (for a given surface roughness) always produces the same dust lifting flux.

$$u = u_* / \sqrt{cd_n} \qquad (2.3)$$

Here cd_n is the 10-m drag coefficient under neutral condition, and we use the following assumption for cd_n:

$$cd_n = \kappa^2 / \ln^2(10/z_0) \qquad (2.4)$$

Here κ is the von Karman constant and z_0 is roughness length (Figure 2.3).

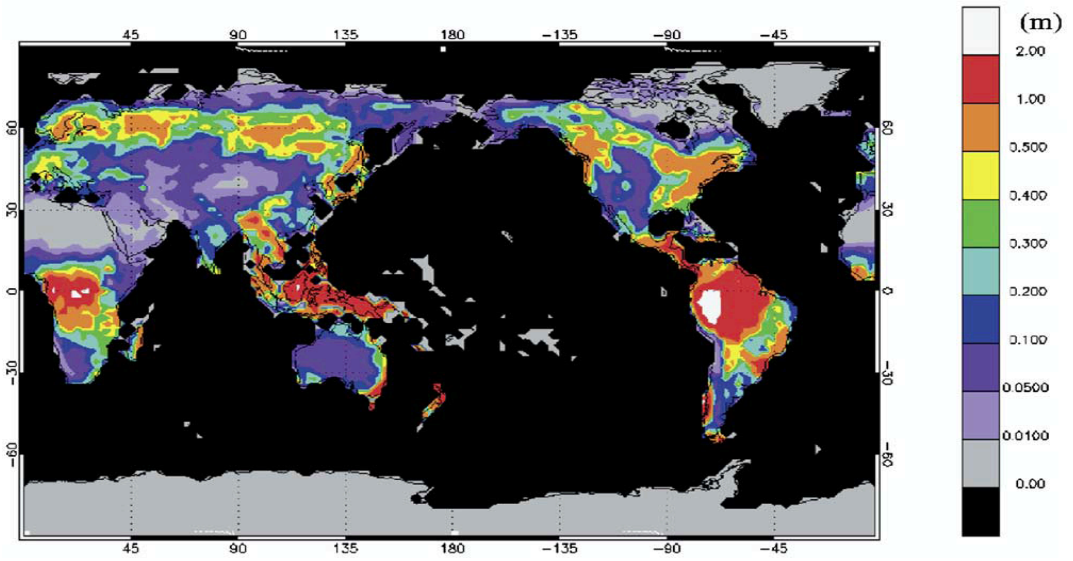

Figure 2.3 Surface roughness length calculated from the land surface model in CAM3, which is time-independent and globally distributed in the model.

To rephrase this point, our dynamical model computes a wind stress (u^* in equation (3)) that is appropriate for the stability, and roughness (z_0 in equation (4)) in each grid cell. The problem is that the Ginoux formulation uses u, not u^*, in its equations without regard to the surface properties or stability. u and u^* are not uniquely related to each other because of the dependence on stability. By replacing u

with u^* and a scaling factor that depends on z_0, given in equation (3), the fluxes are the same for the same u^* . Liu and Westphal [2001] made a similar correction: in this case they defined the wind in the Ginoux formulation as $10.5\,u^*$. We basically use the same idea, however, since our surface roughness varies with location we do not use a fixed value such as 10.5 to make the correction, but rather use a variable. The scaling factor (z_0) applied to u is unique for each grid cell since the roughness is unique for each grid cell in the model. In our formulation the flux will be the same using the surface stress or the ten-meter wind for neutral conditions. However, for other stabilities they will be different.

2.2.3 Dust Erodibility Source Factor

The dust source erodibility factor $(0 < S < 1)$ is the efficiency of the grid cell for dust lifting if the threshold wind velocity is exceeded. It is based on observations of TOMS Aerosol Index (AI). The TOMS satellite instrument is sensitive to UV-absorbing aerosols, such as mineral dust. The long-term TOMS observations show that the major dust source regions correspond to topographic depressions [Prospero at al., 2002]. The dust erodibility source factor used in this study accounts for the recently detected desertification in the Horqin Shadi desert in Inner Mongolia Province [Chin et al., 2003]. Figure 2.4(a) shows the dust source factor S on 1^o x 1^o grids from Ginoux et al. [2001]. We interpolated the dust source factor S on 1^o x 1^o grids into 2^o x 2.5^o grids (Figure 2.4(b)), which is consistent with our model resolution. We also modified the dust source function to account for the Horqin Shadi Desert (Paul Ginoux, private communication, 2007). The major dust sources have been located including the Sahara Desert in Africa, the Gobi and Taklamakan Deserts in northwestern Asia, the dried lake basin in Australia,

and the Arabian Desert. Figure 2.5 magnifies the dust source erodibility factor $(0 < S < 1)$ for Asia at a model resolution of 2° x 2.5°. The Gobi is the largest desert in Asia. The Taklamakan desert is in a large basin [Warner, 2004]. The Horqin Shadi desert is located in the eastern part of the province of Nei Mongol, China. Previous model simulations using the Georgia Tech/Goddard Global Ozone Chemistry Aerosol Radiation and Transport (GOCART) model and the meteorological forecast fields from

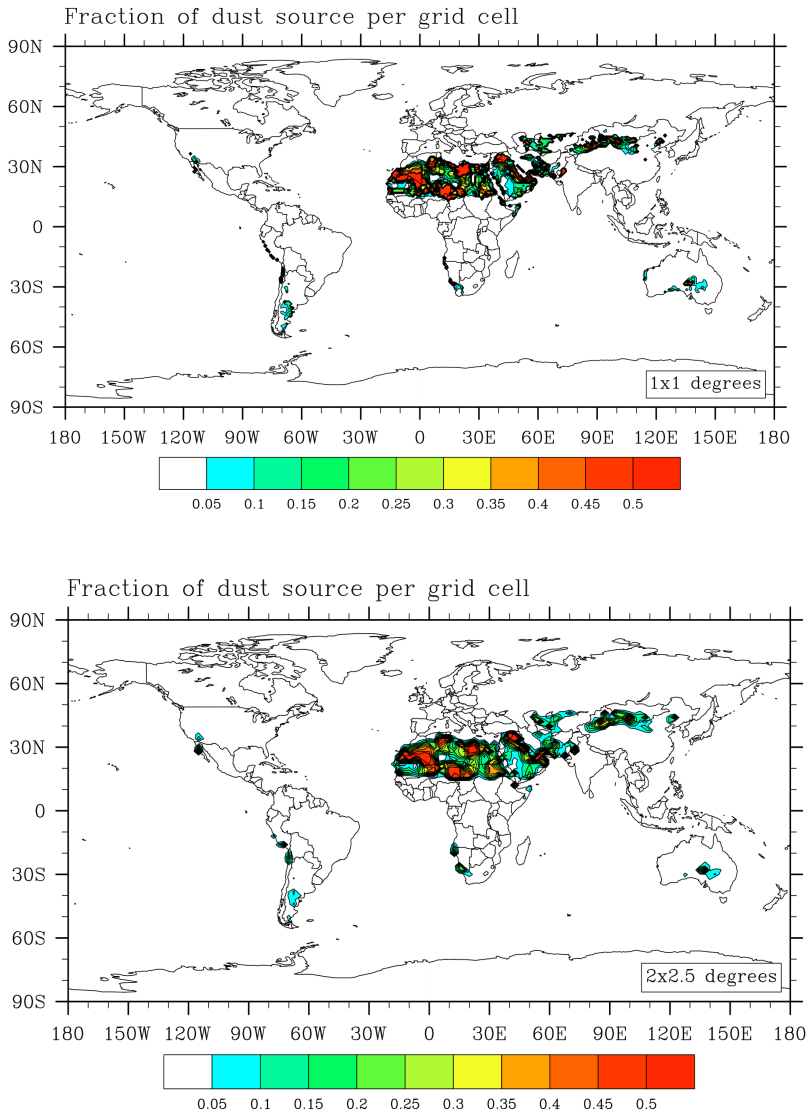

Figure 2. 4 Dust source erodibility factor (0 < S < 1) in the Ginoux et al. [2001] dust emission scheme at two model horizontal resolutions: (a) 1x1 degree and (b) 2x2.5 degrees. We use the latter case, which is consistent with our model resolution.

the Goddard Earth Observing System data Assimilation System (GEOS DAS) during ACE-Asia showed a significant difference in the total dust emission between using the Ginoux et al. [2001] dust erodibility source factor and the modified one that accounted for the desertification areas over the Inner Mongolia Province in China [Chin et al., 2003].

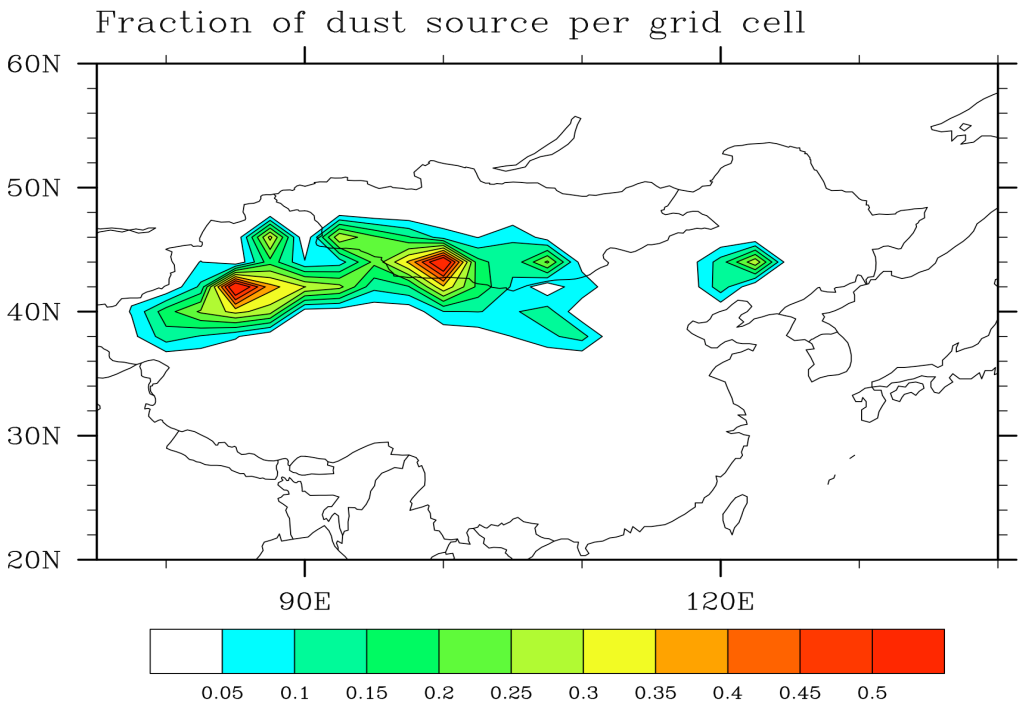

Figure 2.5 Dust source erodibility factor (0 < S < 1) in Asia for the Ginoux et al. [2001] dust emission scheme at a horizontal resolution of 2x 2.5 degrees, which is consistent with our model resolution.

2.2.4 Dust Bin Size Distribution

CARMA2.3 is a sectional or bin microphysical model, which can be run with any number of particle size bins based on our scientific questions. Small particles have small fall velocities. However, their optical properties are very sensitive to the particle size distribution. In this study, we used eight soil particle bins ranging from 0.1 to 10 μm in radius to treat long-range transport, removal process, and optical properties of mineral dust generated from Asian dust storm events. For the larger four bins (in the range 1 - 10 μm radius), we calculate the flux following Ginoux et al. [2001], where the parameter s_s in that equation is 1/4 for each bin. We treat the four smaller bins as a class and we calculate the flux following Ginoux et al. [2001] with s_s = 0.1 for this class. This mass of dust is apportioned across the four smallest bins fractionally: 0.009, 0.081, 0.234, and 0.676 in increasing bin size (the sum of those numbers is 1) [Tegen and Miller, 1998].

2.2.5 Threshold Velocity for Wind Erosion

Several previous studies have chosen the threshold wind velocity to be constant [Tegen and Fung, 1994; Tegen and Miller, 1998; Liu and Westphal, 2001]. Ginoux et al. [2001] do consider the aerosol particle size distribution and soil moisture for their threshold wind speed; however, they may have underestimated the effect of cohesive

forces on small particles since their threshold velocity increases with increasing particle size. The relationship between soil particle size lifted and the threshold wind friction speed for saltation has been measured in wind tunnels [Shao et al., 1996]. Iversen and White [1982] and Marticorena and Bergametti [1995] addressed the effect of the inter-particle cohesion forces to predict the saltation threshold friction velocity. However, they derived a parameterization for the threshold friction velocity over ideal smooth surface (no roughness or moisture effects). In this study, we use a size dependent velocity formulation based on Marticorena and Bergametti [1995], and the soil volume moisture correction from Ginoux et al. [2001] both for the 10-meter wind case and friction velocity case. The parameterization of threshold friction velocity from Marticorena and Bergametti [1995] can be used in the 10-meter wind case, which has been thoroughly discussed in Colarco et al. [2003a]. This point has also been verified by observations [Alfaro et al., 1998]. The new formulation used in this study includes the threshold velocity from Marticorena and Bergametti [1995] for each particle size bin and the surface wetness factor that is based on the volumetric soil water from the land surface model at a depth of 0.71006 cm. The threshold velocity is:

If $0.001 < w < 0.5$ then $u_t = u_{t*} \cdot (1.2 + 0.2 \cdot \log_{10} w)$ (2.5)

Otherwise $u_t = \infty$ (2.6)

Here u_{t*} is the threshold velocity of wind erosion from Marticorena and Bergametti [1995], and w is the volumetric soil moisture ($0 < w < 1$). It should be noted that we use equation (3) and (4) to replace u_{10} in Ginoux's formulation to calculate dust emission based on equation (5) and (6).

2.2.6 Weibull Wind Distribution

Another issue that is important to treat is the representation of the sub-grid scale velocity distribution. This can be treated using Weibull wind distributions (called the wbl case). From previous dust lifting studies, it has been found that applying a wind gust distribution in the dust lifting schemes causes the lifting to be changed significantly, improving agreement between simulations and data [Westphal et al., 1988; Colarco et al., 2002; Grini and Zender, 2004]. This improvement occurs because at the coarse resolutions of typical global models the "mean" wind speeds at each grid cell do not represent the lifting process well. Previous studies have also shown that the considerable differences of the wind flow in the source regions between models result in significant differences in the dust emission flux [Uno et al., 2006]. In this study, we incorporated the Weibull distribution [Gillette and Passi, 1988] for the wind gust distribution to drive the dust source functions in the Ginoux et al. [2001] dust-lifting scheme. Following Justus et al. [1978] and Grini et al. [2005], a scale factor c_{ref} (m s^{-1}) in the probability distribution for wind speeds, PDF, is defined as follows:

$$c_{ref} = U_{ref} \cdot [\Gamma(1 + 1/k_{ref})]^{-1} \qquad (2.7)$$

where

$$k_{ref} = 0.94\sqrt{U_{ref}} \qquad (2.8)$$

Where k_{ref} is the shape factor and U_{ref} is the wind speed in PDF and the subscript ref denotes quantities at a height 10-m and Γ is the gamma function. The Ginoux et al. [2001] dust source function has the form:

$$dF/dr = F_1(r) \cdot u^n \qquad (2.9)$$

Where u is the 10 meter mean wind speed, and $F(r)$ is the part which is related to the dust bin sizes. After integrating formula (9) from the threshold wind velocity u_t to infinity, we got the Weibull distribution for the dust lifting schemes as follows:

$$dF/dr = c_{ref}^{n} \cdot F(r) \cdot \Gamma[\frac{n}{k_{ref}} + 1,(\frac{u_t}{c_{ref}})^{k_{ref}}] \qquad (2.10)$$

Where n is the exponent in equation (9), and Γ is the incomplete gamma function given by

$$\Gamma(a,z) = \int_z^{\infty} t^{a-1} e^{-t} dt \qquad (2.11)$$

Combining equation (7), (8) and (10) with equation (3) and (4), we can easily calculate the dust emission when accounting for the friction velocity with Weibull wind distribution in the model.

2.2.7 Parameterization of Removal Processes

We will discuss two types of removal processes in this study: dry deposition (due to turbulent mixing and sedimentation near the surface) and wet deposition (scavenging by precipitation).

For wet deposition, we use the existing scavenging parameterization described in Barth et al [2000] and Rasch et al [2001]. CAM3 calculates the wet deposition rate for aerosols separately from the trace gases. This is because trace gases are scavenged only by the liquid hydrometeors, whereas aerosols are also scavenged by snow. For temperature below 0^{o}C, the scavenging is assumed to be all snow. CAM3 accounts for both below-cloud and in-cloud scavenging for each model layer. At temperature below -20 ^{o}C, the cloud fraction is 100% ice.

The below-cloud scavenging, which is size and composition independent, is expressed by the following relationship [Dana and Hales, 1976; Balkanski et al., 1993]:

$$L_{W\,bc} = 0.1 \cdot Pq \qquad (2.12)$$

where $L_{W,bc}$ is the mixing ratio loss rate by below-cloud scavenging, 0.1 is the collection efficiency per mm of rain, P is the precipitation flux (mm h^{-1}), and q is the tracer mass mixing ratio.

For in-cloud scavenging process (both convective and stratiform clouds), the aerosols can be removed both by rain and snow, in a manner that is size and composition independent. CAM3 assumes 30% of aerosol in a given size bin resides in cloud water, and 70% is interstitial and cannot be removed. The aerosol transferred from the cloud water to the precipitation is proportional to the fraction of cloud water that is converted to rain. Cloud water that is not converted to rain releases its aerosol at a prescribed evaporation rate. As the rain falls, the same evaporation rate is assumed both for rain and aerosol as in the in-cloud scavenging rate calculations.

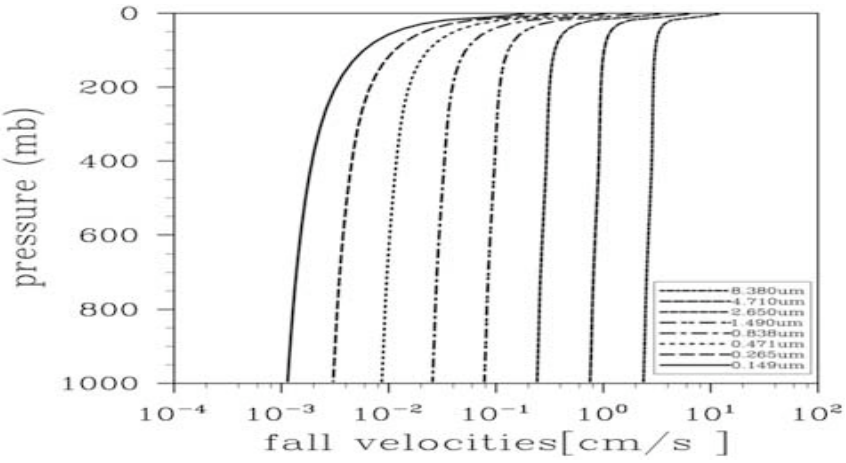

Figure 2.6 Dust fall velocities as a function of altitude for each radius bin.

For dry deposition, we modified the Ginoux et al. [2001] dry deposition scheme for mineral dust based on the dry deposition process described in Seinfeld and Pandis

[1998] and Zhang et al. [2001]. The mineral dust particles are transported downward by gravitational settling which is treated by the CARMA2.3 advection algorithms. For coarse mode particles, the sedimentation dominates the removal whereas turbulent deposition removes fine mode particles. The dry deposition velocity includes two parts: sedimentation near the surface and turbulent mix-out. For flows at low Reynold's numbers (Re < 1), CARMA2.3 calculates the sedimentation fall velocities by Stokes law

$$v_s = 2 \cdot \rho_p \cdot g \cdot r^2 \cdot C_{Cunn} / (9 \cdot \mu) \qquad (2.13)$$

where ρ_p is the density of the particle, r is radius of particle, g is the acceleration of gravity, μ is the dynamic viscosity of the air, and C_{Cunn} is the slip (Cunningham) correction factor. For flows at high Reynold's numbers (Re > 1), corrections are made following Prupacher and Klett [1997]. The particle fall velocities for each radius bin are shown in Figure 2.6. The fall or settling velocity is a function of particle size, density and air viscosity. The fall velocity in the lowest model layer is used as the sedimentation velocity near the surface for the dry deposition velocity calculations. The relatively small settling velocity in the lowest model layer is due to the relatively high air viscosity there.

The dry deposition velocities are calculated following Seinfeld & Pandis [1998] and Zhang et al. [2001]. The formulation is

$$v_d = \frac{1}{r_a + r_b + r_a r_b v_s} + v_s \qquad (2.14)$$

where r_a is the aerodynamic resistance, which is calculated in the CAM3 land surface model, r_b is the quasi-laminar resistance, which is calculated following Zhang et al. [2001], and v_s is the sedimentation velocity in the lowest model layer.

We calculate an effective dry deposition velocity following Ginoux et al. [2001], which is related to the soil moisture when the wind field is larger than the threshold wind velocity. If the soil is dry enough, the deposited dust may be re-suspended by the wind:

$$\hat{v}_d = v_d \cdot (w + (1-w)\exp[-(u_* - u_{*_t})]) \quad u_* > u_{*_t} \qquad (2.15)$$

$$\hat{v}_d = v_d \quad \text{otherwise} \qquad (2.16)$$

where w is the surface wetness. For the ustar case we have replaced u_{10m} and u_t by u_* and u_{*_t} under neutral conditions, respectively, based on the surface drag coefficient properties. From this formula, one can see that if the wind is strong enough, there will be less dust removal if the surface is dry. Whereas over a wet surface, $\hat{v}_d$ is close to v_d.

2.2.8 Modeled Optical Properties

The optical properties of the model aerosols, such as the aerosol optical depth (AOD), the single scattering albedo (SSA), and the vertical extinction are simulated in our coupled CAM3/CARMA2.3 model for mineral dust. We used the real part of dust complex refractive index as 1.55 based on Liu et al. [2002], and for the imaginary part we use AERONET data near a major dust source region as discussed further below and shown in Figure 2.7. We use Mie theory following Dave [1968] and Toon and Ackerman [1981] as well as simulated particle size distributions from the CARMA2.3 model. The equations we used for our optical properties study are:

AOD= $\tau = \iint \pi r^2 N(r,z) q_{ext} dr dz$ (2.17)

Aerosol extinction = $\int \pi r^2 N(r,z) q_{ext} dr$ (2.18)

SSA = $\omega_0 = \dfrac{\tau_{scat}}{\tau_{ext}}$ (2.19)

where r is the particle radius, $N(r,z)$ is the particle number density ($\#\ cm^{-3}\ \mu m^{-1}$), and q_{ext} and q_{scat} are the extinction efficiency and scattering efficiency, which are wavelength dependent. Although Mie theory is not strictly correct for non-spherical dust particles, the errors in optical depth are relatively small [Mishchenko et al., 1996; Dubovik et al., 2006].

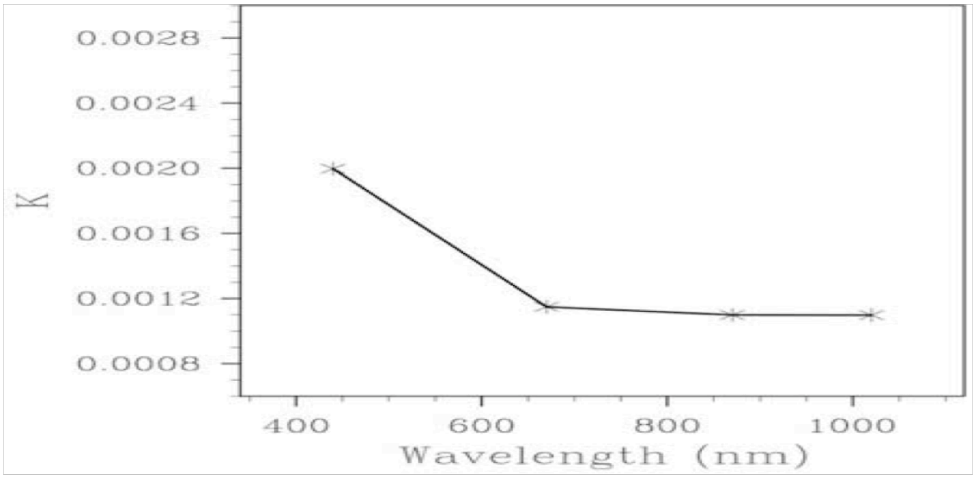

Figure 2.7 Wavelength dependence of the imaginary part (K) of the complex refractive index of mineral dust in Dunhuang, China, from the Aerosol Robotic Network (AERONET).

2.3 Aerosol Characterization Experiment (ACE)-Asia Measurements

The Aerosol Characterization Experiments (ACE) were undertaken to collect in-situ data to increase our understanding of how atmospheric aerosol particles and their radiative forcing affect the Earth's climate system. ACE-Asia was the fourth in this

series of field experiments and took place in the Asian Pacific region. ACE-Asia was conducted during the spring of 2001 along the coasts of China, Korea and Japan (Figure 2.8). Intensive observations were conducted from 31 March to 4 May 2001 over the Yellow Sea and the Sea of Japan. The ACE-Asia intensive measurements used in this study include the handheld sun photometer measurements in Zhenbeitai Tower, the AERONET measurements at Dunguang, Beijing, and the NIES lidar intensive observations (such as Beijing and Nagasaki) from March to May 2001 at all weather conditions [Huebert et al., 2003]. Because of this extensive data set, we chose to simulate dust storms during the ACE-Asia intensive field measurement period.

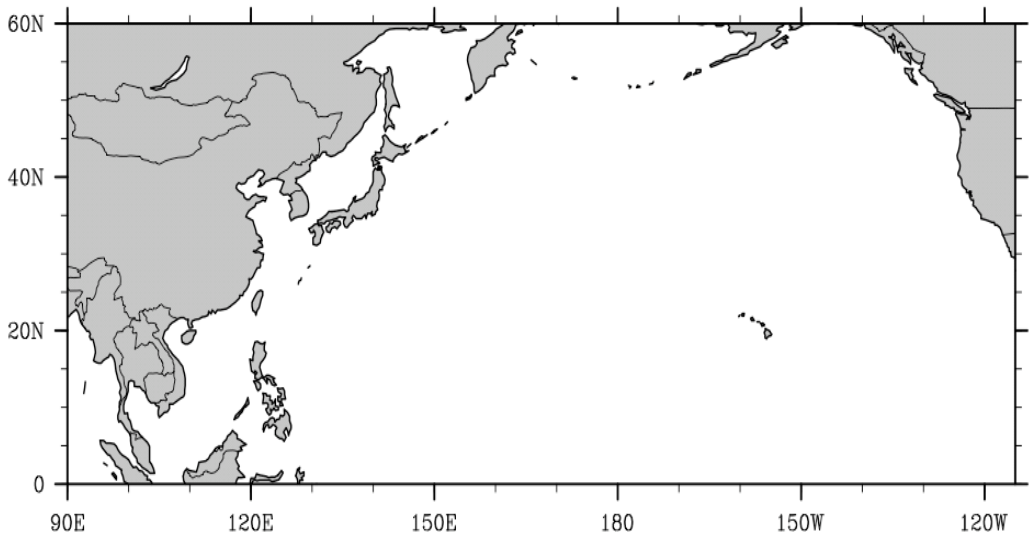

Figure 2.8 Study sites used in this chapter during the Aerosol Characterization Experiment (ACE)-Asia field campaign.

We also extended our analysis to regions downwind (such as Anmyon and Shirahama) and far downwind (such as Midway, Lanai, and Mauna Loa) of the ACE-Asia region in order to determine the spatial and temporal evolution of dust plumes transported far from the Asian dust storm sources.

2.4 Model Results

2.4.1 Dust Emission around Asian Dust Source Area

Figure 2.9 illustrates dust emission for friction velocity with Weibull wind distribution case in April 2001 used in our model. Again, after using the modified dust erodibility source factor, the dust emission has a pattern that is similar to the one from Chin et al. [2003], which accounted for the recent desertification areas in China. However, our model has larger dust emission compared to Chin et al. [2003], especially over the Taklamakan and Horqin Shadi deserts.

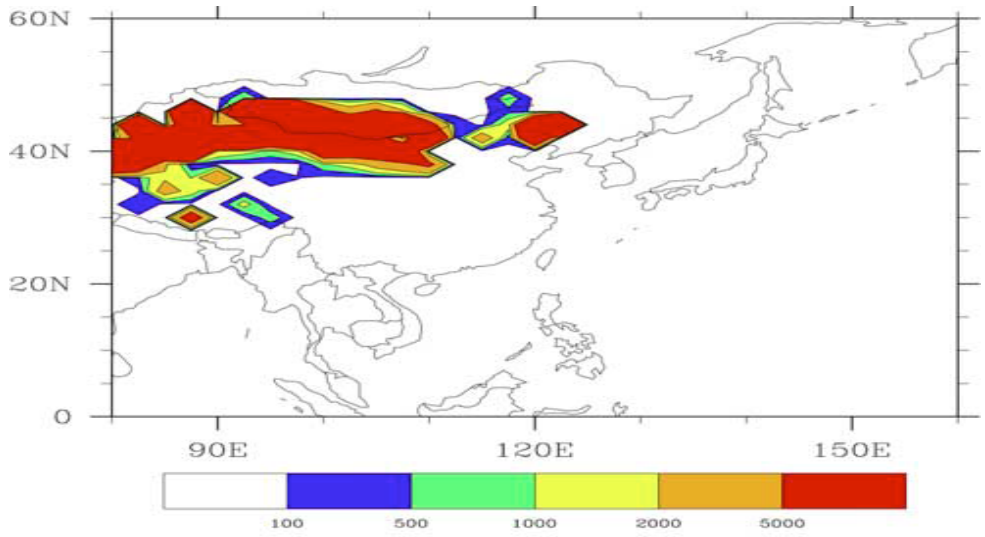

Figure 2.9 Dust emission for friction velocity with the Weibull wind distribution case in April 2001 used in our coupled CAM3/CARM2.3 model.

2.4.2 Results for the Optical Properties

The modeled aerosol optical properties, such as aerosol optical depth (AOD), single scattering albedo (SSA), and the vertical profiles are compared to measurements collected during the ACE-Asia 2001 field campaign.

Zhenbeitai Tower (38.33N, 109.7E) (Figure 2.8) is located on Mount Hongshan, which is 1100m above sea level. Major experimental campaigns were conducted in Spring 2001 and Spring 2002 at Zhenbeitai [Alfaro et al., 2003; Arimoto et al., 2004]. This site is near the city of Yulin ($38^{\circ}17'$N, $109^{\circ}43'$E) and lies in a transitional area from semi-arid to arid desert conditions. It is located in the northeastern loess plateau near the eastern margin of the Gobi Desert, a major source for mineral dust (Figure 2.5). Therefore this site can record the dust generated directly from the main Chinese dust sources, but is convenient to experimentalists since it is near the city of Yulin. During ACE-Asia Chinese scientists from the Institute of Earth Environment of the Chinese Academy of Sciences (IEECAS) measured the spectral aerosol optical depth using a 20-m tall platform on Zhenbeitai Tower. The AOD was measured several times daily in the clear-sky conditions (cloud free) with a handheld sun photometer. The sun photometer was calibrated by the Solar Light Company before the field campaign. Uncertainty in the aerosol optical depth is around 0.01 (personal communication, Michael H. Bergin, 2008).

Figure 2.10 shows the surface AOD at Zhenbeitai Tower in April 2001 compared to the model results at a wavelength of 500nm. The model result is calculated above1100m relative to sea level because the Zhenbeitai Tower is located on a mountain peak. Generally, the magnitude and pattern of model simulations agree well with the observations for the AOD with the relative average error of 0.223. The model missed a major dust event on April 15.

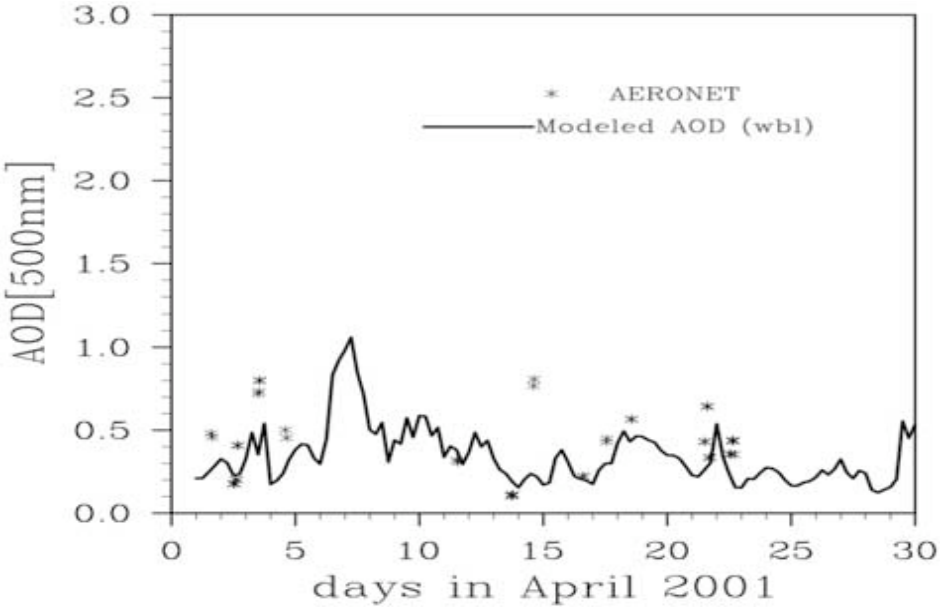

Figure 2.10 Comparison of 500-nm aerosol optical depths between model simulations of the friction velocity with the Weibull wind distribution case and ACE-Asia observations from Zhenbeitai Tower, China, during April 2001.

The ground-based AERONET is a globally deployed long-term remote sensing aerosol monitoring network established by NASA [Holben et al., 1998]. The column-integrated spectral aerosol optical depth (AOD) is measured by the sun-photometers in sixteen spectral channels (340 – 1640 nm). We choose the cloud-screened and quality-assured [Smirnov et al., 2000] AERONET AOD for our model validation. We used the coarse mode optical depth for comparison with our simulations. The total dust emission over Asian area is around 210 Tg in spring of 2001 (March to May) in our model, which is comparable to the dust emission of 250 Tg during March to May of 2001 from Gong et al. [2003]. Gong et al. [2003] applied the North Aerosol Regional Climate Model (NARCM) with 45 km resolution. AERONET sun photometer measurements also provide several aerosol inversion products, such as volume size distribution, single scattering albedo, Angstrom exponents, and complex refractive index. Although AERONET

conducts point measurements, a relatively uniform evolution of the optical depth may determine if the data are representative of the larger region in one of our model grid cells. The study sites from AERONET we used in this study are listed in Figure 2.8. Although other AERONET sites are available we used these because they form a line that is generally in the direction of transport across the Pacific based on the previous studies, which have covered the subject of the long-range transport of Asian dust particles to Midway (Betzer et al., 1988; Stith et al., 2008), central Pacific (Duce et al., 1980), Hawaii (Shaw, 1980; Clarke et al., 2001; Stith et al., 2008) and California (Husar et al., 2001; Clarke et al., 2001; Tratt et al., 2001).

Figure 2.11 illustrates the daily mean column-integrated AERONET and simulated volume size distributions at Beijing (top), on 08 April 2001 and at Midway, on 13 April 2001 during dust events. This figure clearly shows that simulated dust events have a noticeable coarse mode at 1- 8 μm radius, similar to AERONET retrievals both for Beijing and Midway. Therefore, all the comparisons related to AERONET AOD retrievals will be conducted between model and coarse mode AERONET retrievals. There are fine mode particles in the AERONET size distribution data in Figure 2.11, but such particles have not been included in our model.

Figure 2.12 compares the AERONET coarse mode AOD (black marker line) to simulated AOD for the 10-meter wind case, the friction velocity case, and the friction velocity with Weibull wind distribution case at 500nm wavelength. These results are daily means in April 2001 at six Asian dust study sites (Figure 2.8). The error bars for the six study sites are the standard deviations based on all the measurements made during a day for the coarse mode AOD of AERONET retrievals. The Mauna Loa data are limited to data taken before 10:00AM local time to reduce the contribution of sea-salt

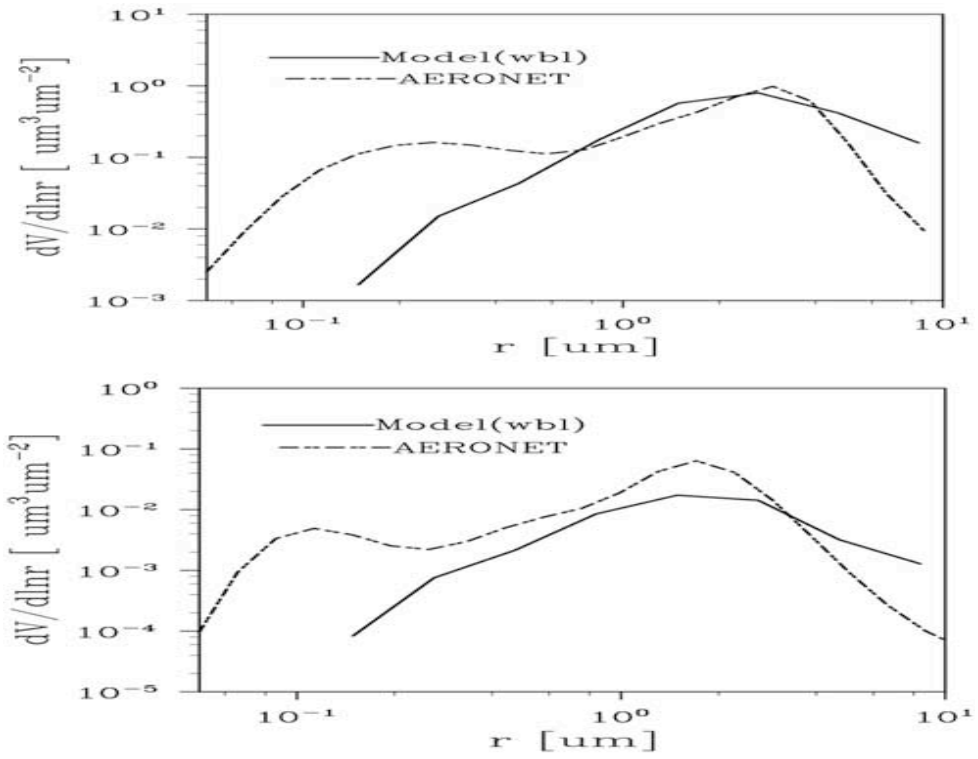

Figure 2.11 Comparison of the daily mean, column-integrated volume size distributions between model and AERONET retrievals for (top) Beijing on 8 April 2001 and (bottom) Midway on 13 April 2001.

aerosols to the coarse mode by upslope winds [Hahn et al. 1992; Bodhaine 1996]. In general, there is little difference between the AOD modeled using 10-meter winds or friction velocity winds in contrast to the conclusions of Liu and Westphal [2001]. The model did well in capturing the magnitude of the AERONET retrieved AOD at Lanai, a site far away from dust sources. The AERONET retrieved AOD is high compared to the modeled AOD in Mauna Loa even though the model results are for 4km altitude, comparable to the altitude of Mauna Loa (4170 m). Possibly the error is due to the model not including the stratospheric aerosol optical depth, which should be a relatively constant background at Mauna Loa. There may also be coarse mode particles from sea salt at Mauna Loa, which are not included in the model. At most sites, the day-to-day

variation of the modeled AOD suggested that the meteorology fields, or variation in dust sources, are significant sources of variability in the model.

Generally, the model captured most dust storms that occurred during April 2001 over the Beijing area: April 04, April 07-08 (the severe one), April 18, and April 28. The model for all three dust lifting cases misplaced the peak of the dust storm that occurred on April 8-10, 2001 for Beijing. As shown in Figure 2.13, dust was in the Beijing region on April 10. Apparently, the simulated dust did not follow the observed trajectories exactly. It should be noted that the GOCART model [Chin et al., 2004] missed the same dust event on April 10, 2001. The magnitude and pattern of AOD from our model are similar to Chin et al. [2004] at Beijing, in April 2001. Chin et al. [2004] and our model both overestimated the AOD at Shirahama between April 15 to 20, which should have relatively smaller AOD for dust aerosols than April 10 as indicated in the coarse mode AERONET retrievals in Figure 2.12.

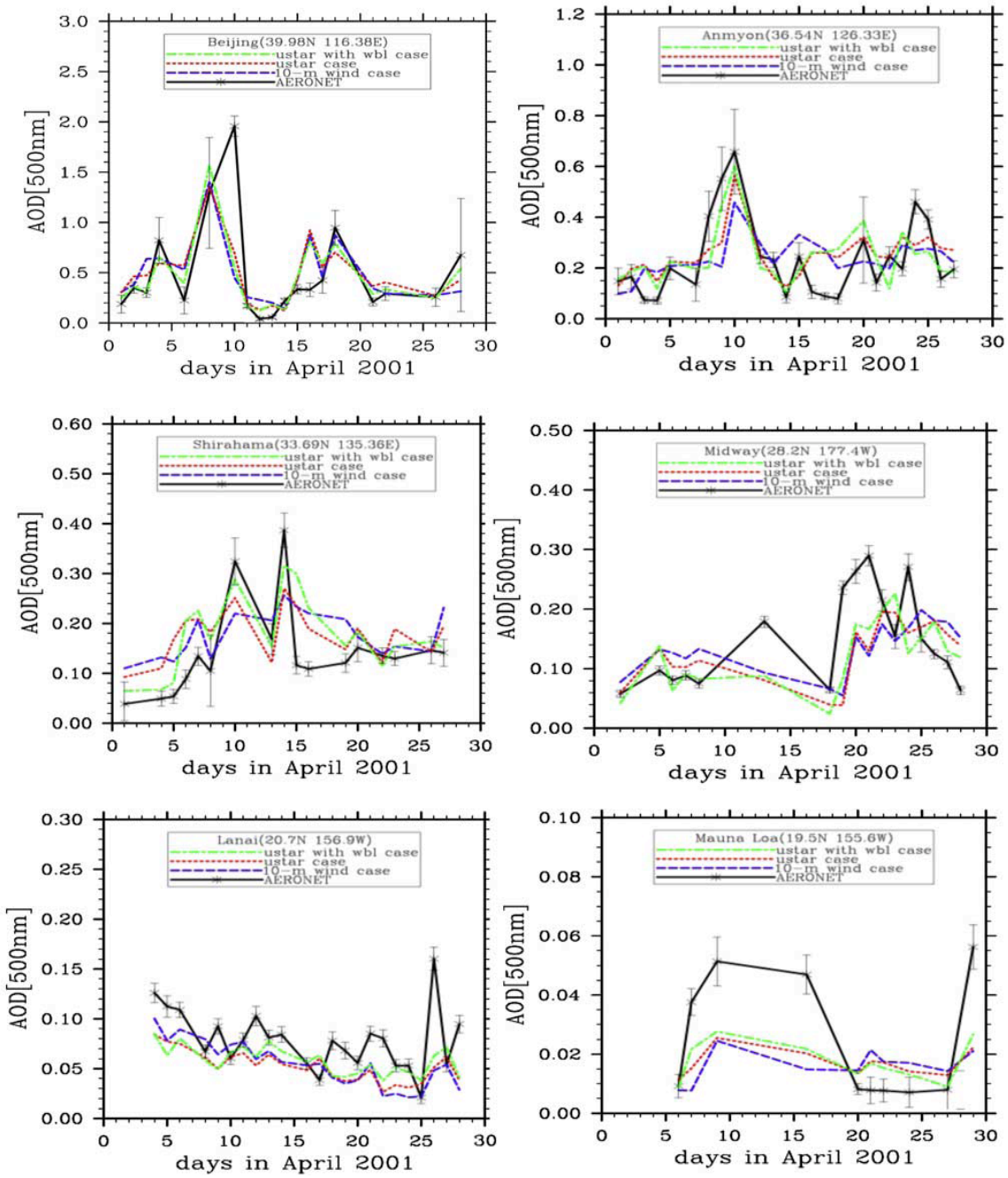

.

Figure 2.12 Comparison of predicted daily mean dust aerosol optical depth (AOD) from the 10-m wind case, friction velocity case, and friction velocity with Weibull correction to AERONET coarse mode data for six different study sites in April 2001.

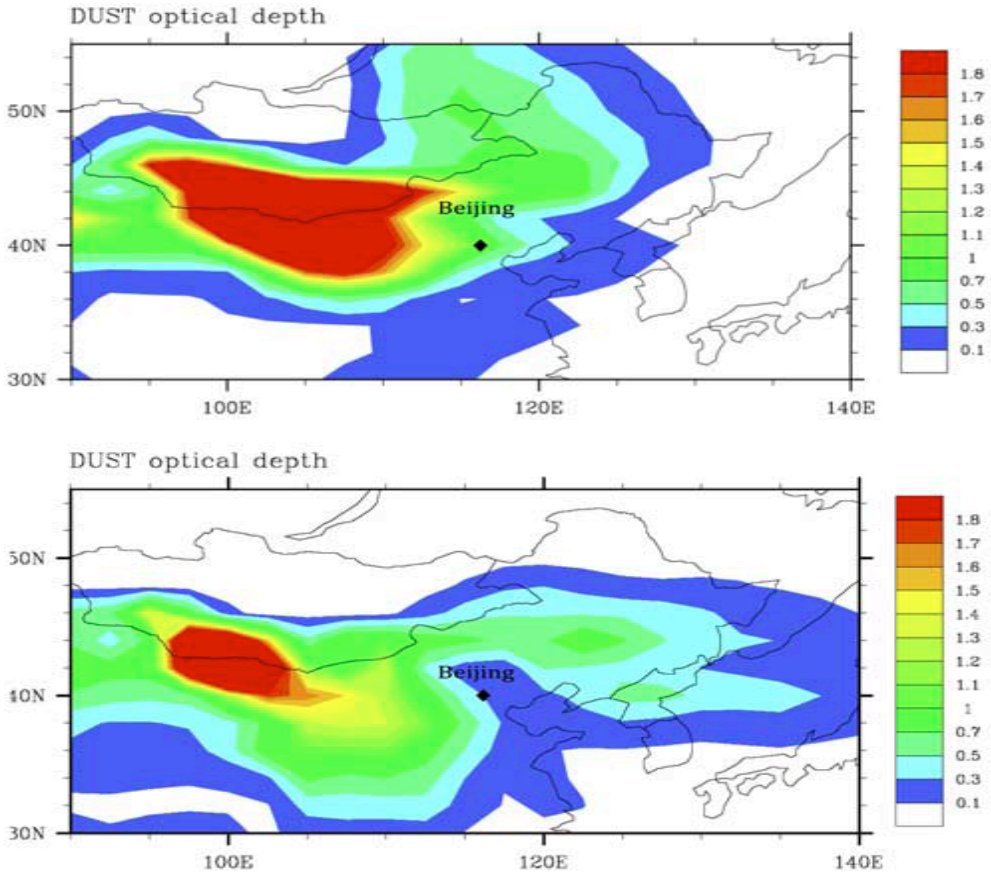

Figure 2.13 Dust aerosol optical depths over the Beijing area (39.98_N, 116.36_E) and its upwind regions (40_N,115_E) for (top) 7 April 2001 and (bottom) 10 April 2001.

Figure 2.14 present the scatter plots of daily mean AOD at 500nm between the model for the 10-meter wind case (top), the friction velocity case (middle), and the friction velocity with Weibull wind distribution case (bottom) and AERONET coarse mode retrievals at six study sites (Figure 2.12) for April 2001. The dashed lines represent the one-to-one line, 2 times of one-to-one line, and half time of one-to-one line, respectively. The solid black line represents the line of best fit through all points. The three equations of the lines of best fit are y=0.690x + 0.087 (u10 case), y=0.721x+0.082 (ustar case), and y = 0.752x + 0.065 (wbl case), respectively. The correlation coefficients for the three

cases (R_{u10}=0.712, R_{u^*}=0.755, and R_{wbl}=0.790) are reported in Figure 2.14. We find that the modeled AOD for the three cases reproduced most of the data within a factor of 2 of the AERONET retrievals and lies close to the one-to-one line.

We assume the real part of the complex refractive index is independent of wavelength (1.55) based on the AERONET retrievals [Dubovik et al., 2000]. We use data on the imaginary part of the refractive index from AERONET site measurements near the dust source regions that are dominated by relative pure mineral dust particles compared to the downwind regions, where other pollutants are involved, such as nitrate, sulfate, and black carbon. Figure 2.7 shows the wavelength dependence of the imaginary part (K) of the complex refractive index of mineral dust for Dunhuang, China, on April 7, 2001 from AERONET retrievals. Dunhuang, China is located in Gobi desert, one of the major dust source regions in Asia. K decreases with the increasing wavelength (440nm, 670nm, 870nm and 1020nm), which means the dust particles absorb more light in the short-wavelength range and scatter more light in the long-wavelength range. This behavior is consistent with a red colored dust [Sokolik and Toon, 1999].

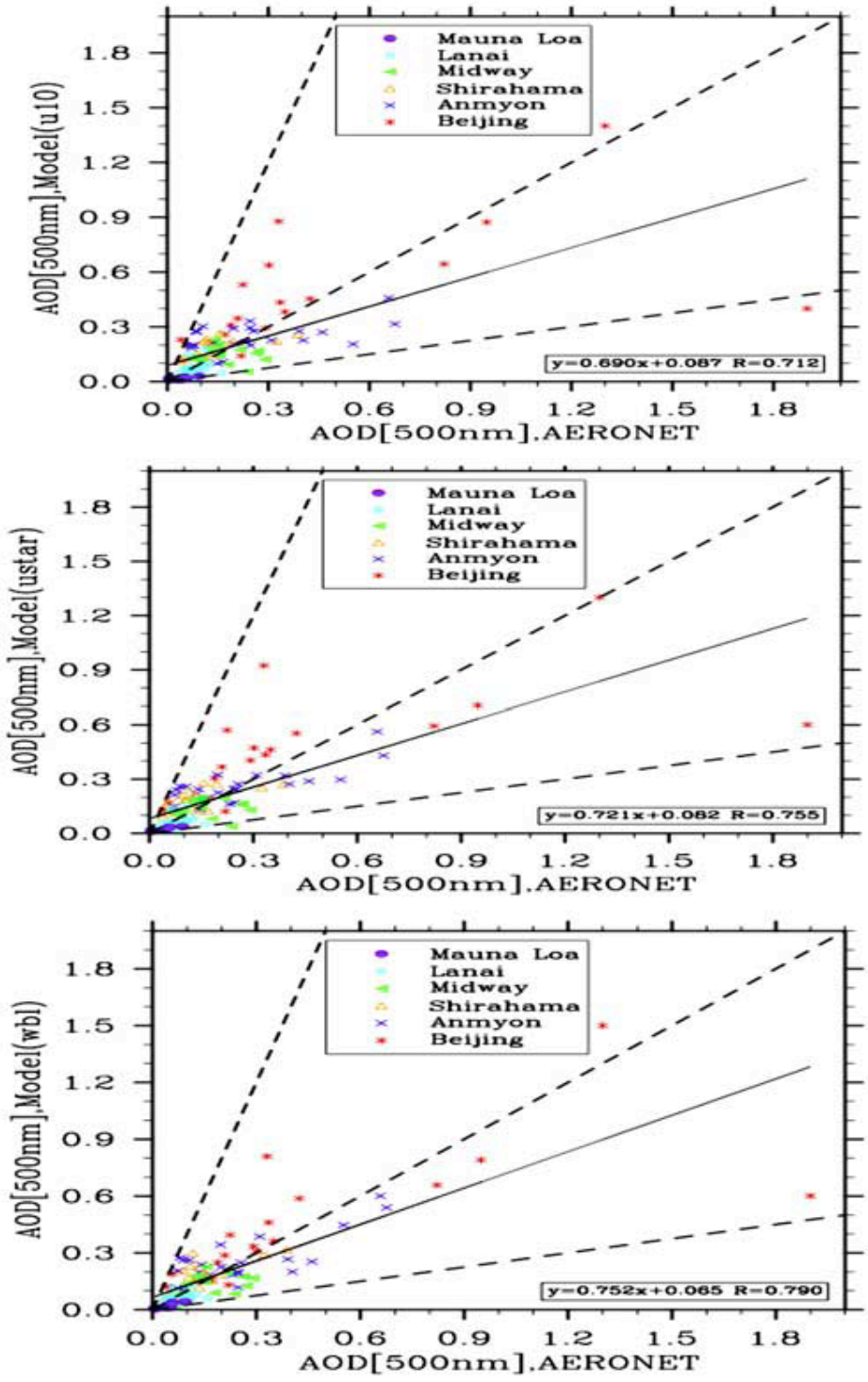

Figure 2.14 Scatterplots of daily mean AOD from model simulations of (top) u10 case, (middle) ustar case, and (bottom) wbl case versus AERONET coarse mode retrievals at six study sites (Figure 12) in April 2001.

Figure 2.15 presents the wavelength dependence of the SSA compared to AERONET retrievals over Dunhuang, China on 7 April 2001. The marked line is the SSA from AERONET retrievals, and the dash line is modeled SSA. The SSA increases with increased wavelength in both the model and observations. The model is within the error bars of the AERONET data. Of course, the AERONET data from this site was used to obtain the refractive index. Nevertheless SSA and its wavelength dependence vary with particle size, so this comparison is not circular. The single scattering albedo of dust may have regional variations. The averaged SSA value from AERONET retrievals and model simulation is 0.947and 0.920 at 0.55 μm (obtained by interpolation), respectively, in this study in Dunhuang area, whereas it is around 0.90 ± 0.06 at 0.532 μm in South Asia [Müller et al, 2003] and less than 0.90 at 0.55 μm in the Sahara Desert [Takemura et al., 2002]. The dust transported from East Asia to the Pacific may not absorb as much light as the dark aerosol from South Asia or from the Sahara Desert [Sokolik and Toon, 1999]. The SSA varies by less than 0.02 as the particles cross the Pacific in the model.

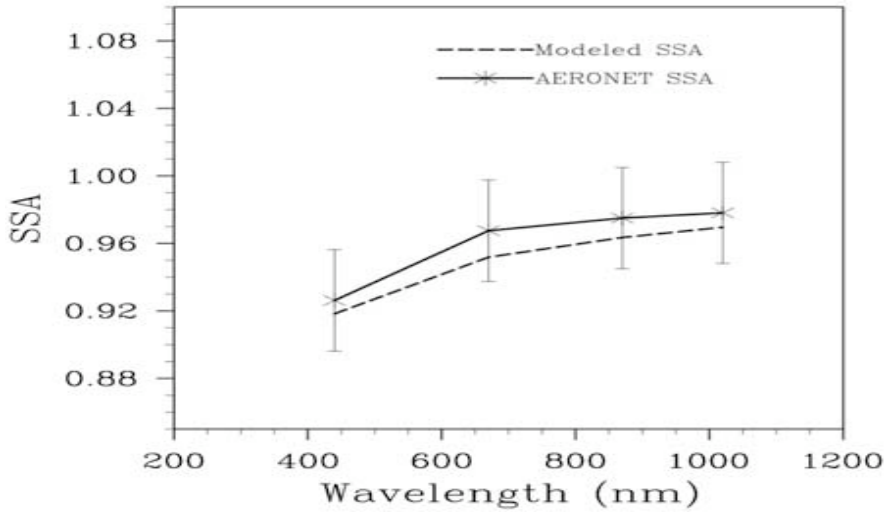

Figure 2.15 Wavelength dependence of single-scattering albedo (SSA) compared to AERONET retrievals over Dunhuang, China, on 7 April 2001.

Lidar measurements of Asian dust have been conducted for more than 20 years. The lidar observations are commonly used to indicate the vertical distributions of aerosol layers [Iwasaka et al., 1988]. During the ACE-Asia field campaign, polarization lidars (non-spherical aerosol can be identified by the depolarization ratio of backscattering signal) from the National Institute for Environmental Studies (NIES), Japan were operated in China and Japan from March to May 2001. NIES-Lidar with a compact back-scattering system began continuous observation in the atmosphere in 1996. Polarization measurement capability was added in 1999. Vertical profiles of backscattering intensity and depolarization ratio were recorded every 15 min at the observation wavelength of 532 nm. The different backscattering coefficients of dust and spherical aerosols (such as sulfates) were estimated from the depolarization ratio with the assumption that both kinds of aerosols were externally mixed [Shimizu et al., 2004].

Our point in comparing our model with lidar data is to determine if dust is present when it should be, and whether it is at the correct altitudes. We cannot compare with the magnitude of the backscatter because the particles are not spheres, and so there is a large unknown correction to the calculated backscatter cross section for particle shape that would be needed. Figure 2.16 illustrates the measured NIES-lidar backscattering coefficients contributed by dust particles (top) [Shimizu et al., 2004] and the total dust mass concentration ($\mu g / m^3$) calculated by our dust model for the friction velocity with Weibull wind distribution case over the Beijing area (39.98N, 116.38E) (middle) and upwind of Beijing region (40N, 115E) (bottom) for April 2001. Generally, the model reproduced almost all the dust events in April 2001 (middle of Figure 2.16), such as the dust storms that occurred on April 2, April 4, April 7-8 (the severe one), April 18, and April 28. However, the model missed the dust storm that occurred on April 10 as we mentioned before (Figure 2.12 and Figure 2.13). From Figure 2.16 (bottom), we find a

large dust mass density on April 10, 2001 upwind of the Beijing area (40N, 115E). However, this dust storm went to the south of Beijing in the model. The model also missed the low level dust storms that occurred on April 20-24, which went to the north of Beijing (Figure 2.17).

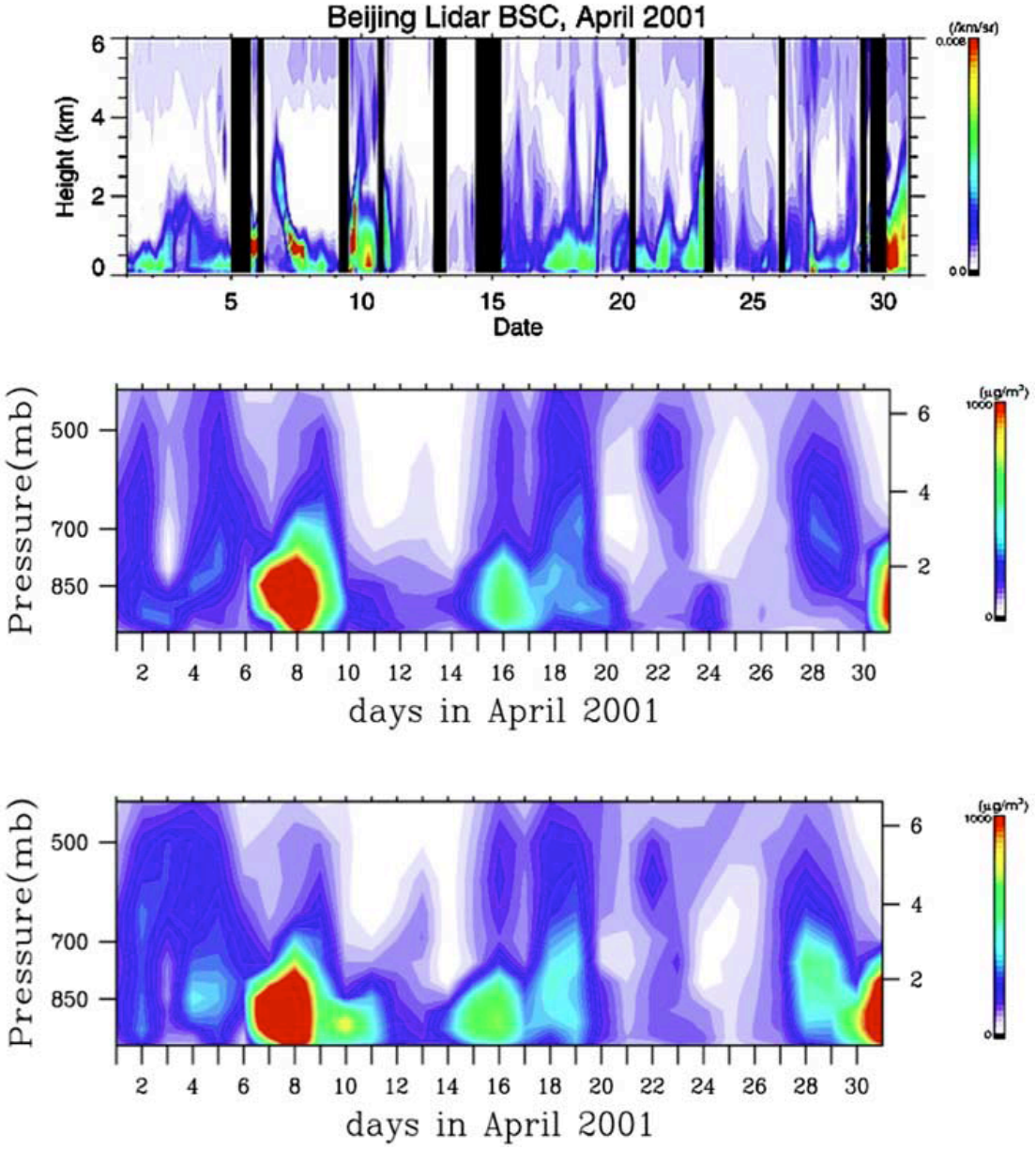

Figure 2.16 Comparison of derived backscattering coefficients of (top) derived lidar backscattering contributed by dust particles [Shimizu et al., 2004] to (middle) the total dust mass density calculated by our dust model over Beijing (39.98_N, 116.36_E) and (bottom) upwind of Beijing (40_E, 115_E) for April 2001.

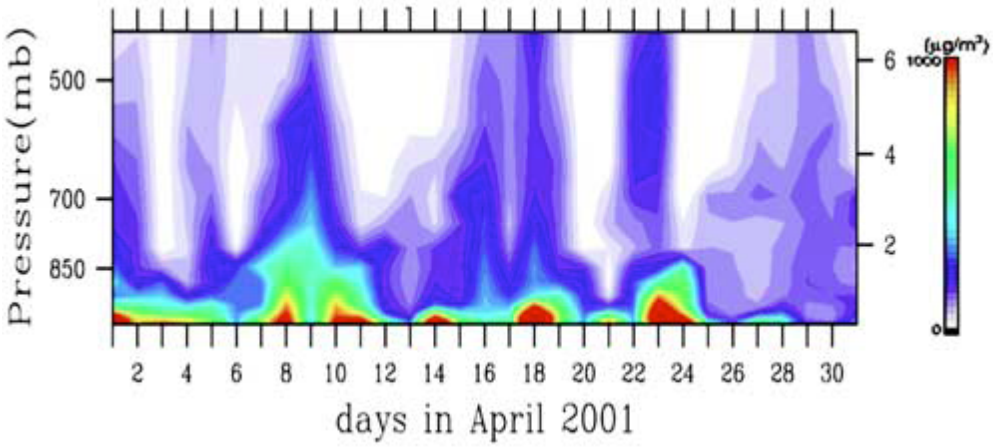

Figure 2.17 Total dust mass density calculated by our dust model north of Beijing (42_N, 120_E).

Figure 2.18 shows the measured lidar backscattering coefficients contributed by dust particles (top) [Shimizu et al., 2004] and the total dust mass concentration ($\mu g/m^3$) calculated our dust model (bottom) over the Nagasaki area of Japan (33.69N, 130.28E) for April 2001. Generally, our model well reproduced the vertical distribution of dust on 12,13, and 14 April of 2001, observed by lidar. The model also correctly simulated the dust in the free troposphere on 2, 23, 26 and 27 April of 2001, which was missed by CFORS in Shimizu et al [2004]. However, our model missed the dust event on April 20 due to incorrect model winds causing the dust to go south of Nagasaki in the model. Also, the model did not predict the dust events on 26 and 27 of April near the surface because wet deposition washed out the low level dust on the 26 of April (Figure 2.19). From Figure 2.19, we can see the wet deposition flux near the surface (below 1 km) at Beijing on April 26, 2001 has a relatively large value (up to $5.0x10^{-9} kg\ m^{-2}\ s^{-1}$), which indicates that further work is needed on the removal processes between dust source and downwind regions such as Nagasaki.

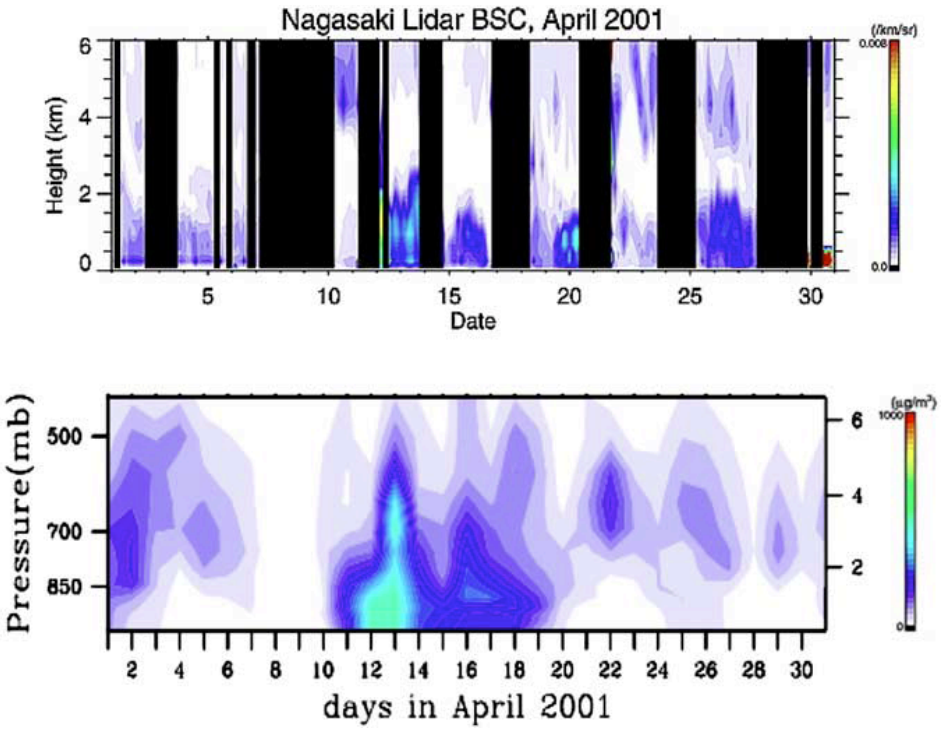

Figure 2.18 Comparison of (top) derived backscattering coefficients of lidar contributed by dust particles [Shimizu et al., 2004] to (middle) the total dust mass density calculated by the Chemical Weather Forecasting System [Shimizu et al., 2004] and (bottom) our dust model over Nagasaki (33.69_N,130.28_E) for 2001.

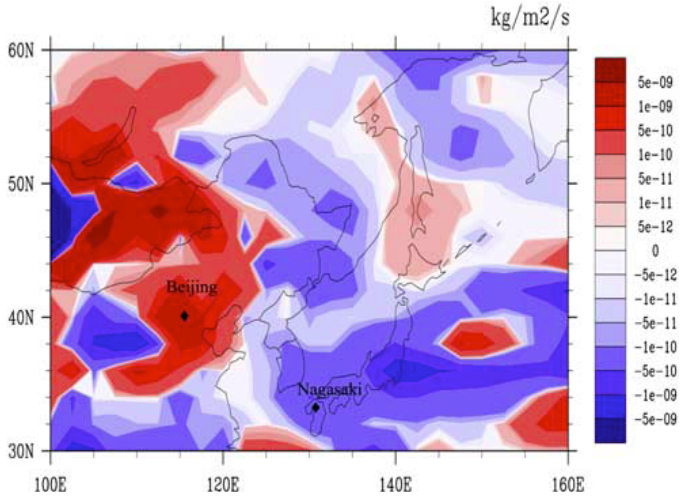

Figure 2. 19 Wet deposition flux on 26 April 2001. The negative washout rates mean that evaporation as a source of particles exceeds deposition as a sink of particles in wet deposition.

2.5 Discussions and Summary

In this chapter, we developed a three-dimensional coupled microphysical/climate model based on the NCAR CAM3 and CARMA2.3 models. Our goal was to test the model's ability to reproduce the optical properties of dust from Asia, as it is transported across the Pacific Basin. The model simulations were conducted during the time frame of the ACE-Asia field experiment since considerable data are available for that time. Our dust source function follows Ginoux et al. [2001]. We modified the source function by using the friction velocity instead of the 10-meter wind based on the wind erosion theory. The new threshold friction velocity formulation included both the inter-particle cohesion forces and the surface wetness factor based on the volumetric soil water for each particle size bin, which is important to the threshold wind speed of dust particles.

The Weibull wind distribution was implemented in the model, using an incomplete gamma function, to treat the sub-grid scale velocity distribution since at the coarse resolutions of typical global models the "mean" wind speeds at each grid cell do not represent the lifting process well. The timing and magnitude of most dust events have been captured when a Weibull wind distribution, surface stress or 10 m wind is used in the model. We tuned the dust lifting to reproduce the total dust emission around 210 Tg in spring of 2001 (March to May). Our conclusions differ from Liu and Westphal [2001] who found the 10 m winds did not capture all of the dust events in their study. Despite not finding this sensitivity in our work we believe it is important to include all of the physics related to the surface wind stress, and wind gusts since the physics may be important in cases other than the ones we examined.

The modeled AOT is well correlated with the AERONET retrievals ($R = 0.844$) in the six study sites, and the results are not greatly biased relative to the observations since the slope of their relationship is close to 1. The modeled single scattering albedo is

within the error bars of AERONET retrievals near the dust sources. SSA increased with increasing wavelength in both the model and observations. Comparing the modeled SSA over the Asian dust source region (Dunhuang) to studies elsewhere, we find that the observed single scattering albedo of dust has geographic variations that exceed those predicted by the model. This larger variation could be caused by different dust compositions and/or background pollution not included in our model.

The vertical profiles of dust are comparable to the ACE-Asia 2001 NIES-lidar observations in Beijing and Nagasaki. Generally, the model produced almost all the dust events in April 2001, such as the dust storms that occurred on April 2, April 4, April 7-8 (the severe one), April 18, and April 28 in Beijing, and the dust events near the surface on April 12,13, and 14 and the dust in the free troposphere on 2, 23, 26 and 27 April of 2001. However, the model did not predict the dust events near the surface on the 26 and 27 of April at Nagasaki because wet deposition washed out the shallow level dust on 26 of April, which indicates that further work is needed on the model wet deposition process between dust source and downwind regions, such as Nagasaki, Japan.

We have shown here that the model results are consistent with data taken during ACE-Asia. There is also a wealth of satellite data with which the model can be compared. The Cloud Aerosol Lidar and Infrared Pathfinder Satellite Observations (CALIPSO) satellite lidar retrievals will provide new insight into the broad scale dust vertical distribution. However CALIPSO was not operating during the time frame of ACE-Asia. Hence, we will present a comparison of model simulations with satellite data in chapter 3 using a different simulation time frame.

Chapter 3

Saharan and Asian Dust: Similarities and Differences determined by CALIPSO, AERONET, and a Coupled Climate-Aerosol Microphysical Model

3.1 Introduction

This work has been published as Su and Toon (2011). Airborne mineral dust is one of the major components of atmospheric aerosols. Dust plays an important role in the atmospheric global circulation (Dunion and Velden, 2004; Wu, 2007), air pollution (Prospero, 1999; VanCuren, 2003), biogeochemical processes (Duce et al., 1991; Martin et al., 1994; Shinn et al., 2000), radiative budget (Sokolik and Toon, 1996; Kaufman et al., 2001), and human health (IPCC, 2007). Dust varies over short time scales and geologic time (Rea et al., 1985).

The Saharan desert is the largest and most continuous dust source in the world. Saharan dust can be transported across the tropical North Atlantic and into the Caribbean region as well as into Europe (Prospero and Carlson, 1972; Prospero, 1996; Colarco et al., 2002; Colarco et al., 2003a,b; Toon, 2003; Liu et al., 2008; Generoso et al., 2008). Especially in summer large amounts of Saharan dust are transported across the Atlantic Ocean, which is dominated by the Azores High, and arrive in the Caribbean Sea (Doherty et al., 2008).

The Taklimakan and Gobi deserts are the major dust sources in Asia (Uno et al., 2005). Asian dust can be transported over the North Pacific Ocean and reach Midway and North America (Duce et al., 1980; Shaw, 1980; Betzer et al., 1988; Clarke et al., 2001; Husar et al., 2001; Tratt et al., 2001; Huang et al., 2008; Eguchi et al., 2009; Su

and Toon, 2009). Asian dust also can be transported over global scales (Clarke et al., 2001; Grousset et al., 2003; Uno et al., 2009).

In this chapter, we refer to all of the major dust lifting regions in Africa and Asia as Saharan or Asian deserts. These dust lifting regions for Asia can be seen from the dust flux maps given in Su and Toon (2009).

Recently, special attention has been paid to Saharan dust in field campaigns such as the Puerto Rico Dust Experiment (PRIDE) (Reid et al., 2002; Reid et al., 2003b; Maring et al., 2003; Colarco et al., 2003a,b), the Dust And Biomass EXperiment (DABEX) (Osborne et al., 2008), the SAharan Mineral dUst experiMent (SAMUM) (Heintzenberg, 2008; Knippertz et al., 2008; Muller et al., 2008), the African Monsoon Multidisciplinary Analysis (AMMA) (Rajot et al., 2008; Heese and Wiegner, 2008; Haywood et al., 2008), and the GERB Intercomparison of Longwave and Shortwave radiation (GERBILS) (Haywood et al., 2005; Marsham et al., 2008). Saharan dust has been studied through model simulations (Marticorena et al., 1997; Colarco et al., 2002; Colarco et al., 2003a,b; Maring et al., 2003; Liu et al., 2008; Generoso et al., 2008), and satellite retrievals (Liu D. et al., 2008; Liu Z. et al., 2008b; Generoso et al., 2008; Cuesta et al., 2009).

Several field campaigns have been also conducted regarding Asian dust aerosols including the Aerosol Characterization Experiments (ACE-Asia) (Huebert et al., 2003; Seinfeld et al., 2004), the Indian Ocean Experiment (INDOEX) (Ramanathan et al., 2001, Rasch et al., 2001]), the TRAnsport and Chemical Evolution over the Pacific experiment (TRACE-P) (Carmichael et al., 2003; Jacob et al., 2003), the Intercontinental Chemical Transport Experiment Phase B (INTEX-B) (Arellano et al., 2007; McKendry et al., 2008), and the PACific Dust EXperiment (PACDEX) (Stith et al., 2008). Asian dust also has been investigated through model simulations (Tegen and Fung, 1994; Schulz et al., 1998; Mahowald et al., 1999, 2006; Ginoux et al., 2001; Uno et al., 2002, 2004,

2008, 2009; Carmichael et al., 2003; Chin et al., 2003, 2004; Gong et al., 2003; Zender et al., 2003a; Shimizu et al., 2004; Shao and Dong, 2006; Huang et al., 2009; Su and Toon, 2009), and satellite retrievals (Huang et al., 2007; Huang et al., 2008; Liu et al., 2008; Uno et al., 2008).

Most studies have focused on either Saharan dust or Asian dust. Here we investigate the differences and similarities in dust lifting, dust removal processes, seasonal variations, transport mechanisms, and physical properties between Saharan dust and Asian dust using satellite data such as CALIPSO, ground-based data such as AERONET, and numerical models.

Numerous satellite observations have been made of Saharan and Asian dust. Here we focus on data from the Cloud-Aerosol Lidar and Infrared Pathfinder Satellite Observation (CALIPSO). CALIPSO was launched in April 2006 (Liu et al., 2006; Winker et al., 2007). The Cloud –Aerosol Lidar with Orthogonal Polarization (CALIOP), on CALIPSO, is a two-wavelength (532 and 1064 nm), polarization-sensitive (at 532 nm) instrument. CALIOP provides substantial and unique information on vertical and geographical distributions of clouds and aerosols. CALIOP conducts nearly continuous observations of height-resolved attenuated backscatter over the globe (Sassen 2000; Winker et al., 2003; Winker et al., 2010).

The Aerosol Robotic NETwork (AERONET) is a globally distributed remote sensing aerosol-monitoring network of ground-based sun photometers that measure sun and sky radiances in 16 spectral channels (340-1640 nm) (Holben et al., 1998). AERONET provides observations of aerosol optical depth (AOD), inversion products such as size distribution and single scattering albedo, and precipitable water. We use the cloud-screened and quality-assured AERONET Level 2.0 data in this chapter (Smirnov et al., 2000).

Numerical modeling of dust aerosols is essential for climate studies, and to better understand the behavior of the dust aerosols in the atmosphere. We use a coupled three-dimensional climate-microphysical sectional model, which is capable of simulating the mineral dust aerosols (Su and Toon, 2009) to explore the differences between atmospheric dust from the Saharan deserts and from the Asian deserts.

The various observations and models have led to a number of questions about Asian and African dust. It is clear from satellite observations that the dust optical depth is generally larger over the Atlantic, than over the Pacific. Is this difference due to more dust being lifted over Africa, to more dust being removed over the Pacific, to seasonality in dust lifting, or to other factors? Is the size distribution of dust downwind of African or Asian dust sources different, or the same so that it can be modeled using the same dust source functions? Are the dust optical properties different between Asian and African dust, and if so are the differences related to dust composition, or to particle size? Do the same mechanisms control dust transport in the two regions of the world? For instance, Saharan dust is observed to descend when crossing the Atlantic. Is this descent due to sedimentation, so Asian dust should also descend, or to air motions which may differ? Does the different meteorology of Africa and Asia lead to differences in the vertical distribution of the two types of dust? We seek to answer these questions here.

3.2 Model Description

The three-dimensional coupled climate-aerosol microphysical model based on the NCAR Community Atmosphere Model (CAM3) (Collins et al., 2004) and the University of Colorado/NASA Community Aerosol and Radiation Model for Atmospheres (CARMA2.3) (Toon et al., 1988; Jensen et al., 1994; Ackerman et al., 1995) is a new numerical model that has been described in detail by Su and Toon (2009). The coupled

model we are using for the Saharan and Asian dust simulations includes a three-dimensional climate model (CAM3) and an aerosol microphysical sectional model (CARMA2.3). CAM3 is driven by off-line meteorological fields from NCAR and the National Center for Environmental Prediction (NCEP) reanalysis package (Kistler et al., 2001). We treat CARMA2.3 as a bin-resolved column aerosol-microphysical sectional model that has the same domain as CAM3. We also choose the finite-volume (FV) dynamical core for the dynamical equations of CAM3 to conserve the mass for tracers as discussed by Lin and Rood (1996). The coupled CAM3/CARMA2.3 model includes dust sources, transport, removal processes, and optical properties of dust aerosols (Su and Toon, 2009).

We configured the coupled CAM3/CARMA2.3 model with a horizontal resolution of 2^{o} x 2.5^{o} degrees, and 28 hybrid vertical model layers from the surface to about 40 km. We used 16 dust size bins with central radius covering the range from 0.1 to 10 μm to parameterize the modified Ginoux et al. (2001) dust source function as discussed in Su and Toon (2009). Briefly, the dust lifting is physically driven by the surface stress based on the saltation-sandblasting process (Gomes et al., 1990; Shao and Raupach, 1993; Shao and Lu, 2000; Su and Toon, 2009). We use the friction wind velocity in the dust source function based on the atmospheric stability and land surface conditions (e.g. surface roughness length). We also account for the recently detected desertification in Inner Mongolia in the dust erodibility source factor (Chin et al., 2003; Chin et al., 2004; P. Ginoux, personal communication, 2007; Su and Toon, 2009). The Weibull wind distribution that represents the subgrid-scale velocity distribution has been implemented in the dust-lifting scheme to better represent the dust lifting process by subgrid scale winds that are not represented well due to the coarse resolution of global models (Gillette and Passi, 1988; Su and Toon, 2009).

We use the same parameterization of removal processes (wet deposition and dry deposition) as described in Su and Toon (2009). Dust aerosols are scavenged both by rain and snow including below-cloud and in-cloud scavenging for each model layer in a manner that is size and composition independent (Barth et al., 2000; Rasch et al., 2001; Su and Toon, 2009). The dry deposition includes sedimentation near the surface (which dominates for coarse mode particles) and turbulent mix-out (which dominates for fine mode particles). The sedimentation fall velocities are calculated in CARMA2.3 by Stokes law at low Reynold's number (Re < 1). Corrections are made at high Reynold's numbers (Re > 1) based on Prupacher and Klett (1997). We modified the dry deposition scheme following Marticorena and Bergametti (1995) and Ginoux et al. (2001) to account for both the bin-resolved dust particles and the effect of soil moisture on dust lifting (Su and Toon, 2009).

A systematic assessment of the model simulations has been done in Su and Toon (2009). We validated the simulations against observations from the ACE-Asia field campaign. We also used observational datasets including AERONET data at six study sites as well as the NIES lidar data to constrain the model simulations in Su and Toon (2009).

3.3 The CALIPSO and AERONET Data

CALIPSO was launched in April 2006 (Liu et al., 2006; Winker et al., 2007). The Cloud –Aerosol Lidar with Orthogonal Polarization (CALIOP) instrument, on CALIPSO, is a two-wavelength (532 and 1064 nm), polarization-sensitive (at 532 nm) instrument. CALIOP provides substantial and unique information on vertical and geographical distributions of clouds and aerosols. CALIOP conducts nearly continuous observations of height-resolved attenuated backscatter over the globe (Sassen 2000; Winker et al.,

2003). We use CALIPSO profile level 1B data and the CALIPSO cloud layer level 2 data in this chapter.

The Aerosol Robotic NETwork (AERONET) is a globally distributed remote sensing aerosol-monitoring network of ground-based sun photometers that measure sun and sky radiances in 16 spectral channels (340-1640 nm) (Holben et al., 1998). AERONET provides observations of aerosol optical depth (AOD), as well as inversion products such as size distribution, single scattering albedo, and precipitable water. We use the cloud-screened and quality-assured AERONET Level 2.0 data in this chapter (Smirnov et al., 2000).

3.4 Results

3.4.1 Comparison of Dust Abundance and Fluxes over the Atlantic and Pacific, and Seasonal Variations

Here we address the problem of why the optical depths of dust over the Pacific and Atlantic are so different. Figure 3.1 shows the daily-averaged and column-integrated spectral optical depth at 500nm at Osaka in the Pacific in May 2007 (top) and at Capo Verde in the Atlantic in July 2007 (bottom) both from our model and from AERONET data. In general, the optical depth is higher over the Atlantic at Capo Verde than over Pacific at Osaka at similar downwind distances from the two dust sources even during the primary months of dust storm activity (such as May in Asia and July in the Sahara). The monthly-averaged optical depth is 0.382 and 0.339 over the Pacific at Osaka in May 2007 for AERONET data and the model simulation, respectively. However, the monthly-averaged optical depth is 0.613 and 0.579 over the Atlantic at Capo Verde in July 2007 for AERONET data and model simulation, respectively

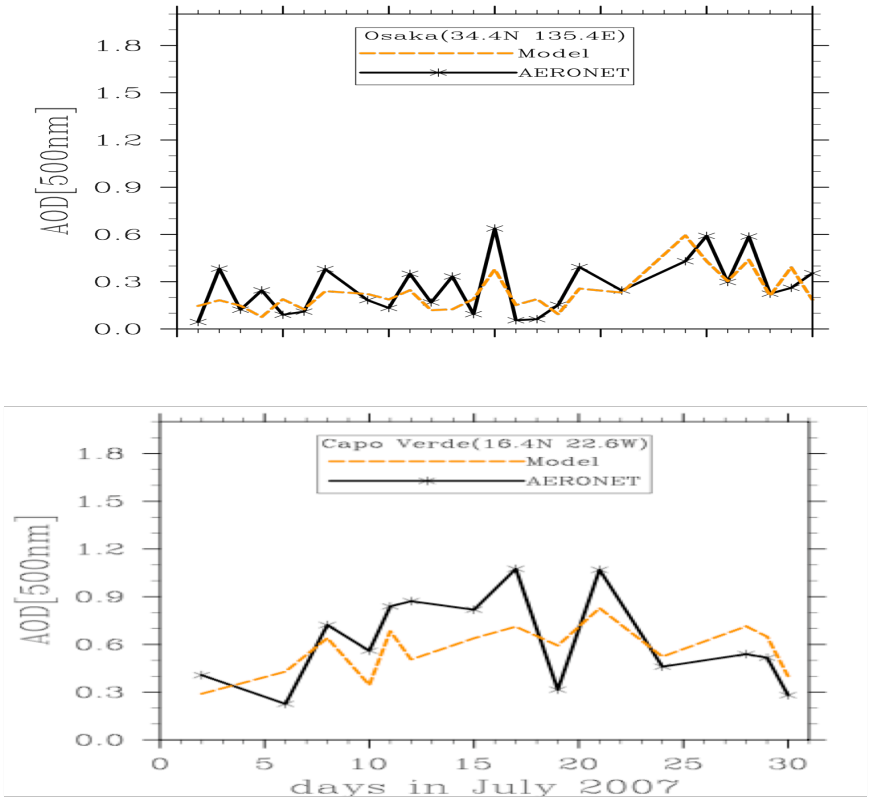

Figure 3.1 The daily-averaged and column-integrated spectral optical depth (500nm) at Osaka in May 2007 (top) and at Capo_Verde in July 2007 (bottom) both from our model and from AERONET data.

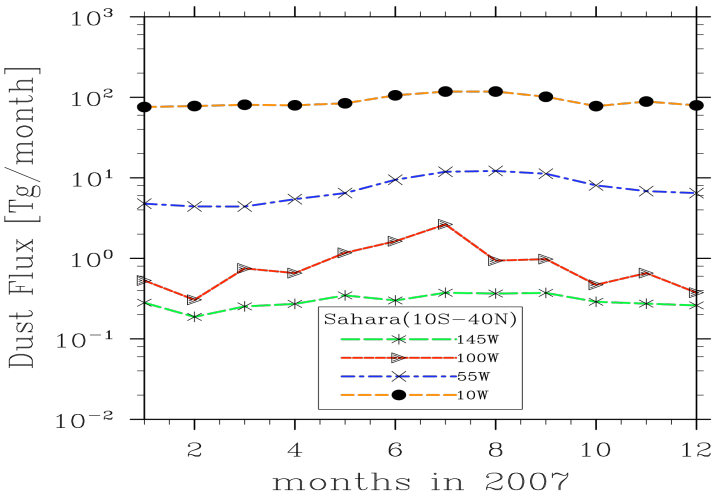

Figure 3.2 Modeled monthly dust flux between 10S-40N, across different longitude planes (10W, 55W, 100W, and 145W) for Saharan dust in 2007.

The dust fluxes into the two ocean basins tell a similar story to the one told by the optical depths. Figure 3.2 shows the modeled dust fluxes for the Sahara in 2007 from 10S - 40N latitude across four different longitude planes at 10W, 55W, 100W, and 145W. Figure 3.3 shows the map used in this chapter for Saharan dust. The dashed lines denote the four longitude planes (10W, 55W, 100W, and 145W) and the latitude boundaries (10S to 40N) at which dust fluxes were computed. We choose the latitude range between 10S to 40N based on previous studies using the GEOS-Chem model and CALIPSO analysis (Generoso et al., 2008; Liu et al., 2008b) suggesting that most Saharan dust plumes occurred and were transported downwind within this area. These longitudes span the distance from the Saharan dust source regions, across the Atlantic, over the Caribbean and into the Pacific. The net dust flux (orange dashed line in Figure 3.2) crossing the 10W plane (10S-40N) at the western edge of the Saharan Desert is about 90Tg for each month and is about 110Tg per summer month when the flux is greatest. The annual net flux is about 1088 Tg across the 10W plane in 2007 (orange dashed line in Figure 3.2). The flux across the 10W plane is about 70% of the total amount of Saharan dust (1547 Tg) lifted in the model for the year 2007. About 6% of the dust (93 Tg) goes north toward Europe in the model. Another 3% of the dust is lifted to the west of the 10W plane. The remainder of the dust (about 21% of that lifted) is removed locally over the Sahara before it can reach the 10W plane.

The Saharan Desert is located in the tropics and sub-tropics, and usually experiences deep convection throughout the year. Strong winds embedded in the tropical trades (northeasterly flow) continually lift dust from the surface of Saharan Deserts. The dust outbreaks are contained in a deep mixed layer. The deep mixed layer usually extends to 5-6 km or higher in altitude over the Saharan Deserts due to the strong solar heating (Prospero et al., 1972 and 1981; Karyampudi et al., 1999; Colarco et al., 2003b). This hot and dry air mass is advected west of Africa and referred to as the

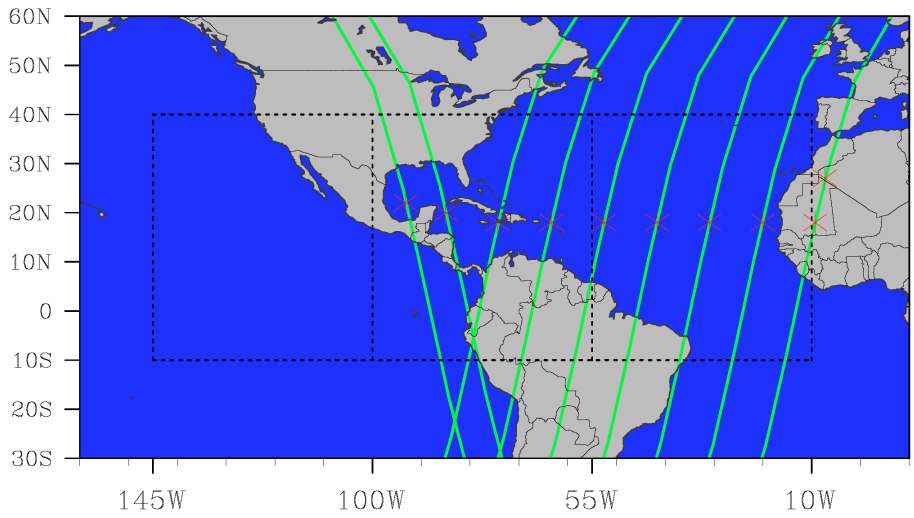

Figure 3.3 Map used in this chapter for Saharan dust. The dashed lines denote the four longitude planes (10W, 55W, 100W, and 145W) and the latitude boundary (10S to 40N). The CALIPSO tracks are shown as lines along the asterisks.

Saharan Air Layer (SAL). Dust lifting over African can be triggered and modulated by synoptic systems, such as African easterly waves in the Atlantic region (Prospero and Carson, 1972; Westphal et al., 1987; Jones et al., 2003). The dust outbreaks usually occur in the ridge of passing easterly waves with a period of 5-7 days (Prospero and Carson, 1972). The African easterly waves are identified through filtered (2.5-10 days) relative vorticity at 700 hPa over the tropical Atlantic Ocean. About 20% of the dust entrainment into the atmosphere is related to easterly wave activity, and approximately 10%-20% of the seasonal variation of Saharan Desert dust transported across the North Atlantic Ocean is regulated by easterly waves (Jones et al., 2003).

Figure 3.2 and Figure 3.4 show that about 90% of the dust is removed by the time it reaches 55W. During most months of the year only about 1% of the dust reaches as far as 100W, the longitude of Mexico. However, in the summer of 2007 our model

indicates a relatively larger dust flux (around 1.9Tg/month, 3.6% of total dust flux) reached the west coast of the Caribbean Sea (the 100W plane red curve in Figure 3.2). These dust fluxes are qualitatively consistent with previous studies. Colarco et al. (2003b) and Doherty et al. (2008) indicate each summer large amounts of Saharan dust are transported across the Atlantic Ocean and arrive in Caribbean Sea. The Saharan dust transport into the Caribbean is controlled primarily by a semi- permanent high, the Azores High (also called North Atlantic High), which usually extends westward toward Bermuda. This anticyclone becomes stronger and moves north in summer, and it moves south and becomes weaker in winter. The longitudinal displacement of the Azores High is highly related to the Saharan dust transport into the Caribbean.

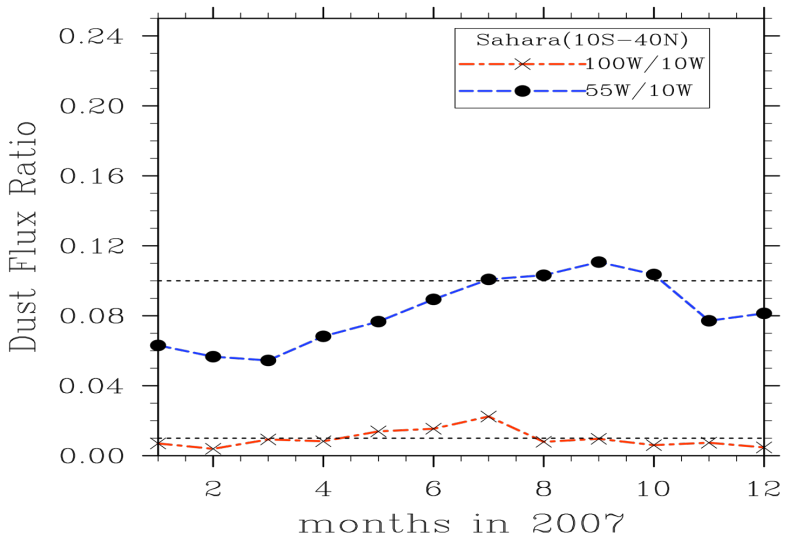

Figure 3.4 Modeled monthly mean dust flux between 10S to 40N. The asterisk-marked line denotes the ratio of the flux as 100W to that at 10W, and the blue dashed-line denotes the ratio of the flux at 55W to that at 10W for Saharan dust in 2007. The dashed lines mark 0.1 and 0.01.

Figure 3.2 also shows that the far-most plane over the Pacific at 145W (the asterisk marked dash-line) indicates a significant loss of dust between 100W and 145W in the months of June, July and August. The amount of loss in this longitude region is related to the position of the Inter-tropical Convergence Zone (ITCZ). During summer the ITCZ moves into latitudes near 10N, and there is significant convection over Central America due to the frontal zone of the ITCZ bringing the warm, moist air from the Gulf of Guinea into the hot, dry Saharan air to the north. This convection is quite efficient at removing the dust (Pfister et al, 2010). However, during other parts of the year there is less convection over Central America and our model suggests that dust is more likely to reach the Pacific.

Figure 3.4 presents the modeled monthly dust flux between 10S to 40N for 2007 at various longitudes as a fraction of the flux at 10W. The 55W to 10W ratio shows a monthly variation that may be related to the position of the Azores High as we discussed earlier. Generoso et al. (2008) estimated 151 Tg of dust was deposited in 2006 in the area bounded by 5N-27N and 17W-100W. We similarly find that total annual dust deposition in the tropical

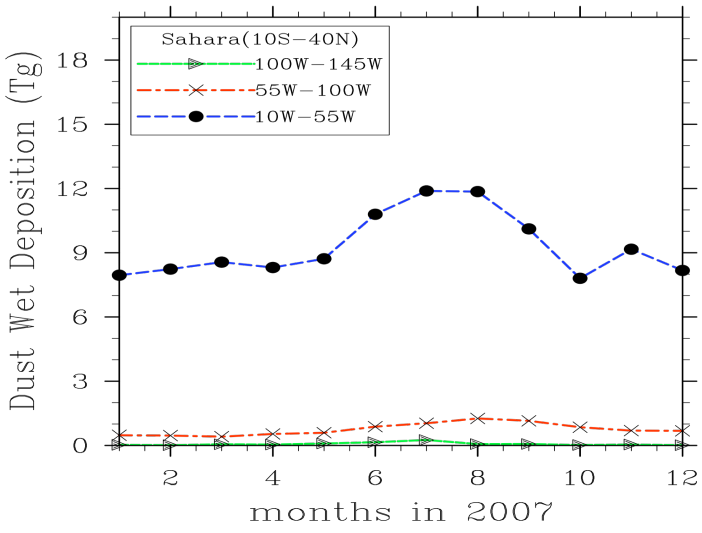

Figure 3.5 Modeled monthly dust wet deposition between 10S to 40N for longitudes between 10W to 55W, 55W-100W, and 100W-145W for Saharan dust in 2007.

Atlantic in the area bounded

by 5N-30N and 17W-100W is about 163 Tg in 2007.

Figure 3.5 shows the modeled annual dust wet deposition between 10S to 40N for 10W-55W, 55W-100W, and 100W-145W for Saharan dust in 2007. The annual total of the dust wet deposition over 10S to 40N and 10W to 145W is 122Tg based on the model simulations. Over the year there are about total 112 Tg (10% of total annual dust flux of 1088 Tg crossing the 10W plane), 9 Tg (10% of total annul dust flux of 92 Tg crossing the 55W plane), and 0.8 Tg (8% of total annual dust flux of 11.09 Tg crossing the 100W plane) of dust removed during transport between 10W and 55W, 55W and 100W, 100W and 145W, respectively, by wet deposition. Therefore the results of our model simulation indicate that 10% of total dust crossing 10W is deposited before it reaches the 145W plane in 2007 by wet removal, of which about 60% of the wet

Impact factors (annual average)	**Asian dust** (total dust flux across source plane is 355Tg in 2007)	**Saharan dust** (total dust flux across source plane is 1087Tg in 2007)
Wet deposition	15%	10%
Dry deposition	75%	80%
Soil Erodibility Factor	0.077	0.081
Area of sources	2.07×10^6 km^2	8.95×10^6 km^2
Area lifting occurs	1.33×10^6 km^2	4.17×10^6 km^2
Power averaged wind	4.2 m/s	5.1 m/s
Soil moisture	0.1 mm^3/mm^3	0.03 mm^3/mm^3
Snow	2.5×10^{-5} mm/s	0

Table 3.1 The factors that contribute to the magnitudes of the total dust fluxes both for Asian and Saharan dust simulated from the coupled CAM3.0/CARMA2.3 model in 2007. The % in the first two lines (wet and dry deposition) refers to the fraction of the dust removed before traveling 45 degrees of longitude from the sources.

deposition occurs in summer. There is less wet deposition in spring and autumn. Our study suggests that the wet removal process is a minor contributor to the total dust loss over the Atlantic (see Table 3.1).

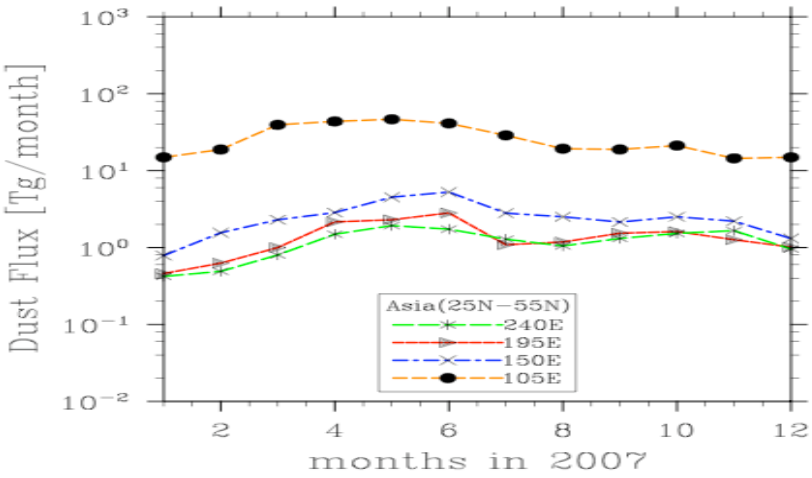

Figure 3.6 Modeled monthly dust fluxes (25N-55N) across different longitude planes (105E, 150E, 195E, and 240E) for Asian dust in 2007.

Figure 3.6 shows the modeled annual dust fluxes (between 25N-55N) across different longitude planes (105E, 150E, 195E, and 240E) for Asian dust in 2007. Figure 3.7 shows the map used in this study for Asian dust. The dashed lines denote the four longitude planes (105E, 150E, 195E, and 240E) and the latitude boundaries (25N to 55N). We chose the latitude range between 25N to 55N based on previous modeling and observational studies showing that most Asian dust plumes occurred and were transported downwind within this area (Eguchi et al., 2003 and 2009; Huang et al., 2008). The total dust flux (orange dashed line in Fig. 6) across the 105E plane, which crosses central Mongolia in the Asian deserts, is 355Tg in 2007. Only about 4% of the total dust lifted over Asia comes from the east of 105E. Figure 3.2 showed an annual dust flux across 10W from the Sahara of about 1088 Tg in 2007. Therefore, about 3

times as much dust was transported downwind of the Sahara desert in 2007, as downwind of the Asian deserts. Unlike the case for the Sahara, there is a strong seasonal variation in Asian dust fluxes. We find that 62% of the 355 Tg lifted is generated in the months March-June. Eguchi et al. (2003) reported that the dust transported through the longitudinal cross-plane at 90 E is approximately 34.1 Tg for a period of 5-15 May 2007 based on a 3-D aerosol model. Our model estimates about 36.4 Tg within the same latitude region between 25°N -55°N.

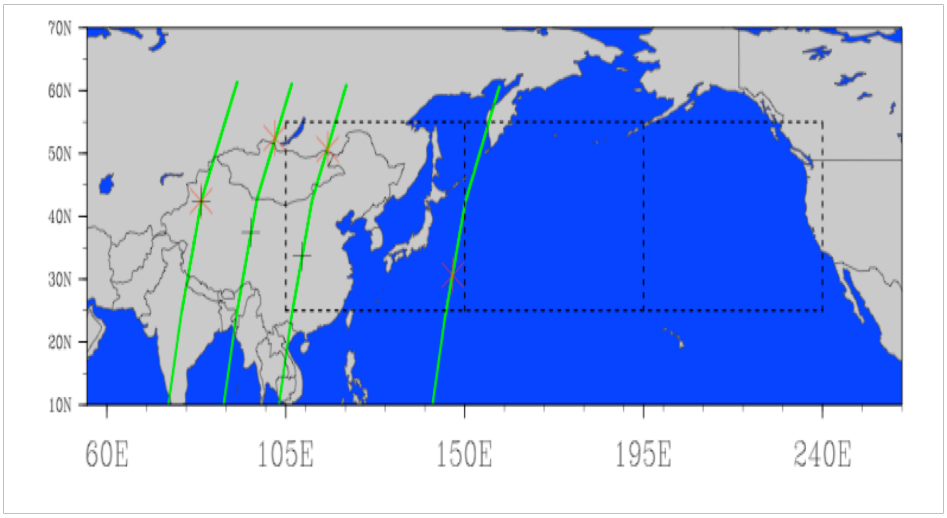

Figure 3.7 Map used in this chapter for Asian dust. The dashed lines denote the four longitude planes (105E, 150E, 195E, and 240E) and the latitude boundary (25N to 55N). The CALIPSO tracks are shown as lines along the asterisks and cross marks.

The seasonal variation of dust outbreaks over Asia is associated with variation in the wind speed (Shao and Dong, 2006), the surface vegetation (Lee and Sohn, 2009), and the soil moisture and snow cover (Laurent et al., 2006). Strong winds occur most frequently in spring in Asia due to the activity of mid-latitude frontal systems. The mid-latitude cyclones associated with intense cold fronts from Mongolia to northeastern China not only generate dust storms, but also lift Asian dust into the westerly jet in the

free atmosphere. There is no equivalent of the SAL over Asia, though some of the dust is transported in a relatively shallow boundary layer. Deep dry convection is a major feature of Saharan Deserts (Cuesta et al., 2009). The mixed boundary layer depth and the tropopause altitude above the low-latitude tropical surface of Africa are higher than at mid-latitudes in Asia. Thus the springtime weather in Asia produces intense dust storm events in which dust is transported along the direction of the westerly winds. However, this transport is not associated with a deep convective boundary layer, as it is for Saharan dust.

The dust emission over the Asian dust source regions is substantially suppressed after spring not only due to the weaker Mongolian cyclonic activity but also because of the increasing vegetation (Lee and Sohn, 2009). Laurent et al. (2006) indicates that the soil moisture and snow cover in the northern deserts of China decreases the dust emission by 94% and 84%, respectively, in winter but the dust emissions of Taklimakan desert are not noticeably influenced by the soil moisture and snow cover due to low precipitation and snowfall.

Figure 3.8 presents the monthly dust flux between 25N to 55N latitude across 240E and 150E longitudes as a fraction of the flux across 105E. Figure 3.8 shows that only about 10% of the dust lifted reaches the longitude of Japan (150E) and only 5% reaches the West coast of the U.S. (240E). This large mass loss suggests that the removal processes (including wet and dry deposition) play an essential role during the Asian dust transport to 150E. Like Sahara dust there is a low layer of Asian dust that is rapidly removed by deposition. However, the relatively small dust particles lifted from the dust source that are entrained into air at high altitude (up to 10km) can be transported via upper tropospheric westerly jets over long distances as has been pointed out from observations by Stith et al. (2009). Once dust passes Japan, removal is less important. Eguchi et al. (2009) reported that about 30% of dust crossing 140E is transported

eastward and arrives in the North America based on the CALIPSO and SPRINTARS model analysis, which is consistent with our model simulations of 40% of Asian dust crossing 150E reaching the west coast of America.

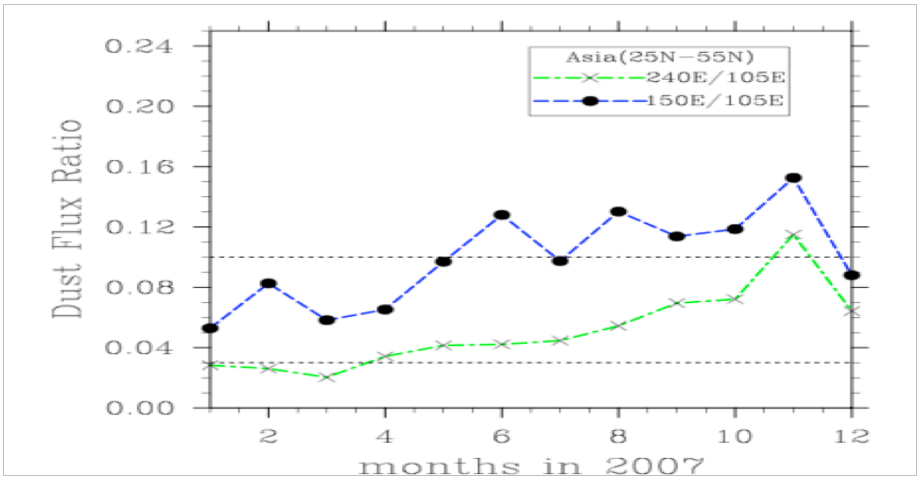

Figure 3.8 Modeled ratios of monthly dust flux between 25N to 55N for Asian dust in 2007. The horizontal dashed lines are the 0.1 and 0.03 lines.

The dust flux ratios in Figure 3.8 are lowest in the months from December to May. This seasonal variability means there is preferential dust removal during the same period when dust is lifted over Asian deserts. This overlap occurs because the low pressure centers over the Asian deserts are not only responsible for the strong winds needed for the dust lifting, but also act as sources of rain needed for dust removal. This is a different phenomenon than for Sahara dust.

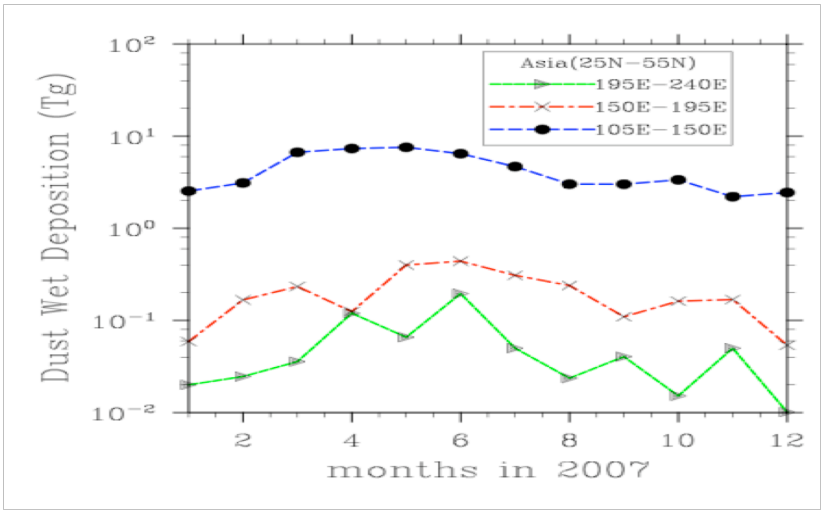

Figure 3.9 Modeled monthly dust wet deposition between 25N to 55N for regions between 105E to 150E, 150E to 195E, and 195E to 240E for Asian dust in 2007.

Figure 3.9 shows the modeled annual dust wet deposition between 25N to 55N for 105E to 150E, 150E to 195E, and 195E to 240E for Asian dust in 2007. The dust flux is correlated with the wet removal. In part this is because the same systems that lift the dust, bring rain. About 52 Tg (15% of dust crossing the 105E plane) of dust is removed during transport from 105E to 150E by wet deposition on an annual average. The results of our model simulation indicate that more dust is wet deposited during spring and summer, than in autumn and winter. This study also suggests that wet removal process plays a larger role in dust removal for Asian dust (15% of dust crossing the 105E plane) than Saharan dust (10% of dust crossing the 10W plane). This larger loss is due to the abundant rainfall over Asia (especially in spring and summer) leading to greater local dust removal than over the Sahara.

The dust mass flux from the Sahara in 2007 is about 3 times greater than that from Asia across a plane that is 45 degrees longitude from the source. Table 1 shows the factors that contribute to the differences of the total dust fluxes between Asian dust

and Saharan dust as simulated from the coupled CAM3.0/CARMA2.3 model in year 2007. We can see the wet and dry deposition processes have similar magnitudes for Asian and Saharan dust. Although most of the dust is removed in transport over these distances, deposition is not the major mechanism causing the differences in the total dust fluxes between the two dust sources. The soil erodibility factor (the fraction of the grid cell for which dust lifting occurs if the threshold wind velocity is exceeded) is not a function of time in the model. There are the similar values of the area averaged soil erodibility factor (0.078 for Asian deserts and 0.081 for Saharan deserts). The total areas of the dust sources are 2.07×10^6 km^2 and 8.95×10^6 km^2 for Asian deserts and Saharan deserts, respectively. However, the annual averaged areas over which dust lifting occurs (when wind exceeds the threshold velocity, which is related to the particle size distribution and soil moisture) are 1.33×10^6 km^2 and 4.17×10^6 km^2 for Asian deserts and Saharan deserts, respectively, based on the model simulations. The areas over which dust lifting occurs in various seasons in Saharan deserts are 3.97×10^6 km^2 (spring), 4.53×10^6 km^2 (summer), 4.25×10^6 km^2 (fall), and 3.94×10^6 km^2 (winter). The areas over the Asian deserts are 1.67×10^6 km^2 (spring), 1.15×10^6 km^2 (summer), 1.20×10^6 km^2 (fall), and 1.31×10^6 km^2 (winter). Therefore the different areas over which dust is lifted contributes about a factor of 3 to the difference in total dust lifting between the two sources in 2007. A factor of three is also about the difference in the spring and summer lifting between the Sahara and Asia, so that the area over which dust is lifted dominates the difference between the amounts of dust lifted. We also calculated the seasonal mean power-averaged wind over the dust lifting areas. The amount of dust lifted in the source function is directly proportional to the power in the wind. The values of the power-averaged winds are 4.9 m/s (spring), 5.5m/s (summer), 5.3 m/s (fall), and 4.7 m/s (winter) for Saharan deserts. And the values of the power-averaged winds are 4.9 m/s (spring), 3.6m/s (summer), 4.0 m/s (fall), and 4.3 m/s (winter) for Asian deserts. So the

annual-averaged and power averaged winds for Asian deserts and Saharan deserts are 4.2 m/s and 5.1 m/s, respectively. The wind speeds are the same between the Sahara and Asia in the spring, so when Asia has most of its dust events it is the area of the source that dominates the difference between Asian and African dust fluxes. However in other times of the year low winds speeds cause Asia to be a less important dust source. Over the year, wind speed contributes about a factor of 1.7 (the lifting depends on the third power of the wind) to the differences of the total dust fluxes between the African and Asian sources. Soil moisture and snow can be seen as restricting the area of the dust sources, or the magnitude of the dust lifting. The soil moisture (the volumetric soil water in the model) is different between the two sources with an annual mean value of 0.1 mm^3/mm^3 for Asian deserts and 0.03 mm^3/mm^3 for Saharan deserts (Table 1). The dust flux is not linearly proportional to the soil moisture. Soil moisture contributes about a factor of 10% to the total dust flux differences between the two sources. Other factors that affect the dust flux differences between the two sources can be snow and vegetation (the annual total snow is 778 mm over Asian deserts in 2007 and it is around zero for Saharan deserts in 2007 in the model). Snow and vegetation limit the area of dust lifting, not the magnitudes of dust lifting in our model.

4.2 Dust Vertical Distribution

We would like to know if Asian and African dust has the same vertical distribution, and to understand how the vertical distribution of dust impacts the downwind transport and properties of dust. As we noted in the previous section the removal over 45 degrees of longitude is similar for Africa and Asia. However, because these deserts are at different latitudes, the times to go these distances are shorter by about 20% for the Asian dust, assuming the wind speeds are similar. However, the mean wind speed at

30N-50N latitude is higher than at 10N-30N latitude, so in fact the Asian dust is traveling faster than the Saharan dust and so has even less time to be removed. In net the Asian dust has about 25% less time to be removed than the African dust considering both distance and wind speed. We compare the vertical distribution of Saharan dust with that of Asian dust and explore how each evolves downwind of their respective source. We use data from the CALIOP instrument on CALIPSO for this comparison.

We investigated a case study of dust transport for Saharan dust and one for Asian dust. Over the tropical and subtropical regions the cloud coverage is very high, which makes it hard to acquire enough cloud-free profiles to create case studies. Due to the availability of CALIPSO measurements, we take Aug. 17 to Aug. 28 of 2006 as an example of Saharan dust, and May 07 to May 10 of 2007 as an example of Asian dust.

CALIPSO profile level 1B data contains measurements of Total Attenuated Backscatter at 532nm (TAB_532) and of Perpendicular Attenuated Backscatter at 532nm (PAB_532). Following Fernald et al. (1972 and 1984), Young et al. (2008), Liu et al. (2008b), and Cuesta et al. (2009), the dust vertical extinction (km^{-1}) at 532nm can be calculated (here we assume the aerosol layer is homogeneous along the laser beam) by

$$\alpha_{532} = \frac{\beta_{532r} \times S_{532}}{\exp(-2 \times \alpha_{532} \times \Delta z)} \qquad (3.1)$$

Where β_{532r} is the total attenuated backscatter at 532nm ($km^{-1}sr^{-1}$), α_{532} is the vertical extinction (km^{-1}), S_{532} is the lidar ratio (44 for this study based on Liu et al. (2006)), and Δz is the detected layer height. We also screen out the cloud from CALIPSO profile level 1B data based on the CALIPSO cloud layer level 2 data based on Liu et al. (2008b). Nighttime CALIPSO measurements primarily are used in this study because

they have less noise. However we use the daytime data for Aug. 25 and 28 because the nighttime data are not available. We expect additional solar background noise in measurements on these two days.

Figure 3.3 shows the map of CALIPSO tracks for Saharan dust used in this study (Aug. 17 to Aug. 28 of 2006). The asterisks indicate the dust transport path for Saharan Deserts from Aug. 17 (most easterly asterisk) to Aug. 28 (most westerly asterisk) of 2006. It should be noted that there are two dust plumes on Aug. 17 of 2006 (as two asterisks denoted), which merged together before it begins its long-range transport across the Atlantic on Aug. 18 of 2006. We averaged these two profiles on August 17. We used the Hybrid Single-Particle Lagrangian Integrated Trajectory (HYSPLIT) model (Draxler and Rolph, 2003) (http://www.arl.noaa.gov) to trace the downwind evolution of Saharan and Asian dust. The HYSPLIT model can be configured to compute air parcel trajectories for complex dispersion and deposition simulations based on the wind fields from the National Center for Environmental Prediction (NCEP) analyses. We averaged the CALIPSO data every 120-laser shots over about 40 km along the track around the regions marked by asterisks. Figure 3.10 presents the results of the comparison of the vertical distribution (extinction at 532nm) of Saharan dust between the model (solid marked lines) and CALIPSO data by Eq. (3.1) (dashed lines) from Aug. 17 to Aug. 28 of 2006. The simulated dust vertical distribution of Sahara dust is generally consistent with CALIPSO (lidar) retrievals. However, on some days, such as from Aug. 19 to Aug. 23 the model does not capture the sharp layer top that is observed by CALIPSO. Probably the model lacks enough vertical resolution to fully resolve the layer top. However, it is also possible that the upper parts of the layer have been advected horizontally away from the lower parts and the model has not properly captured that transport.

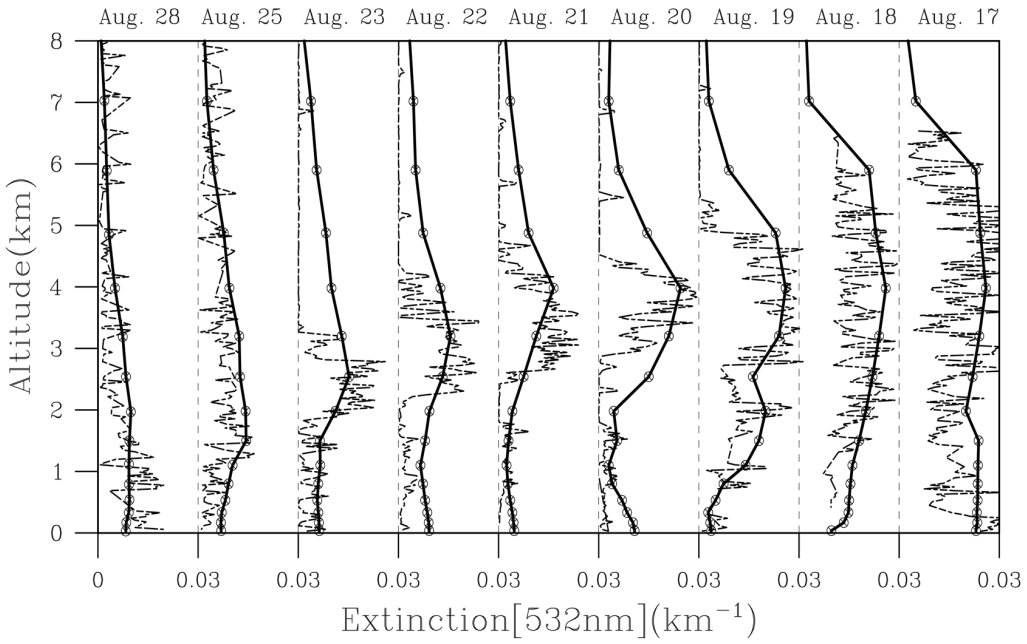

Figure 3.10 Comparison of vertical distribution of Saharan dust between model simulations and CALIPSO observations in August of 2006.

The Sahara dust layers descend over time with the top altitude starting at about 7km on Aug. 17 and reaching the marine boundary layer on Aug. 28. The typical magnitude of the vertical extinction (vertical average through the dust layer) decreases from 0.023 km^{-1} (averaged from the CALIPSO data) and 0.027 km^{-1} (averaged from the model) on Aug. 17 to 0.01 km^{-1} (averaged from the CALIPSO data) and 0.007 km^{-1} (averaged from the model) on Aug. 28. The dust resides in a well-mixed layer about 2km thick (between 1 to 3km in altitude) as it advects west and enters the Caribbean Sea on Aug. 23. Colarco et al. (2003b) found a similar layer over the Caribbean but located between 3 to 5 km in altitude during the Puerto Rico Dust Experiment (June-July 2000).

The descent of the Saharan dust layers during transport was recognized previously by Colarco et al. (2003b) who suggested it was due partly to particle

sedimentation. On the other hand, Doherty et al. (2008) suggested the descent is dominated by vertical air motions. The Sahara Air Layer (SAL) is affected by the Azores high. The Azores High usually extends westward from the Azores toward Bermuda. It becomes stronger and moves north toward the Iberian Peninsula in summer. Descending air in the Azores High will cause the top of the SAL to descend as air is transported to the Caribbean Sea from West Africa. The transport of dust in the SAL

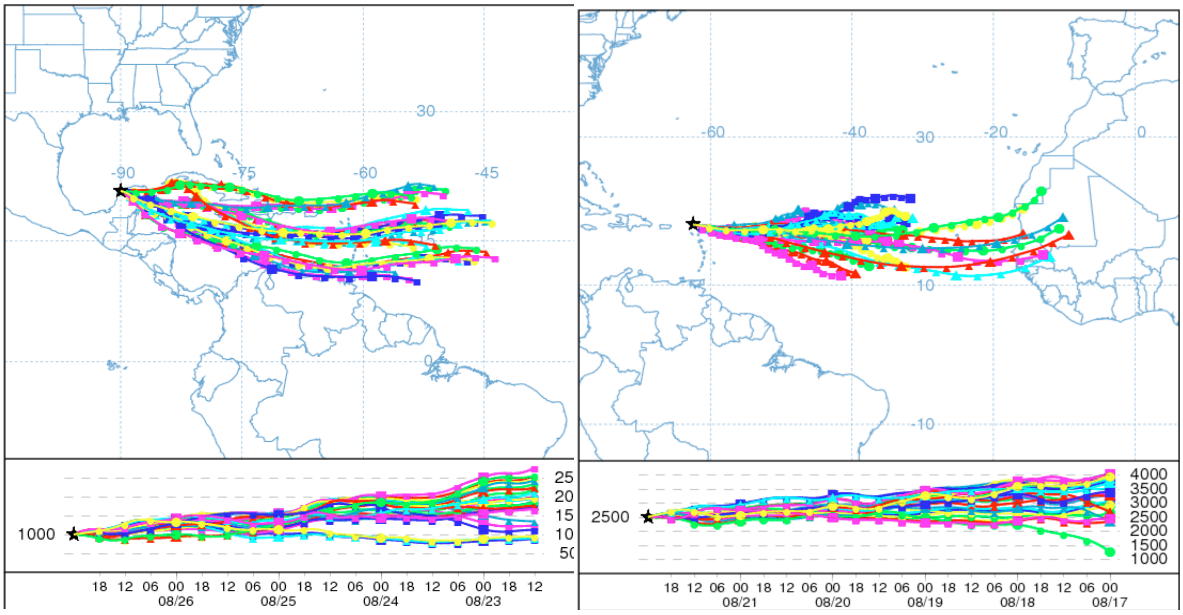

Figure 3.11 Back trajectory ensemble of Sahara dust for Caribbean Sea from 27 August to 22 August in 2006 (left) and from 22 August to 17 August in 2006 (right) using HYSPLIT model for altitude 1000m (left) and 2500m (right). The horizontal trajectory components (top) and the vertical components (bottom) are shown in the figures. We chose two back trajectory ensemble runs because the maximum ensemble run time of HYSPLIT is 120 h.

from West Africa to the Caribbean Sea took about one week (Aug. 17 to Aug. 25.). The mean vertical velocity of the dust descent is about 6.3 mm/s based on the vertical extinction profiles of Aug. 17 to Aug. 25, 2006. Liu et al. (2008b) found that the mean descending velocity of the top of the Saharan dust layer is about 6 mm/s for transport from the west coast of Africa to the Caribbean Sea based on depolarization profiles for these same days in August 2006. The HYSPLIT model showed that the SAL descended

between West Africa and the Caribbean Sea from Aug. 17 to Aug. 27 at about 4.0 mm/s (Figure 3.11). The difference between the dust descent rate (6.3 mm/s) and the air descent rate (4.0 mm/s) is consistent with the fall velocity of dust particles around 2 μm in size. Hence about one third of the descent rate of the dust is due to sedimentation and two thirds to the descent of the air in the case studied.

Figure 3.7 shows the map of CALIPSO tracks for Asian dust used in this study (May 07 (most westerly track) to May 10 (most easterly track) of 2007). The asterisk and the cross marks indicate two dust transport paths for Asian dust from May 07 to May 10 of 2007. We averaged 120-laser shots from CALIPSO over about 40km along the track both at the asterisk and cross mark points. The paths differ by the altitude of the dust layer. The track to the south was followed by dust below 3 km, and the track to the north by dust above 3 km. The transport paths are tracked by the HYSPLIT model. Vertical shear of the wind prevented a “SAL-like” layer from advecting away from the dust source.

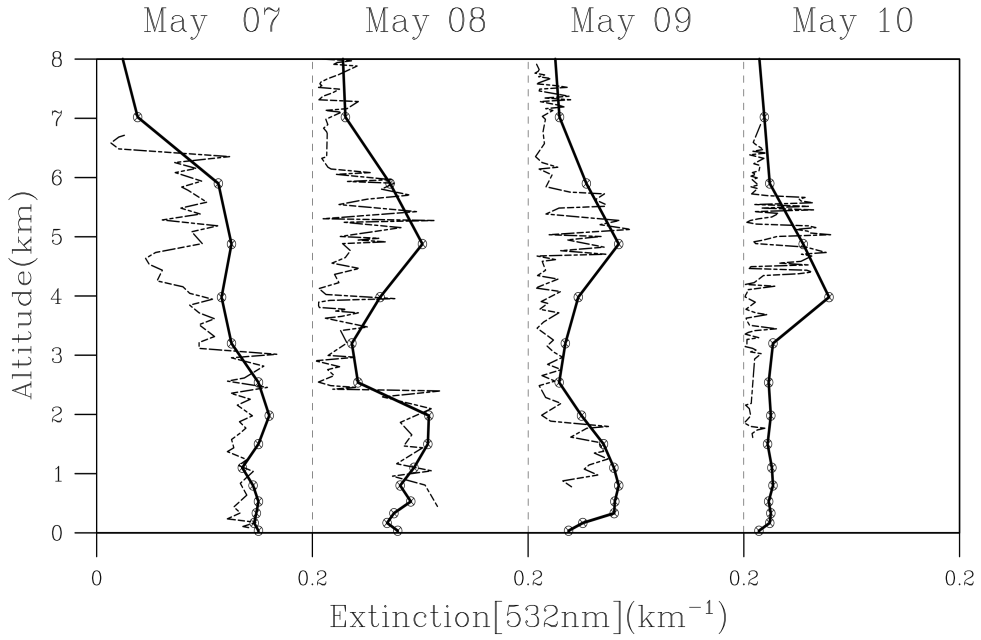

Figure 3.12 Comparison of vertical distribution of Asian dust between model simulations and CALIPSO observations in May of 2007.

The simulated dust vertical distribution of Asian dust is consistent with CALIPSO (lidar) retrievals (Figure 3.12). Asian dust shows multiple layers (two layers in the case studied) during transport. One layer is at the altitudes between about 4.5-6.5 km (and is located to the north along the asterisks in Figure 3.7) and shows little descent, while the other, lower layer top descends with time from 3km on May 07 to 1km on May 09 (there are no data available below 1 km on May 10 2007). The HYSPLIT model showed that the air between 4.5-6.5 km ascended at about 0.4 cm/s during transport from May 07 to May 10 of 2007 along the CALIPSO tracks (Figure 3.13). Such ascent is enough to compensate for the sedimentation of particles as large as 3-4 μm. This ascent is consistent with the mid-latitude frontal cyclones, which not only generate dust storms, but also lift Asian dust into the upper troposphere and transport it along the westerly jet.

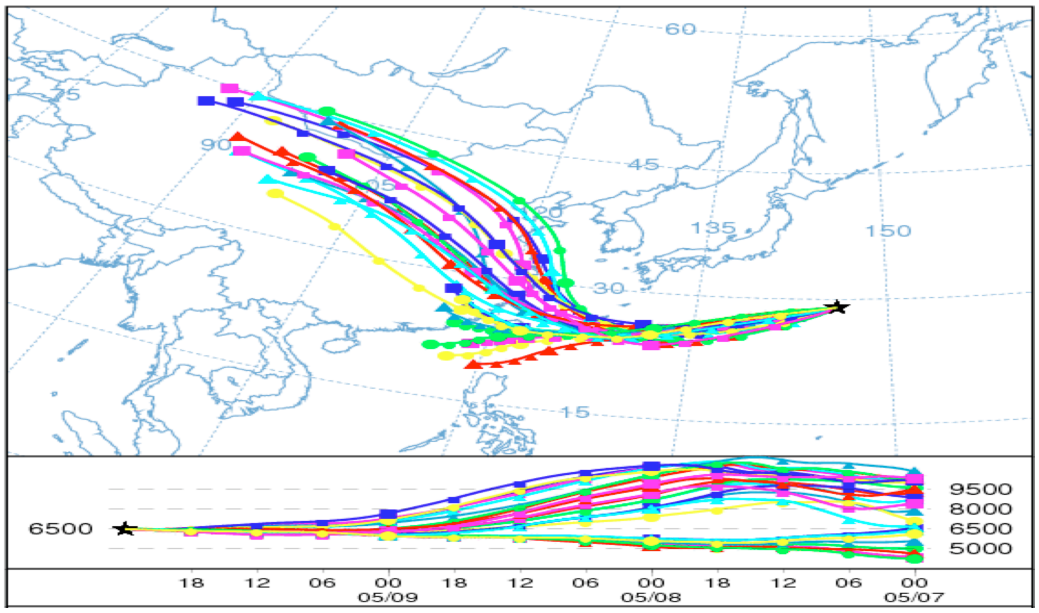

Figure 3.13 Back trajectory ensemble of Asian dust for Pacific Ocean from 10 May to 7 May 2007 using HYSPLIT model for altitude 6500 m. The horizontal trajectory components (top) and the vertical components (bottom) are shown in the figure. Note the back trajectory goes from right (the black star at Pacific Ocean) to left (Asian Desert) (top) and it goes from left (the black star at 6500 m) to right (multiple levels) (bottom).

The behavior of the upper and lower dust layers is consistent with results from Huang et al. (2008).

The magnitude of the vertical extinction for the higher layer decreases from 0.1km^{-1} (averaged from the CALIPSO data) and 0.12 km^{-1} (averaged from the model) on May 07 to 0.04 km^{-1} (averaged from the CALIPSO data) and 0.05 km^{-1} (averaged from the model) on May 10 2007. There is a larger magnitude change for the extinction in the lower dust layer, which changes from 0.135 km^{-1} (averaged from the CALIPSO data) and 0.15 km^{-1} (averaged from the model) on May 07 to 0 (averaged from the CALIPSO data) and 0.05 km^{-1} (averaged from the model) on May 09 2007.

In conclusion we find the vertical distributions of Asian and African dust are different. African dust is in a deep layer, the SAL, which descends at about 6 mm s^{-1} as it crosses the Atlantic. Asian dust does not form a deep layer, but is split by vertical wind shear into two layers in the case studied. Unlike African dust, the top layer shows no evidence of descent during transport.

3.4.3 Dust Size Distribution

The dust size distribution can be important for optical properties such as the wavelength dependence of the optical depth, and the single scattering albedo. Small particles (0.1 to 1.0 μm diameter) have larger scattering and absorbing cross sections per unit mass than large particles (Seinfeld and Pandis, 1998). We would like to know if Saharan and Asian dust particles have similar or different size distributions.

Figure 3.14 shows the 532-nm volume depolarization ratio from Saharan dust (around 15.02N, 6.90W) measured by CALIPSO on July 21which goes near the AERONET site at Dakar. The dust fills the SAL from the ground to about 6 km altitude. There are cirrus clouds around 10N, 8W at 11 to 14 km altitudes that are distinguished from dust by their

height and the fact that the lidar beam is almost totally attenuated beneath the cirrus. The volume depolarization ratio is computed from the total attenuated backscatter in the CALIPSO version 1 data products following Cairo et al. (1999) and Liu et al. (2008):

$$\delta(r) = \frac{\beta_{532,m,\perp}(r) + \beta_{532,p,\perp}(r)}{\beta_{532,m,\parallel}(r) + \beta_{532,p,\parallel}(r)} \tag{3.2}$$

Where $\beta_{532,m,\perp}(r)$ and $\beta_{532,p,\perp}(r)$ are the components of the backscatter signal polarized perpendicular to the polarization plane of the linearly polarized laser pulse due to the molecular scattering and particulate scattering at range r and at the laser wavelength 532nm, respectively. $\beta_{532,m,\parallel}(r)$ and $\beta_{532,p,\parallel}(r)$ are the components of the backscatter signal polarized parallel to the polarization plane of the linearly polarized laser pulse due to the molecular scattering and particulate scattering at range r and the laser wavelength 532nm, respectively. The values of the volume depolarization ratio of dust aerosols are usually between 0.06 to 0.3, whereas the ratio is below 0.06 (close to zero) for other aerosol types (Liu et al., 2008). The relatively high values of the dust

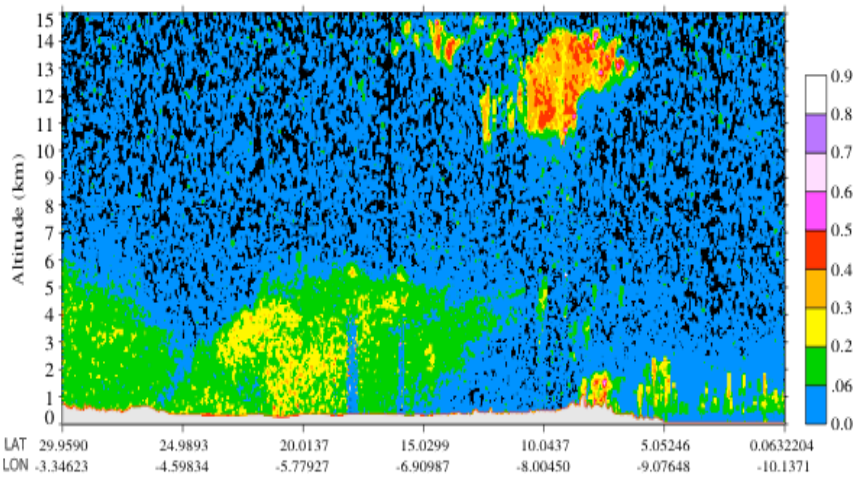

Figure 3.14 The 532-nm depolarization ratio for Saharan dust on 21 July 2007. Red characters “c” and “d” represent “clouds layers” and “dust plumes”, respectively.

depolarization ratios are due to the nonsphericity and large size of dust particles.

Figure 3.15 shows the dust depolarization profile for Asian dust on 23 May 2007. Dust extends to about 8 kilometers over the Gobi Deserts (between 45.0254N, 109.356E and 40.0556N, 107.684E) on 23 May 2007, but does not make a continuous layer to the surface.

We compare the dust size distributions between Saharan and Asian dust during dust outbreaks. Considering the availability of AERONET observations, we choose Dakar on 22 July 2007 and Xianghe on 24 May 2007, which are close to dust sources, to represent Saharan and Asian dust, respectively.

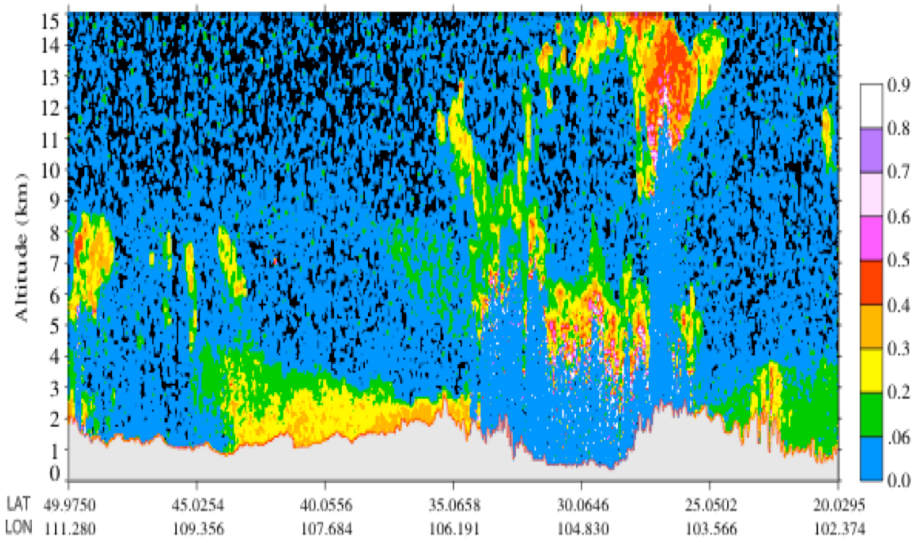

Figure 3.15 The 532-nm depolarization ratio for Asian dust on 23 May 2007.
Red characters “c” and “d” represent “clouds layers” and “dust plumes”, respectively.

Figure 3.16 and Figure 3.17 present the modeled volume size distribution of Saharan dust at Dakar and the modeled volume size distribution of Asian dust at

Xianghe, respectively. The model simulations are compared to AERONET measurements in each figure. The AERONET and modeled size distribution for Saharan dust in Fig. 16 show only one mode located near 1.0 μm for dust with radius larger than about 0.2 μm. The AERONET and modeled size distributions for Asian dust (Figure 3.17) shows two volume modes, one near 0.5 μm and one near 2 μm radius. It is interesting that the model reproduces both of these distributions even though it uses identical dust source functions in each case. These volume mode radii have been verified by previous field campaigns both in Asia and in Sahara. McNaughton et al. (2009) indicated that the mode volume radius of the Asian dust is around 2μm radius based on the analysis from in-situ sampling of tropospheric aerosol during spring of 2006 in Phase B of the Intercontinental Chemical Transport Experiment (INTEX-B). Nowottnick et al. (2010) also found that the mode volume radius of Saharan dust is around 1 micron radius based on sampling during the African Monsoon Multidisciplinary Analyses field campaign (August-September 2006). It should be noted that there are fine mode

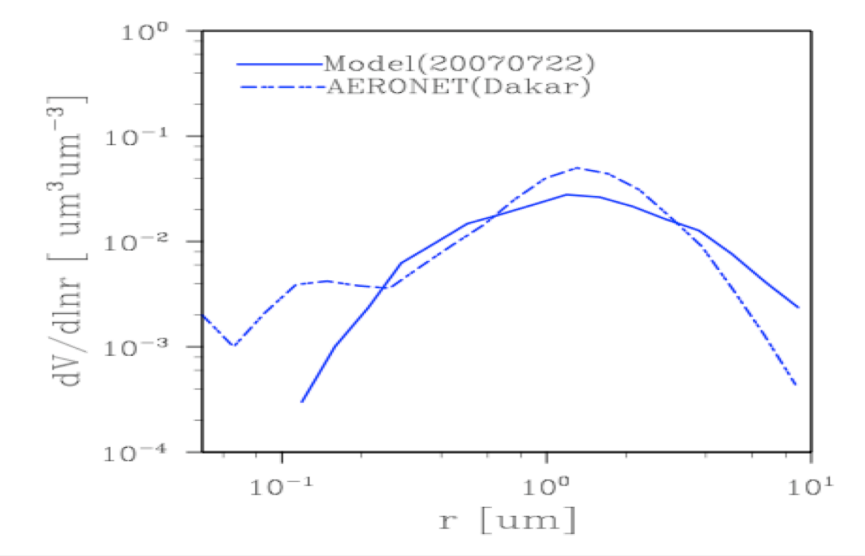

Figure 3.16 Modeled volume size distribution of Saharan dust in Dakar (14.39N, 16.95W) constrained by AERONET measurements.

particles (such as nitrate, sulfate, and black carbon) in the AERONET size distribution data in Figure 3.16 and Figure 3.17 (mode around 0.1 μm), but such particles have not been included in our model.

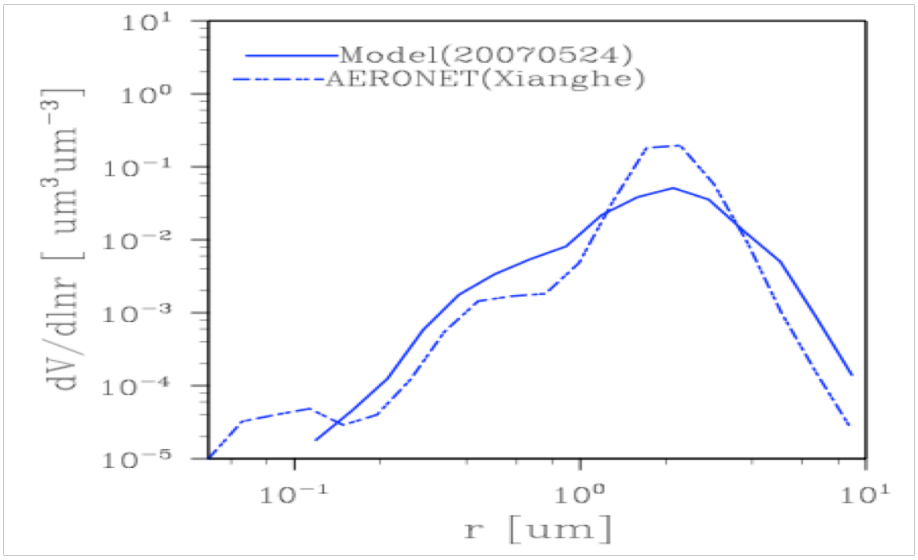

Figure 3.17 Modeled volume size distribution of Asian dust in Xianghe (39.75N, 116.96E) constrained by AERONET measurements.

We suggest that the reason for the different numbers of size modes and the different mode radius values between African and Asian dust is related to the difference in mixing and in vertical ascent of the dust in the atmosphere. Over the Sahara there is strong mixing throughout the deep mixed layer. Hence, while particles larger than about 1 μm are influenced by sedimentation, the remainder are well mixed so the size distribution is relatively unimodal. Over Asia, the mixing occurs only in a shallow layer, and there is some ascent in the cyclonic circulation which lifts the dust. Hence the size distribution is modified as particles larger than about 2 μm are able to fall against ascending air but smaller ones are not able to be removed by sedimentation.

We conclude that the particle size distributions in Saharan and Asian dust

advected away from the sources likely differ, but these differences can be modeled using the same set of dust lifting functions. The differences are not related to surface mineralology or lifting rates, but rather to different vertical velocities and turbulent mixing rates during transport.

3.4.4 Single Scattering Albedo

Figure 3.18 compares of the single scattering albedo between the model simulations and the AERONET retrievals both for Asian (Gobi) Desert (Dalanzadgad (43.3N, 104.3E)) in April 2006 and the Sahara Desert (Tamanrasset_TMP (22.5N, 5.3E)) in July 2006. We choose these two locations and time periods because they are close to the dust sources (while Dakar and Xianghe which we analyzed for size distributions are downwind of dust sources), which minimize potential effects from air pollution, and also have cloud-screened and quality-assured AERONET data. Unfortunately size distributions retrieved from the AERONET data were not available for these sites on these days.

For the model, we assume the real part of the complex refractive index (assumed to be 1.55) is independent of wavelength both for Asian dust and Saharan dust based on the AERONET retrievals (Dubovik et al., 2000; Lyamani et al., 2005) and previous studies (Patterson et al., 1977; Diaz et al., 2000; Liu et al., 2002). We use data on the imaginary part of the refractive index from AERONET site measurements at the dust source regions that should be dominated by relative pure mineral dust particles. In downwind regions other pollutants such as nitrate, sulfate, and black carbon may alter the single scattering albedo. The imaginary part of the dust refractive index is constrained by the averaged AERONET value in April of 2006 at Dalanzadgad (0.0027, 0.0022, 0.0017, 0.0013 with increasing wavelength at 440nm, 670nm, 870nm, and

1020nm, respectively) for Asian dust and in July of 2006 at Tamanrasset_TMP (0.0036, 0.0031, 0.0026, 0.0020 with increasing wavelength at 440nm, 670nm, 870nm, and 1020nm, respectively) for Saharan dust. Figure 3.18 shows that the averaged single scattering albedo is larger for Asian dust than the Saharan dust. This is consistent with previous work suggesting that the dust transported from Asia to the Pacific may not absorb as much light as the dust from the Sahara Desert (Sokolik and Toon, 1999). The Asian dust has a smaller imaginary refractive index than Saharan dust, which is main reason the Asian dust has a higher single scattering albedo near the source. The single scattering albedos may depend on size as well, particularly as the size distributions are modified downwind of the sources as discussed previously. It should be noted that some studies report much lower SSA values of Asian dust that in Fig.18 (Pandithurai et al., 2008, Ge et al., 2010). The small SSA values ranging from 0.74 to 0.84 at 500nm reported by Pandithurai et al. (2008) originated from New Delhi, India, where dust is likely mixed with absorbing anthropogenic aerosols. The Zhangye site studied in Ge et al. (2010) is the center of the Hexi Corridor in China, which is 618km to the south of Dalanzadgad. The small SSA values ranging from 0.76 to 0.86 between 415nm to 870nm in Zhangye reported by Ge to al. (2010) may also be explained by the local pollution.

3.5 Summary and Conclusions

Using our model we find that the yearly annual dust flux from Africa is about 3 times greater than that from Asia. In general, it is observed that the dust optical depth is higher over the Atlantic than over the Pacific at similar downwind distances from the two dust sources. The monthly-averaged optical depth is 0.382 and 0.339 over the Pacific at Osaka in May 2007 for AERONET data and model simulation, respectively. However,

the monthly-averaged optical depth is 0.613 and 0.579 over Atlantic at Capo Verde in July 2007 for AERONET data and model simulation, respectively. Hence even during peak months for dust lifting in Asia, smaller dust optical depths occur than during peak months in Africa.

The annual dust flux near the dust source is about 1088Tg/year across 10W (10S-40N, 10W) and 355Tg/year across 105E (25N-55N, 105E) for Sahara and Asia in 2007, respectively. Saharan deserts are largely south of 30N, while Asian ones are primarily north of 30N. This leads them to experience different meteorological regimes. Saharan dust lifting occurs all year long, primarily due to subtropical weather systems. The Saharan dust transport into the Caribbean is controlled primarily by a semi-permanent high, the Azores High. Dust lifting from African dust sources can be triggered and modulated by synoptic systems, such as African easterly waves. The dust outbreaks usually occur within the ridge region of passing easterly waves with a period of 5-7 days. In contrast, 45% of Asian dust was lifted in spring during the modeled year of 2007 when mid-latitude frontal systems lead to high winds. The seasonal variation of dust outbreaks in Asia is associated with the seasonal modulation of the wind speed. Strong winds occur most frequently in spring in Asia due to the activity of the mid-latitude frontal systems. The mid-latitude frontal cyclones associated with intense cold fronts from Mongolia to northeastern China not only generate dust storms, but can also lift Asian dust into the westerly jet in the upper troposphere.

Rainfall is more abundant over Asia during the dust lifting events than over the Sahara, leading to greater local dust removal than over the Sahara. However, wet removal is a small fraction of the total removal of dust, and removal processes do not account for the difference in annual dust flux between the Sahara and Asia. Instead, the Sahara simply has about three times as much area with dust lifting as Asia because Asia

has smaller deserts and also more vegetation and snow cover, which suppresses dust lifting.

During the major lifting season the power averaged winds over Africa and Asia are similar. However in other seasons Africa has stronger winds than does Asia, which further contributes to more dust lifting over Africa. The power-averaged wind contributes about a factor of 1.7 to the differences of the total dust fluxes between the two sources averaged over the year.

The vertical distribution of Asian and African dust also differs in the cases we considered. The Saharan dust is primarily located in a deep layer, the SAL. The top of the layer descends during transport, which we conclude is mainly due to descending air in the Azores High. There are two noticeable layers of Asian dust during transport in May. One layer stays well above boundary layer, and does not descend with time. The other dust layer is in a shallow near surface boundary layer and descends with time. The transport of Asian dust is dominated by the westerlies at high altitudes, while it is controlled by regional weather systems and topography at lower altitudes. Sedimentation does not seem to play a significant role in the descent of long lasting layers. Horizontal wind shear can also play a role in creating elevated dust layers by moving dust horizontally, which is particularly important over Asia.

The size distribution of Asian dust (at Xianghe) is bi-modal while that of Saharan dust (at Dakar) is uni-modal. The volume size distribution of Asian dust peaks around 2 microns, whereas it peaks around 1 micron for Saharan dust. Both model simulations and the AERONET retrievals show similar patterns. We suggest these differences originate from mixing in the boundary layers, and the vertical winds that occur during transport. For the case we studied, winds over Africa were descending in a well-mixed deep boundary layer, while those over Asia were ascending and there was no deep boundary layer. The ascending winds may have strong enough to loft micron sized dust.

We assume the real part of the complex refractive index is independent of wavelength (1.55) both for Asian dust and Saharan dust based on the AERONET retrievals and previous studies. We use data on the imaginary part of the refractive index from AERONET site measurements near the dust source regions. We find that the average single scattering albedo is larger for Asian dust than the Saharan dust. This is consistent with the refractive indecies inferred by AERONET for the two dust sources, and with a previous study that the dust transported from Asia to the Pacific may not absorb as much light as the dust from the Sahara. As the size distribution evolves downwind of the sources due to the vertical winds experienced during transport, and as pollutants are added to the dust, the single scattering albedos will evolve.

Chapter 4

Radiative Effects of Asian Dust on Climate Investigated with an Integrated Microphysical-Climate-Radiation Model

4.1 Introduction

East Asia has high aerosol optical depths that result partly from air pollution, and partly from desert dust. Here we explore the role that dust plays in the climate and radiation budget of China, and the surrounding countries. There are large uncertainties in estimating the radiative effects of dust on climate. Dust affects both the longwave and shortwave radiation because dust particles are relatively large. The net radiative forcing could be either negative or positive depending on the surface albedo, dust vertical distribution, and various optical properties of dust aerosols (Liao and Seinfeld, 1998). Dust generation responds to changes in weather and climate since wind speed and soil moisture are critical in controlling dust lifting. Likewise, it is possible that weather and climate may respond to dust amount. We use a microphysical-climate-radiation model to attempt to limit some of these uncertainties and gain a better understanding of the role of dust in the climate of China.

Several studies have previously considered the effects of dust on the radiation budget of China, and have identified the single scattering albedo (SSA) as especially critical to quantifying the radiation budget. Huang et al. (2009) used data from Cloud-Aerosol Lidar and Infrared Pathfinder Satellite Observations (CALIPSO) and Cloud and the Earth's Energy Budget Scanner (CERES) to constrain radiative transfer calculations and found the net radiative heating rate could reach 5.5 K day^{-1} at 5 km with a typical value of 1-3 K day^{-1} in dust layers over the Taklimakan desert in Asia. They also found that the net radiative forcing at the top of the atmosphere (TOA) was positive (warming) and that longwave radiation contributed two-thirds of the radiative forcing. About 90% of

the atmospheric warming was contributed by shortwave radiation. There were the similar radiative effects at the surface where longwave warming offset about one third of the shortwave cooling.

Huang et al.'s (2009) conclusion that TOA net forcing is positive depends on assuming a relatively low value of SSA of about 0.89 at a wavelength of 0.67 μm over the Taklimakan desert. Ge et al. (2011) used ground-based instruments to determine that the single scattering albedo was about 0.83, which is even lower than suggested by Huang etal. (2009). These SSA values are much lower than suggested in previous studies of desert dust around the world. Forster et al. (2007) suggested a global mean SSA of 0.96 for desert dust based on spectrally dependent, simultaneous remote and in situ observations. Dubovik et al. (2002) gave an average SSA of 0.95 at 0.67 μm based on long-term AERONET observations over the Saharan desert. Mikama et al. (2006) suggested a SSA value of 0.93 over the Asian desert during the Aeolian Dust Experiments on Climate (ADEC). Su and Toon (2011) used a small set of AERONET observations to suggest the SSA of the Saharan dust may be about 0.035 lower than Asian dust. The values in the study of Su and Toon (2011) at 0.67 μm were about 0.96 for Asian dust. However, the single scattering albedo is wavelength dependent and reaches much lower values below 0.5 μm. All these relatively high SSA will result in different shortwave radiative forcing compared with Huang et al. (2009) and Ge et al. (2011).

An alternative approach to determining the SSA instead of using optical observations, is to use wavelength dependent refractive indices measured for dust samples together with scattering theory to determine the SSA for different sized particles. Generally, climate models use this approach since the radiative properties are usually not available from observations for all possible circumstances. For example, the SSA is directly dependent on dust size distributions that vary in space and time. Dust

optical properties are very sensitive to small dust particles (0.1-1.0 um diameter) because of their larger scattering and absorbing cross sections per unit mass relative to large particles (Claquin et al., 1998; Seinfeld and Pandis, 1998). Su and Toon (2009, 2011) reproduced observed dust size distributions using the coupled climate-microphysical model, CAM3/CARMA2.3, with 16 dust size bins having central radius covering the range from 0.1 to 10 μm. Using refractive indices from AERONET observations, the computed wavelength dependent SSA were close to those derived by AERONET. Claquin et al. (1998) argued that using the refractive indices for a few wavelength or using wavelength averaged ones would bring large errors in calculating radiative fluxes so computing wavelength dependent values is important. The refractive indices depend on composition, which can vary between various regions (Sokolik and Toon, 1996; Claquin et al., 1998; Shi et al., 2005). Shi et al. (2005) provided an updated dataset of refractive indices for a wide spectral range (about 0.1 to 100 μm) representing East Asia dust based on the dust collected from the Taklimakan desert. Shi et al. (2005) used a simple single radiative-convective model to simulate dust radiative fluxes with specified dynamics and surface albedo. Their size distribution and refractive indices yield SSA near 0.94, which is on the high side of the range that is suggested by observations.

Here we explore the importance of the uncertainty in the SSA to the radiative effects of dust on the climate of China. We employ Mie theory and the refractive indices of Shi et al. (2005) as an initial case, but then scale the refractive indices to consider more absorbing aerosols as suggested in Ge et al. (2011). The integrated three-dimensional microphysical-climate-radiation model used in this study allows us to consider interactions with the local surface albedo and emissivity, evolution of the size

distribution in time, the vertical distribution of the dust as well as transport of dust aerosols vertically and horizontally.

4.2 Model description

The integrated three-dimensional microphysical-climate-radiation model based on the NCAR Community Atmosphere Model (CAM5) (Neale et al., 2010) and the University of Colorado/NASA Community Aerosol and Radiation Model for Atmospheres (CARMA3.0) (Toon et al., 1988; Jensen et al., 1994; Ackerman et al., 1995) is a new coupled numerical model. Su and Toon (2009, 2011) employed CARMA2.3, coupled with CAM3.0. The new version of CARMA, CARMA3.0, provides a computational interface currently being used for various microphysical models of polar stratospheric clouds, cirrus, dust, sulfate, sea salt, and black carbon. The microphysics and structure in CARMA3.0 is nearly identical to that in CARMA2.3, but the code has been updated to Fortran 90, and made compatible with the NCAR CAM5 model. CARMA3.0 is a bin-resolved column aerosol-microphysical sectional model. CARMA3.0 generates optical properties using Mie theory for aerosol optical properties such as extinction optical depth, single scattering albedo, and asymmetry factor. These optical properties are passed to the radiation scheme in CAM5.

CAM5 uses the Rapid Radiative Transfer Model for GCMs (RRTMG). RRTMG is used to calculate the radiative fluxes and heating rates for the radiatively active particles with an efficient and accurate modified correlated-k method both for the shortwave bands (14 bands between 0.2 μm to 12.2 μm) and longwave bands (16 bands from 3.1 μm to 1000 μm) (Iacono et al., 2008).

I use a horizontal resolution for CAM5/CARMA3.0 of 1.9^{o} x 2.5^{o} degrees, with 30 hybrid vertical model layers from the surface to about 40 km. We use 16 dust size bins

with central radius covering the range from 0.1 to 10 μm to parameterize the modified Ginoux et al. (2001) dust source function as discussed in Su and Toon (2009 and 2011). The coupled CAM5-CARMA3.0 is driven by offline meteorological fields from NCAR and the National Center for Environmental Prediction (NCEP) reanalysis package (Rasch et al., 1997).

As stated in Huang et al. (2009), most Asian dust studies have focused on spring. However, the CALIPSO lidar observations show that dust plumes occur throughout the year over Taklimakan desert (Liu et al., 2008a) and it showed heavy dust storm weather during summer (Huang et al., 2007) due to low precipitation (Laurent et al., 2006). In this study, we chose to consider the effects of dust on China in July 2006 to be consistent with the time period of the studies in Huang et al. (2009).

4.3 Results

4.3.1 Optical properties of dust aerosols over East Asia

I simulated the dust optical properties, such as dust optical depth and single scattering albedo (SSA) using the coupled CAM5/CARMA3.0 model based on the approach described in Su and Toon (2009). We define the real part of the complex refractive index of dust particles as 1.55, which is wavelength independent and consistent with previous studies (Patterson at al., 1977; Diaz et al., 2000; Liu et al., 2002; Su and Toon, 2009&2011). The imaginary parts of the complex refractive indices are constrained by the two cases mentioned above (case-Shi and case-Ge) based on radiative closure experiments.

Shi et al. (2005) developed a set of data representing East Asian dust aerosols based on a field campaign in spring 2002 during the Sino-Japan joint project titled “Aeolian Dust and it’s Experiment on Climate Impact (ADEC)” period. The dust samples were collected in Cele ($37^{o}01^{'}$N, $80^{o}44^{'}$E, 1363 m above sea) and the surrounding area,

which is south of Taklimakan desert in western China. Shi et al. (2005) calculated downward diffuse flux using a refractive index model based on the weighted volumes of the main compositions of mineral dust particles collected in Cele. They also observed the spectral diffuse fraction in downward radiative flux using a spectrometer (Field Spec FR of ASD Inc., spectral region covers 350 to 2500 nm). Then they compared the theoretically calculated refractive indices using the refractive index model with the measured ones using the spectrometer and obtained the ones that best fit the observed diffuse fractions. For case-Shi I used the imaginary part of the refractive index as indicated in Shi et al. (2005) from ADEC (0.004670, 0.002430, 0.002330, 0.002360 for wavelengths at 0.441 μm, 0.673 μm, 0.873 μm, and 1.022 μm, respectively). I use Shi et al. (2005) imaginary refractive indices for all other wavelengths in the infrared. It should be noted that the longwave scattering effects are not presently included in RRTMG in CAM5.0.

On the other hand, Ge et al. (2011) concluded that the imaginary part of the dust complex refractive index is 0.01 at 0.67μm based on radiative closure experiments in two field experiments, the U.S. Department of Energy Atmospheric Radiation Measurement (DOE/ARM) Program in 2008 and the Semi-Arid Climate and Environment Observation of Lanzhou University (SACOL) Program in 2010, during April to June over Northwest China. They measured the broadband total irradiance and the diffuse flux using a Pyranometer at the south edge of Gobi desert, and the optical properties of dust aerosols were derived from the Multi-Filter Rotating Shadowband Radiometer (MFRSR). We used the imaginary parts of refractive indices as (0.0192, 0.010, 0.00957, 0.00970) for wavelengths at 0.441 μm, 0.673 μm, 0.873 μm, and 1.022 μm, respectively in our model for case-Ge. At other wavelengths I used the same refractive indices as in case-Shi.

Figure 4.1(a) shows the simulated column integrated mean optical depth in July 2006 over East Asia at a wavelength of 0.67 μm. The optical depth is greater than 1 (the maximum is 1.6) near dust sources (Taklimakan desert and Gobi desert), and decreases as dust is transported downward (around 0.3 in Beijing area). The difference between case-Shi and case-Ge is less than 1%, which is consistent with the results in Ge et al. (2011) who compared their MFRSR cases with AERONET cases for dust optical properties for the two field experiments mentioned above.

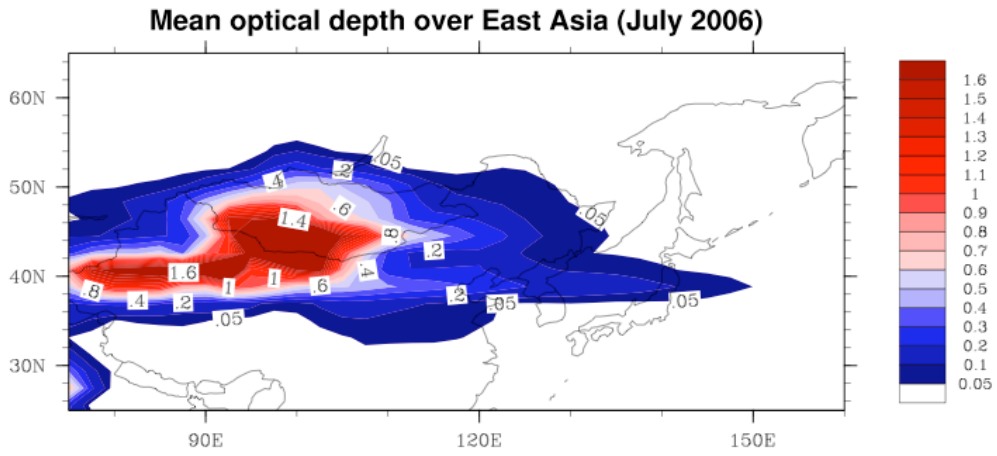

Figure 4.1(a) Column integrated mean optical depth in July 2006 over East Asia at λ = 0.67 μm (the difference between case-Shi and case-Ge less than 1%).

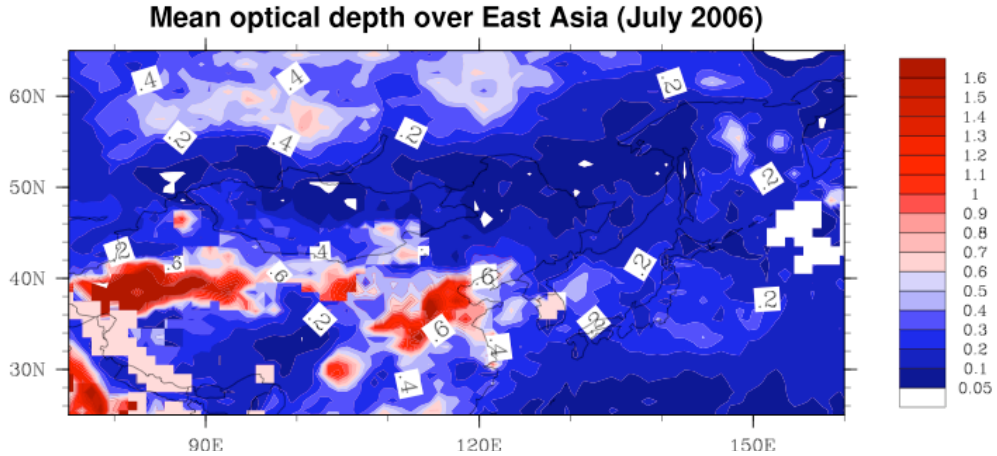

Figure 4.1(b) Monthly mean optical depth in July 2006 over East Asia from MODIS.

Figure 4.1 (b) shows the monthly mean aerosol optical depth from MODIS in July 2006. The maximum value (1.2) is comparable to the one (1.6) in Figure 4.1 (a) from model simulations. The AOD value in Beijing from MODIS data in Figure 4.1(b) is higher (0.6) compared with the model simulations (0.3). This larger value is possibly due to other pollution being mixed with dust over the Beijing.

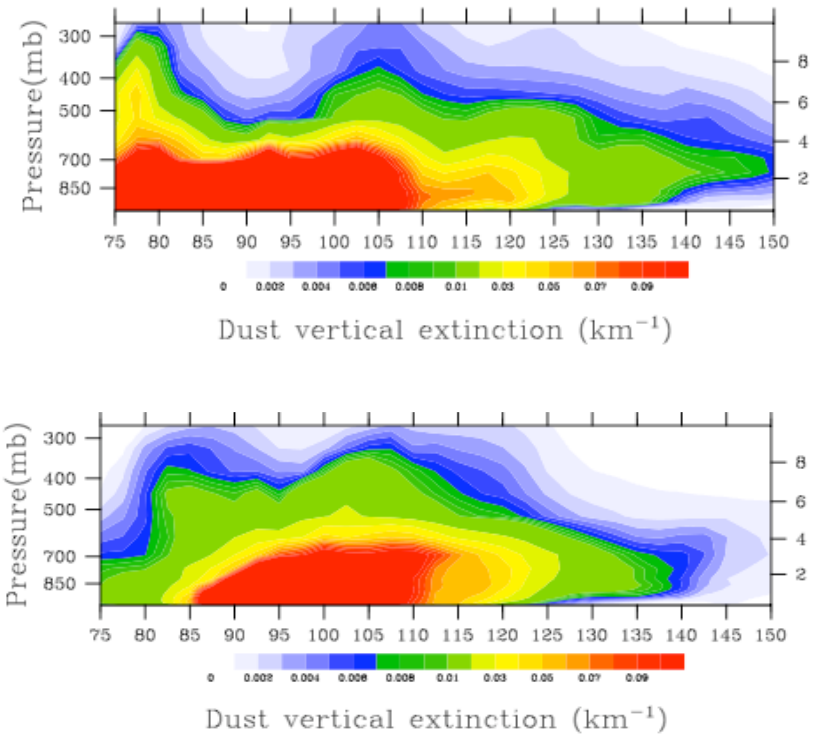

Figure 4.1 (c) The simulated vertical dust extinction (km^{-1}) along 40°N latitude (top) (crossing the Taklimakan desert) and the one along 47°N latitude (bottom) (crossing the Gobi desert).

Figur 4.1 (c) shows the simulated vertical dust extinction (km^{-1}) along 40°N latitude (top) (crossing the Taklimakan desert) and along 47°N latitude (bottom) (crossing the Gobi desert). It clearly shows that the maximum dust vertical extinction for the two deserts can be up to 0.1 km^{-1}.

The SSA is the most important variable for aerosol direct radiative forcing calculations. The magnitude of SSA is dependent on the dust size distribution, and the refractive index. We used the same dust source function and dust model for both case-Shi and case-Ge, which means we use essentially the same dust size distribution for both cases. The major difference that affects the SSA values will be the refractive index for the two cases as defined above. Figure 4.2 (a) presents the simulated column integrated mean SSA for case-Shi (top) and case-Ge(bottom) in July 2006 over East Asia at a wavelength of 0.67 μm based on the two sets of refractive indices. The SSA values are around 0.94 near the dust sources from case-Shi, whereas it's about 0.82 for case-Ge. The SSA values increased during transport away from the source reaching 0.96 for case-Shi and 0.84 for case-Ge in Japan. This increase in SSA is caused by the decreasing size of the particles as they move away from the source, since smaller particles have higher SSA for particles in this size range (Figure 4.2(b)). Figure 4.2 (b) shows the simulated monthly mean effective radius in July 2006. The effective radius decreased from 2.8 μm near the dust sources to 2.2 μm near Japan.

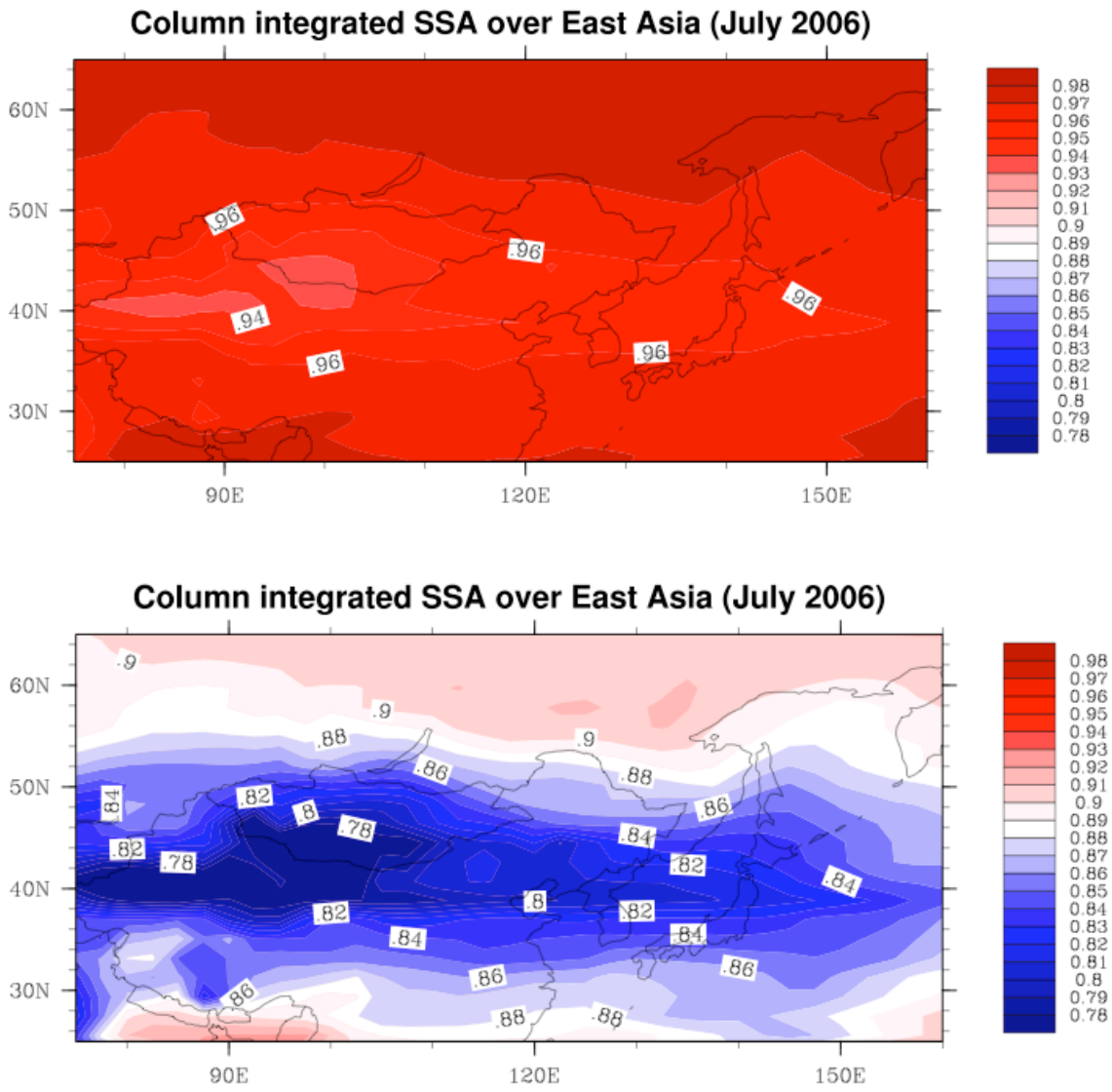

Figure 4.2 (a) Column integrated mean single scattering albedo for case-Shi (to
and case-Ge (bottom) in July 2006 over East Asia at λ = 0.67 μm.

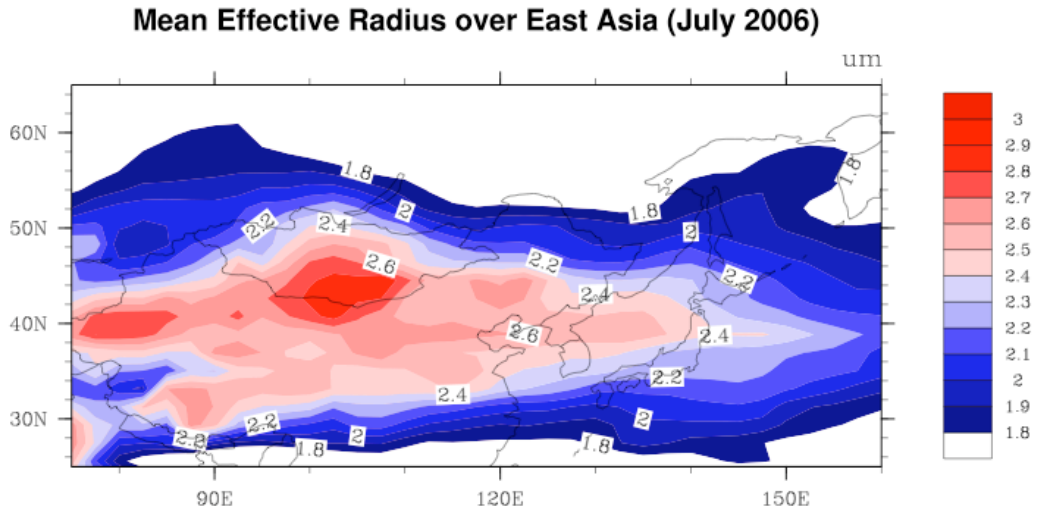

Figure 4.2 (b) Column monthly mean effective radius over East Asia in July 2006.

4.3.2 Radiative fluxes of dust aerosols

Figure 4.3 shows the simulated monthly mean clear-sky net radiative fluxes at TOA from CERES (top), case-Shi (middle), and case-Ge (bottom) in July 2006 over East Asia. Both the patterns and the magnitudes of the net radiative fluxes (130 to 156 W m^{-2}) are comparable between CERES and the two cases although the two cases overestimate the fluxes up to 10 W m^{-2}. Figure 4.4 shows the differences in net radiative flux at TOA between case-Ge and case-Shi (case-Ge minus case-Shi) in July 2006. The dust net radiative flux at TOA is larger in case-Ge than case-Shi, by up to 6 W m^{-2} near dust sources, and decreasing during dust transport away from the sourcecs The larger imaginary part of refractive index in case-Ge results in smaller SSA compared with case-Shi. Therefore the dust aerosols from case-Ge may absorb more solar energy so less is reflected at TOA and the shortwave net flux is larger than in case-Shi.

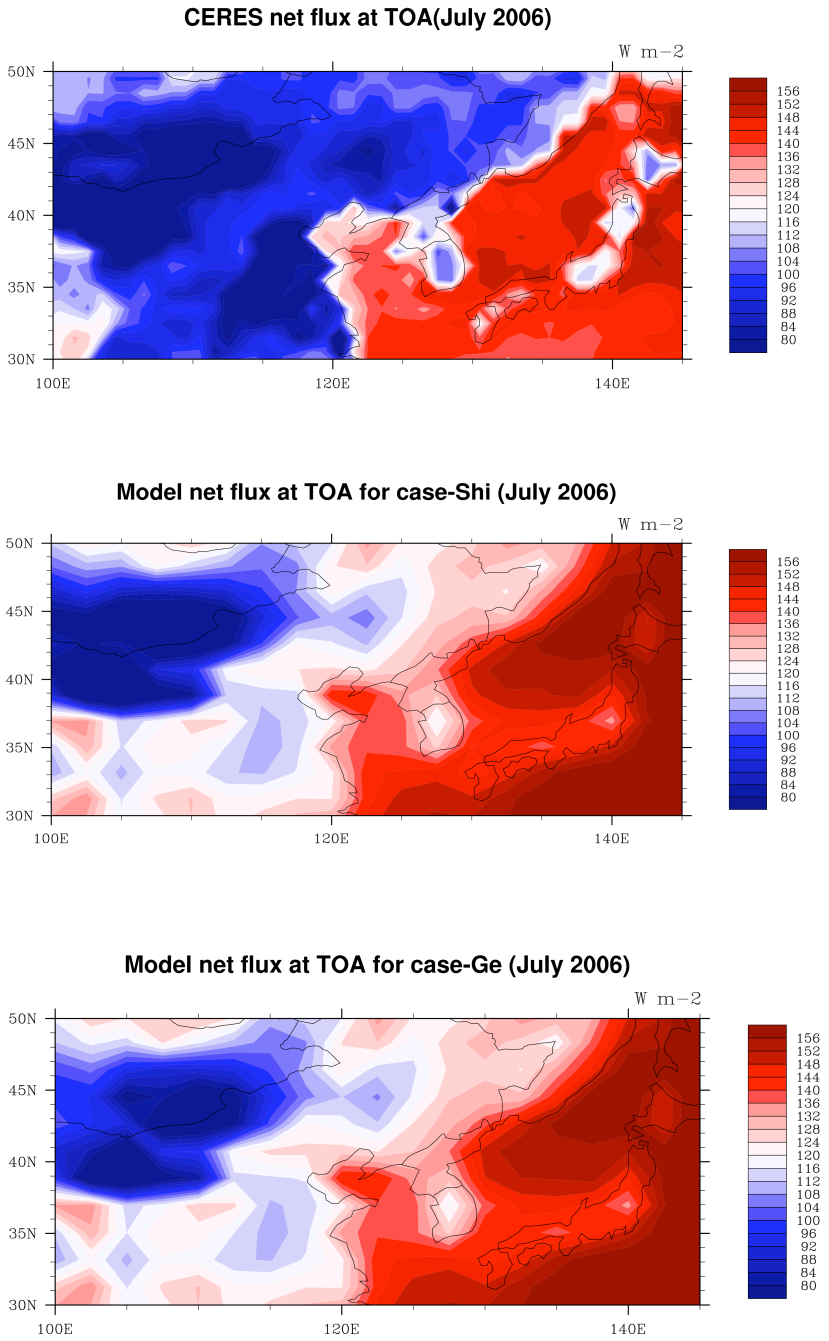

Figure 4.3 Monthly mean clear-sky radiative fluxes at TOA from CERES (top), case-Shi (middle), and case-Ge (bottom) in July 2006.

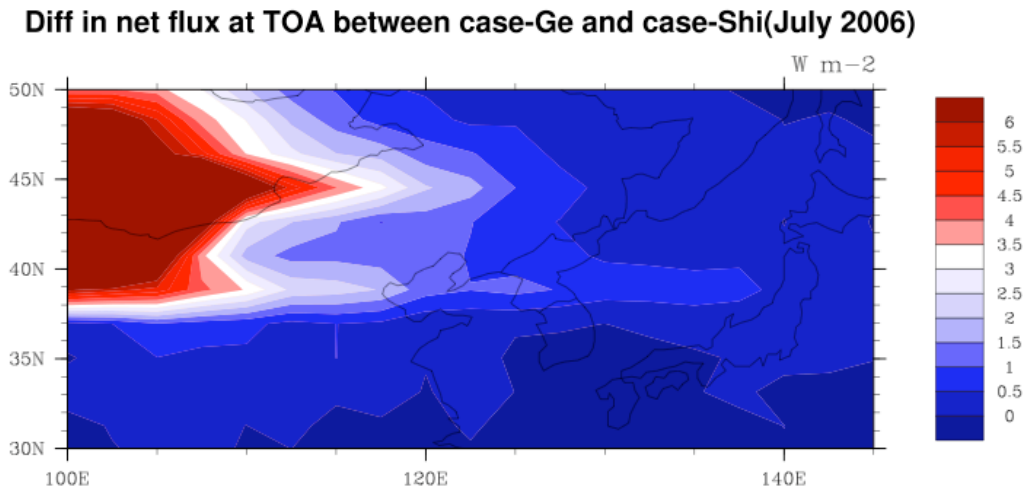

Figure 4.4. Monthly mean differences between case-Ge and case-Shi for the net flux at TOA in July 2006.

Figure 4.5 presents the change in the simulated monthly mean shortwave radiative fluxes at TOA due to dust radiative forcing (with dust minus without dust radiative forcing) from case-Shi (top) and case-Ge (bottom) in July 2006. The shortwave fluxes at TOA due to dust radiative forcing in case-Shi is negative (between 0 to -3.5 W/m^2) with the maximum smaller than -3.5 W/m^2 near dust sources, whereas the values are positive in case-Ge (between 0 to 2.5 W/m^2) with the maximum larger than 2.5 W/m^2 near dust sources. Figure 4.6 shows the simulated monthly mean net radiative fluxes at TOA due to dust radiative forcing from case-Shi (top) and case-Ge (bottom) in July 2006. We come up with the similar patterns and the magnitudes comparing with Figure 4.5. We conclude that the radiative forcing at TOA is very sensitive to the SSA values, and the shortwave radiative forcing is the greatest difference between the Shi and Ge cases. Dust is likely to have only modest effects on the longwave forcing, as suggested by previous studies. Hansen et al. (1981) suggested that aerosol particles with SSA

higher than 0.85 may result in negative TOA forcing and the ones smaller than 0.85 may yield positive TOA forcing, which is consistent with Figure 4.6.

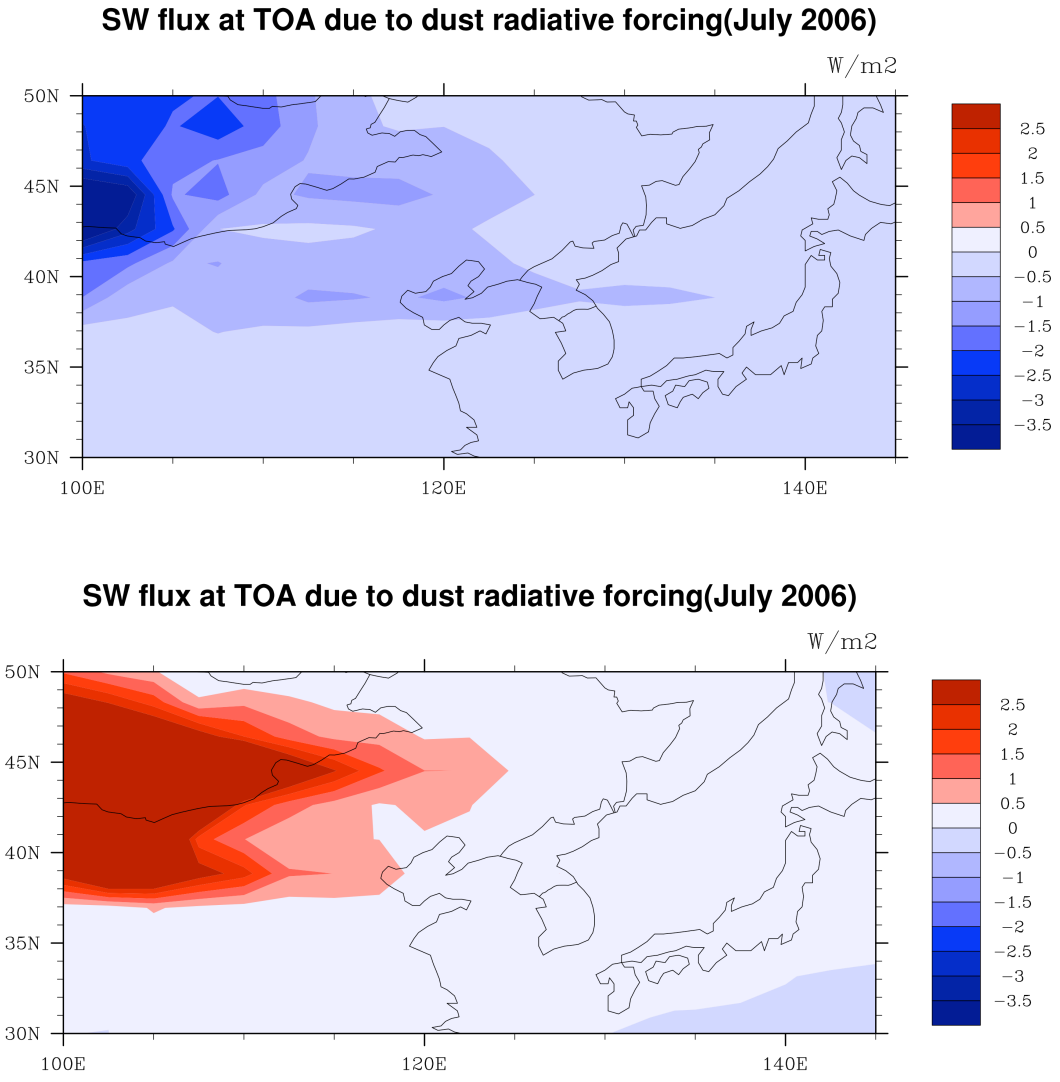

Figure 4.5 Change in monthly mean shortwave fluxes at TOA due to dust radiative forcing from case-Shi (top) and case-Ge (bottom) in July 2006.

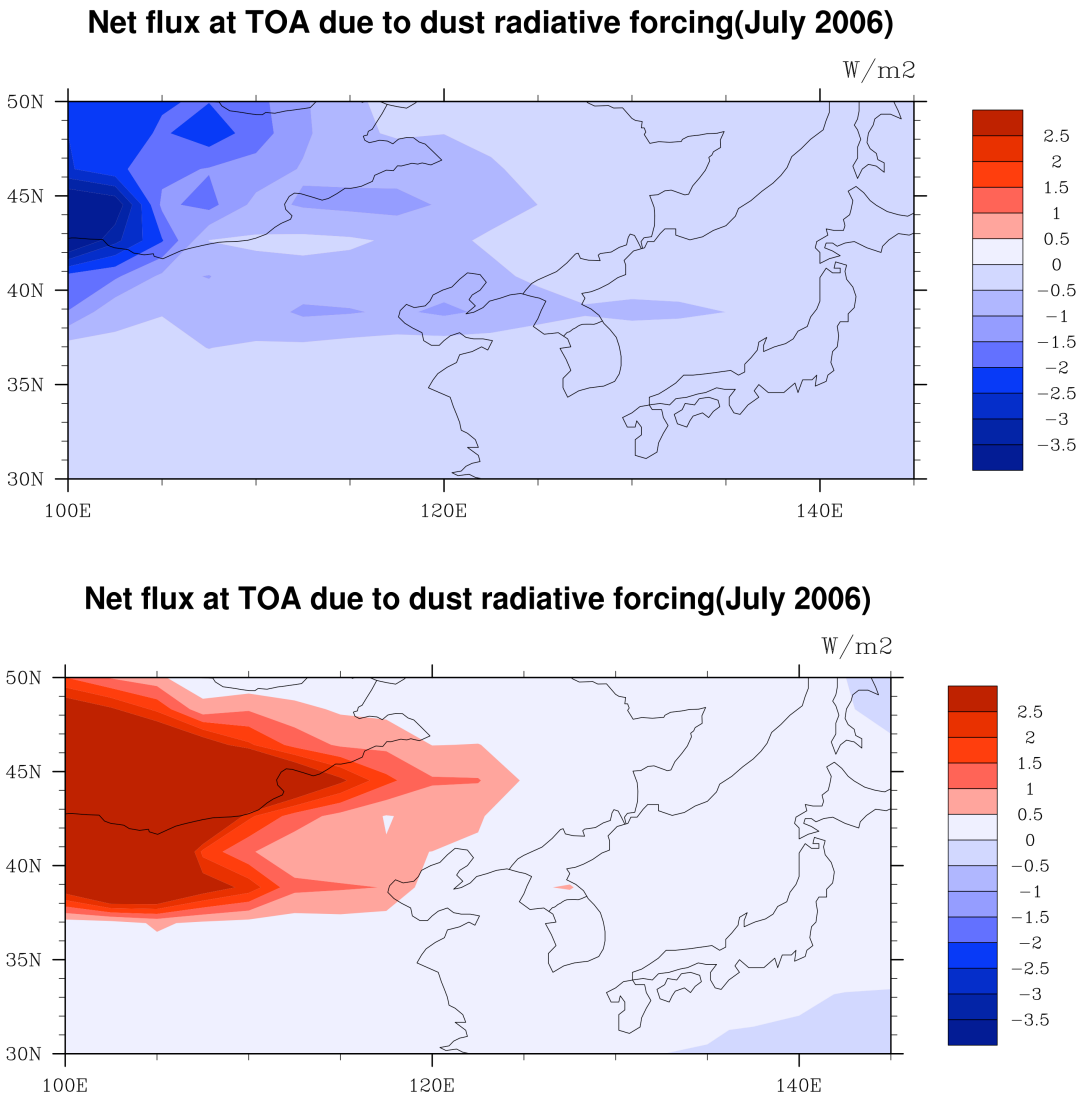

Figure 4.6 Monthly mean net fluxes at TOA due to dust radiative forcing from case-Shi (top) and case-Ge (bottom) in July 2006.

Figure 4.7 shows the simulated monthly mean change in net radiative fluxes at surface from case-Shi (top) and case-Ge (bottom) in July 2006. The change in the net fluxes at surface are both negative. As we defined the downward fluxes as positive, the positive radiative TOA flux (downward) and larger negative surface flux (upward) from case-Ge indicates larger dust direct radiative forcing in the atmosphere compared with the one from case-Shi, so there are greater warming effects to the atmosphere from case-Ge.

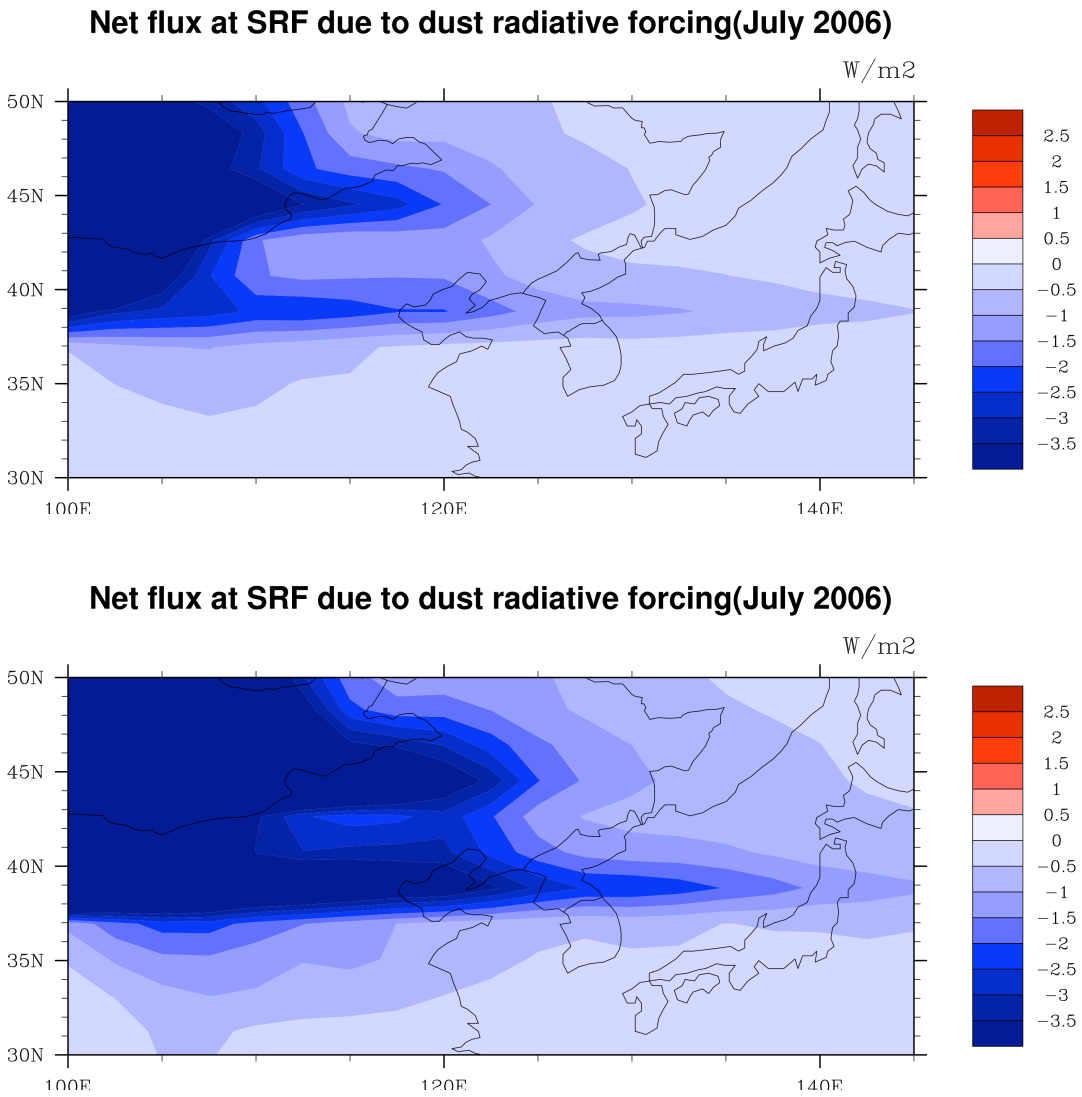

Figure 4.7 Change in monthly mean net fluxes at surface due to dust radiative forcing from case-Shi (top) and case-Ge (bottom) in July 2006.

4.3.3 Dust heating rates

Figure 4.8 shows the simulated daily mean shortwave (top), longwave (middle), and net (bottom) heating rates due to dust aerosols, respectively, for case-Shi (left panel) and case-Ge (right panel) over Taklimakan Desert (averaged between 37^{o}N-40^{o}N and 78^{o}E-88^{o}E) in July 2006. Note the difference in the scales between the longwave and shortwave heating. The shortwave radiation dominates the dust radiative effects and heats the atmosphere by absorbing shortwave solar energy. There is about 3 times larger heating in case-Ge compared with case-Shi for the shortwave heating rates in July 2006. The heating rates of shortwave radiation for case-Ge was up to 6 K day^{-1} on July 12 to 16 and July 28, 2006 in heavy dust layers, and around 3 K day^{-1} on other days in July 2006 over the Taklimakan desert. For case-Shi, the maximum of the shortwave heating rates are about 2 K day^{-1} on July 12 to 16, 2006, and they are 1 K day^{-1} on other days in July 2006.

The longwave radiative heating rates show (Figure 4.8 (middle)) warming effects in and below dust layers and cooling effects on the top of dust layers both for case-Shi and case-Ge with maximum heating near the surface. There is more dust heating in case-Ge than case-Shi and it is up to 0.5 K day^{-1} on July 14 2006 for case-Ge, whereas it is around 0.1 K day^{-1} for case-Shi. The longwave cooling rates on the top of the dust layers are around -0.2 K day^{-1} for both two cases. This longwave cooling is smaller than the dust heating rates in the same layers.

The net dust heating rates (Figure 4.8 (bottom)) are positive through out the dust layers in the atmosphere both for case-Shi and case-Ge in July 2006. The maximum

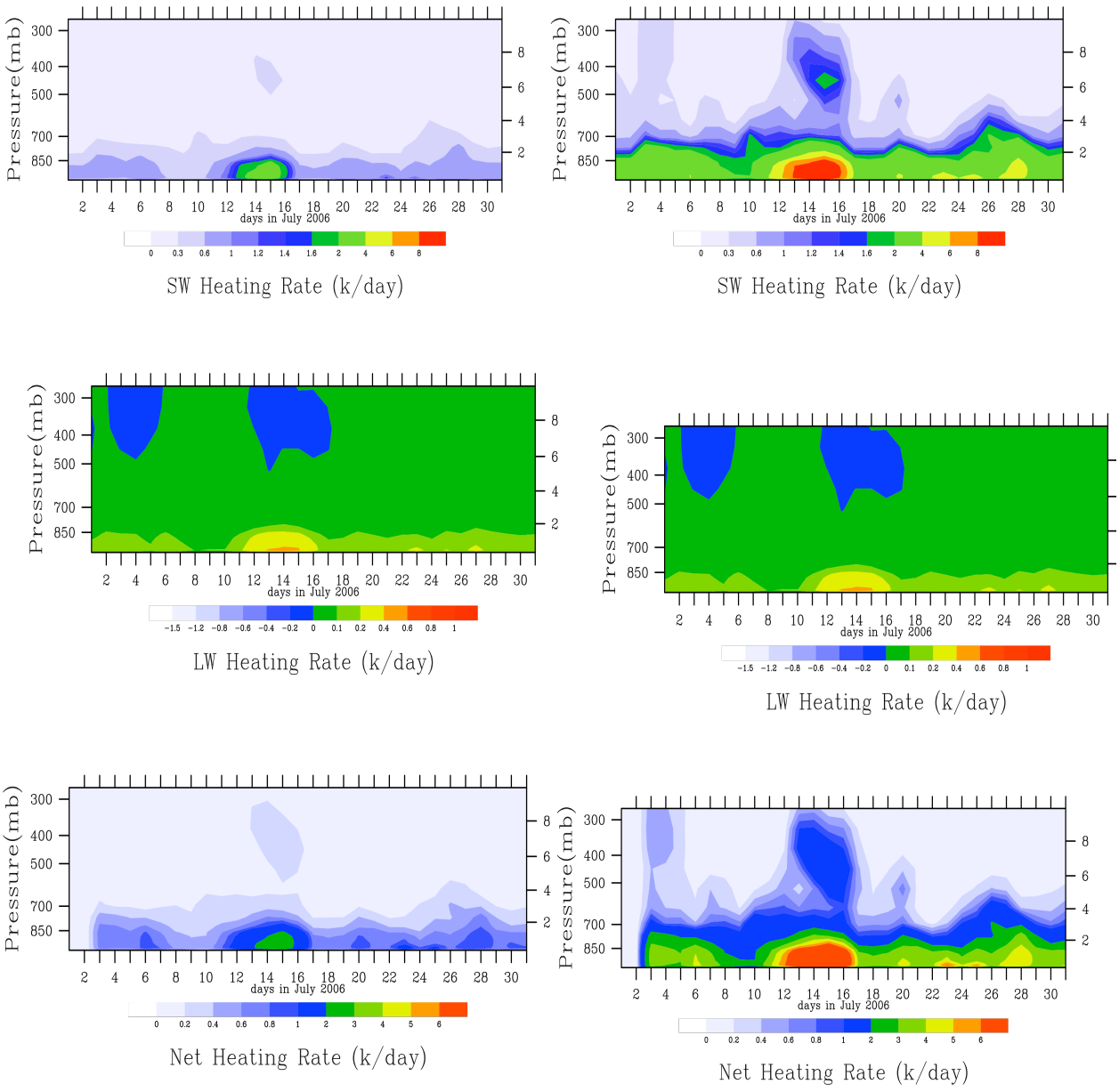

Figure 4.8 Daily mean heating rates for shortwave (top), longwave (middle), and net (bottom) for case-Shi (left panel) and case-Ge (right panel) over Taklimakan Desert in July 2006.

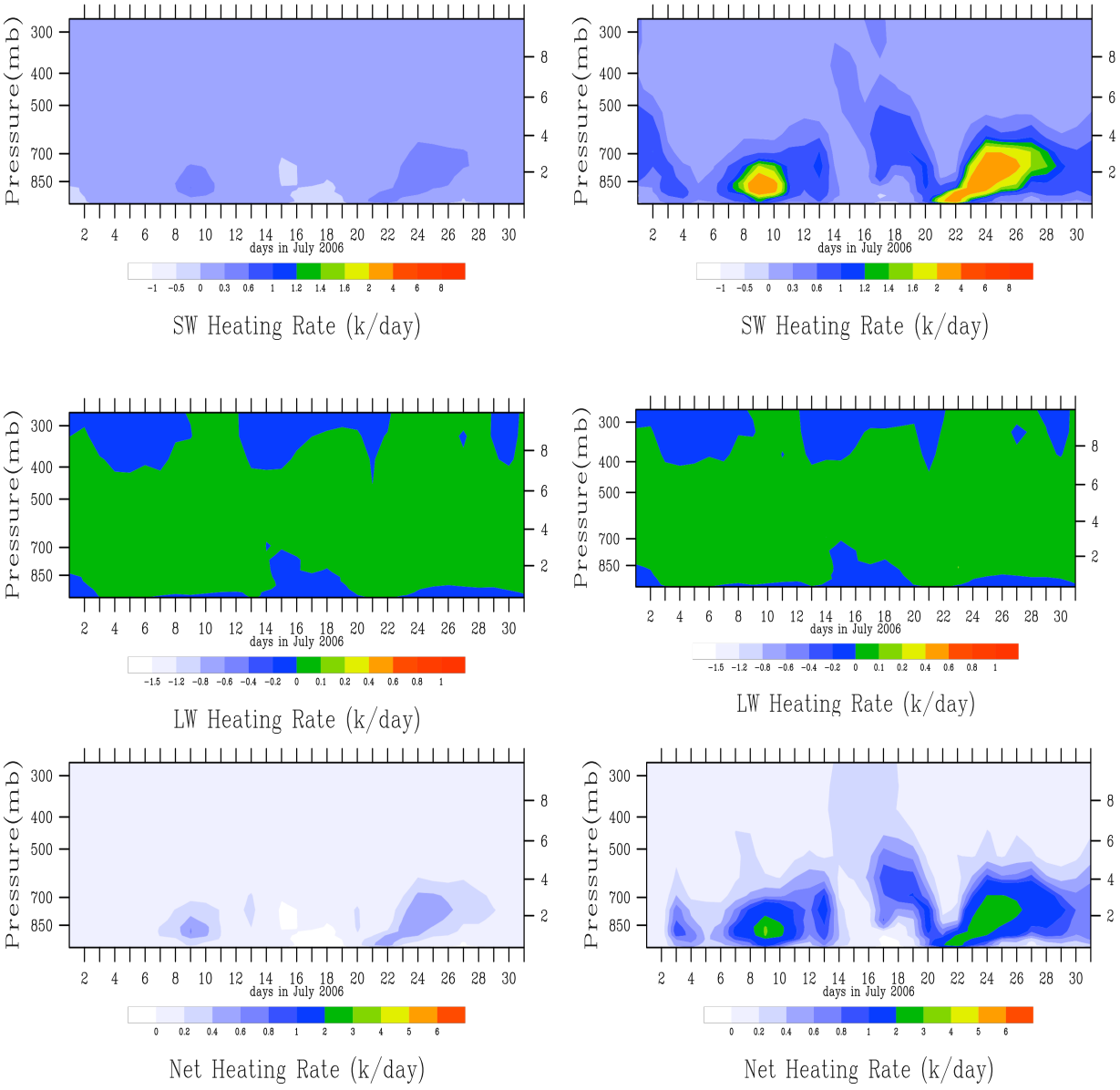

Figure 4.9 Daily mean heating rates for shortwave (top), longwave (middle), and net (bottom) for case-Shi (left panel) and case-Ge (right panel) over Beijing in July 2006.

heating rates can up to 6 K day^{-1} in case-Ge on July 12 to 16 2006, whereas it is 2 K day^{-1} for the same time period in case-Shi.

Figure 4.9 shows the simulated daily mean shortwave (top), longwave (middle), and net (bottom) heating rates due to dust aerosols, respectively, for case-Shi (left panel) and case-Ge (right panel) over the Beijing area (averaged around 40^{o}N and 116^{o}E) in July 2006. The shortwave radiation still dominates the dust radiative effects and heats the atmosphere by absorbing shortwave solar energy. There is about 3 times larger heating for case-Ge compared with case-Shi for the shortwave heating rates in July 2006. The heating rates of shortwave radiation for case-Ge can be up to 2 K day^{-1} on July 9 and July 23, 2006 in relatively heavy dust layers, and around 0 to 1 K day^{-1} on other days in July 2006 over Beijing area. For case-Shi, the maximum of the shortwave heating rates is about 0.6 K day^{-1} on July 12 to 16, 2006, and they are -1 to 0.3 K day^{-1} on other days in July 2006. Negative shortwave heating can result from the loss of light due to absorption by dust above the level of interest.

The longwave radiative heating rates show (Figure 4.9 (middle)) warming effects in dust layers and cooling effects below and on the top of dust layers both for case-Shi and case-Ge. There is similar dust warming effects between case-Ge and case-Shi of up to 0.1 K day^{-1} in July 2006. The longwave cooling rates on the bottom and the top of the dust layers are around -0.2 K day^{-1} for both two cases.

The net dust heating rates (Figure 4.9 (bottom)) are positive through out the dust layers in the atmosphere both for case-Shi and case-Ge in July 2006. The maximum heating rates can up to 2 K day^{-1} in case-Ge on July 9 and July 23 2006, whereas it is 0.6 K day^{-1} for the same time period in case-Shi.

Figure 4.10 shows the simulated daily mean shortwave (top), longwave (middle), and net (bottom) heating rates due to dust aerosols, respectively, for case-Shi (left

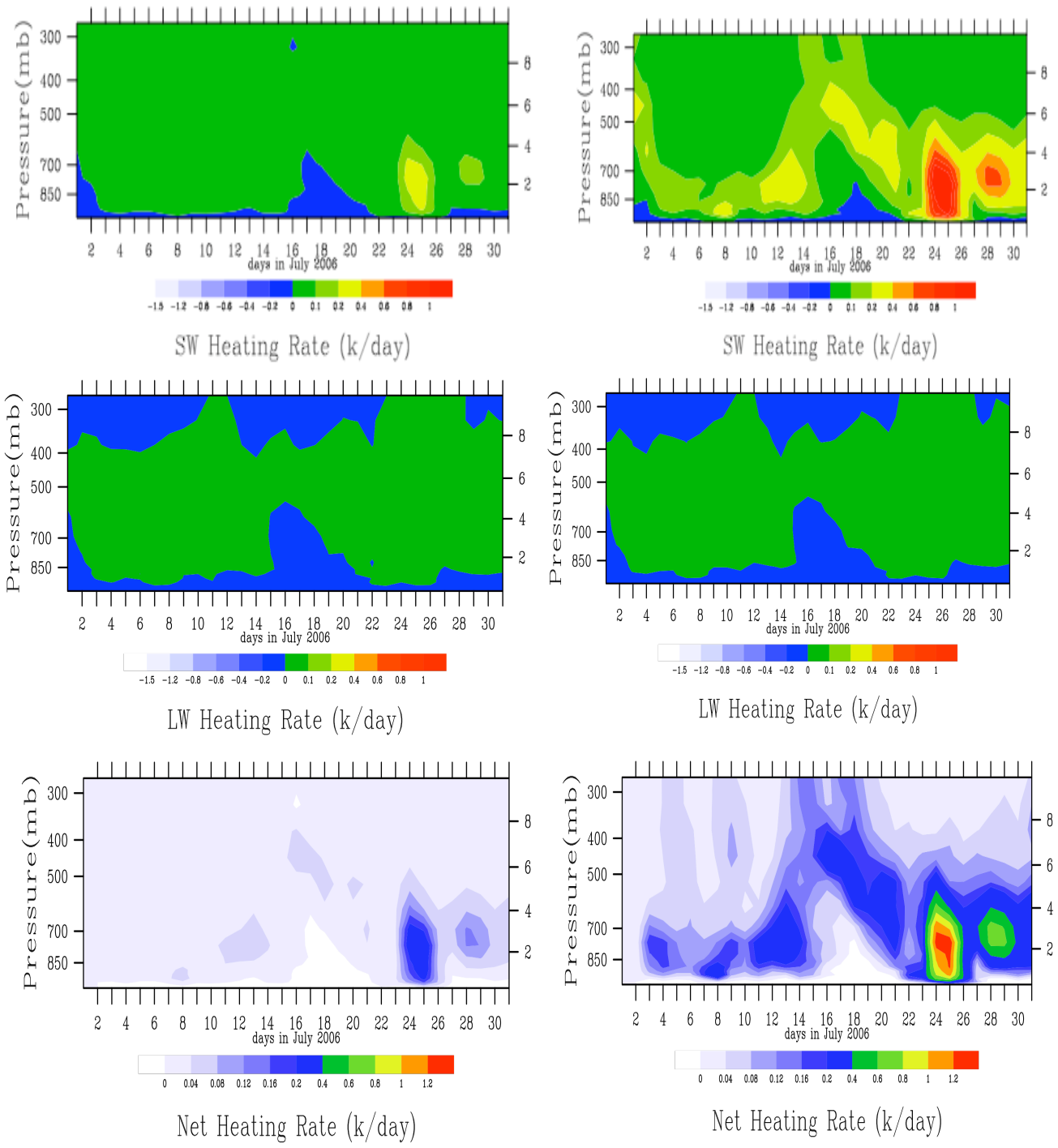

Figure 4.10 Daily mean heating rates for shortwave (top), longwave (middle), and net (bottom) for case-Shi (left panel) and case-Ge (right panel) over Sea of Japan in July 2006.

panel) and case-Ge (right panel) over the Sea of Japan in July 2006. The shortwave radiation has similar magnitudes as the longwave radiation over the Sea of Japan. The heating rates due to shortwave radiation for case-Ge is up to 1.2 K day^{-1} on July 24, 2006. There are negative heating rates for both cases (such as on July 18 2006) near the surface over the Sea of Japan. This small cooling could be caused by the small ocean surface albedo that reflects little solar radiation so it has less chance to be absorbed by dust aerosols. The longwave radiative heating rates show (Figure 4.10 (bottom)) more cooling near the surface compared with Taklimakan and Beijing cases both for case-Shi and case-Ge. The differences can be explained by the different surfaces for these locations. The Taklimakan desert has a brighter and hotter surface that emits more longwave radiation that can interact efficiently with large particles near the dust sources, whereas the dark and cold ocean emits less longwave radiation that has less chance to interacted with dust aerosols over the Sea of Japan. The net dust heating rates (Figure 4.10 (bottom)) are generally positive.

4.3.4 Surface temperatures

The model runs done to date are not sufficient to show changes in surface temperatures, because the model is constantly nudged back to observations. In the future I plan to conduct free running simulations to better understand the different impacts on climate of the two choices of refractive index.

Figure 4.11 shows simulated monthly mean surface temperatures differences between case-Ge and case-Shi (case-Ge minus case-Shi) in July 2006. Despite being nudged back to data, there are larger negative dust net radiative fluxes at surface in case-Ge compared with case-Shi near dust sources (Figure 4.7), which results in lower surface temperature (negative) in case-Ge than in case-Shi (Figure 4.11). This means

there is more dust radiative effects on surface temperature if we use a larger imaginary part of the dust refractive index (such as 0.01 at 0.67 um) or a smaller SSA (0.82) in case-Ge compared with case-Shi (around 0.002 for refractive index at 0.67um) and 0.94 for SSA).

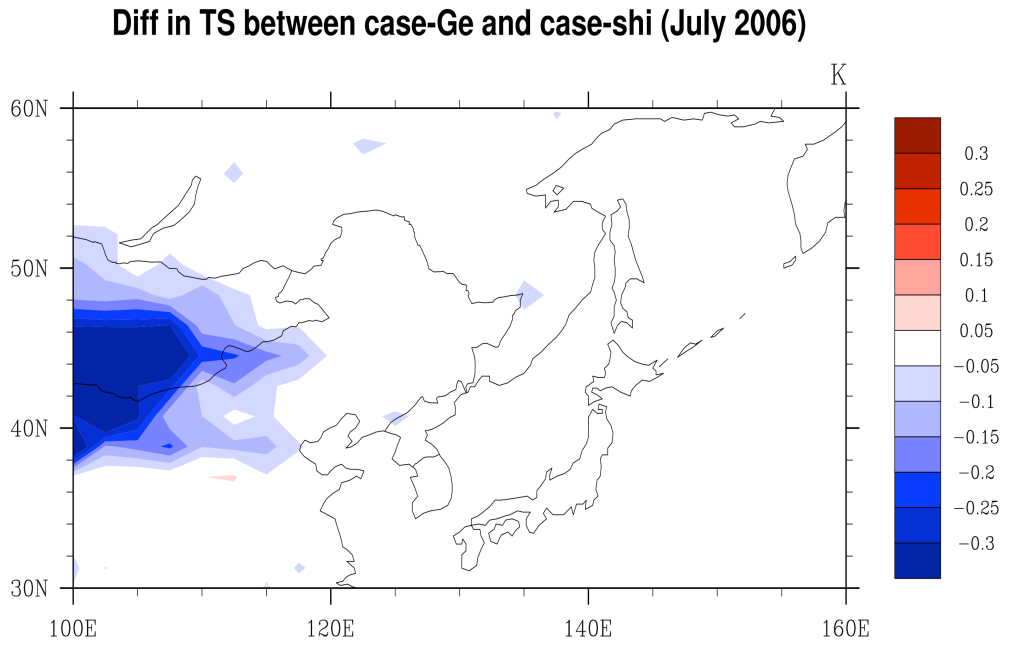

Figure 4.11 Monthly mean surface temperatures at surface due to dust radiative forcing from case-Shi (top), case-Ge (middle), and differences between case-Ge and case-Shi in July 2006.

4.4 Conclusions

The importance of the uncertainty in the SSA to the radiative effects of dust on the climate of China are explored through two case studies based on the modeled and observed solar diffuse fluxes/irradiances at the surface. The integrated three-dimensional microphysical-climate-radiation model used in this study allows us to consider interactions with the local surface albedo and emissivity, evolution of the size distribution in time, the vertical distribution of the dust as well as transport of dust aerosols vertically and horizontally.

The SSA values are around 0.94 near the dust sources from case-Shi, whereas they are about 0.82 for case-Ge. The SSA values increased during transport away from the source reaching 0.96 for case-Shi and 0.84 for case-Ge in Japan. This increase in SSA is caused by the decreasing size of the particles as they move away from the source, since smaller particles have higher SSA for particles in this size range.

The change in net radiative flux due to dust at TOA is larger in case-Ge than case-Shi, by up to 6 W m^{-2} near dust sources, and decreasing during dust transport away from the sources The larger imaginary part of refractive index in case-Ge results in smaller SSA compared with case-Shi. Therefore the dust aerosols from case-Ge absorb more solar energy so less is reflected at TOA and the shortwave net flux is larger than in case-Shi. The radiative forcing at TOA is very sensitive to the SSA values, and the shortwave radiative forcing is the greatest difference between the Shi and Ge cases. The change in the net fluxes at surface due to dust are both negative. As I defined the downward fluxes as positive, the positive radiative TOA flux (downward) and larger negative surface flux (upward) from case-Ge indicates larger dust direct radiative forcing

in the atmosphere compared with the one from case-Shi, so there is greater warming of the atmosphere from case-Ge.

There is about 3 times larger heating in case-Ge compared with case-Shi for the shortwave heating rates in July 2006. The heating rates due to shortwave radiation for case-Ge was up to 6 K day^{-1} on July 12 to 16 and July 28, 2006 in heavy dust layers, and around 3 K day^{-1} on other days in July 2006 over the Taklimakan desert. For case-Shi, the maximum of the shortwave heating rates are about 2 K day^{-1} on July 12 to 16, 2006, and they are 1 K day^{-1} on other days in July 2006.

The longwave radiative heating rates show warming effects in and below dust layers and cooling effects on the top of dust layers both for case-Shi and case-Ge with maximum heating near the surface. There is more dust heating in case-Ge than case-Shi and it is up to 0.5 K day^{-1} on July 14 2006 for case-Ge, whereas it is around 0.1 K day^{-1} for case-Shi. The longwave cooling rates on the top of the dust layers are around -0.2 K day^{-1} for both two cases. This longwave cooling is smaller than the dust heating rates in the same layers. The longwave radiative heating rates show more cooling near the surface compared with Taklimakan and Beijing cases both for case-Shi and case-Ge. The differences can be explained by the different surfaces for these locations. The Taklimakan desert has a brighter and hotter surface that emits more longwave radiation that can interact efficiently with large particles near the dust sources, whereas the dark and cold ocean emits less longwave radiation that has less chance to interact with dust aerosols over the Sea of Japan. The net dust heating rates are generally positive.

There are larger negative dust net radiative fluxes at surface in case-Ge compared with case-Shi near dust sources, which results in lower surface temperature (negative) in case-Ge than in case-Shi. This means there is more dust radiative effects on surface temperature if we use a larger imaginary part of the dust refractive index (such as 0.01 at 0.67 um) or a smaller SSA (0.82) in case-Ge compared with case-Shi

(around 0.002 for refractive index at 0.67um) and 0.94 for SSA). However, since my model temperatures are forced to data the model cannot fully represent the surface temperature differences due to the different SSA in these cases.

Chapter 5

Summary

In this study, we developed a three-dimensional coupled microphysical/climate model based on the NCAR CAM3 and CARMA2.3 models. Our goal was to test the model's ability to reproduce the optical properties of dust from Asia, as it is transported across the Pacific Basin. The model simulations were conducted during the time frame of the ACE-Asia field experiment since considerable data are available for that time. Our dust source function follows Ginoux et al. [2001]. We modified the source function by using the friction velocity instead of the 10-meter wind based on the wind erosion theory. The new threshold friction velocity formulation included both the inter-particle cohesion forces and the surface wetness factor based on the volumetric soil water for each particle size bin, which is important to the threshold wind speed of dust particles.

The Weibull wind distribution was implemented in the model, using an incomplete gamma function, to treat the sub-grid scale velocity distribution since at the coarse resolutions of typical global models the "mean" wind speeds at each grid cell do not represent the lifting process well. The timing and magnitude of most dust events have been captured when a Weibull wind distribution, surface stress or 10 m wind is used in the model. We tuned the dust lifting to reproduce a total dust emission around 210 Tg in spring of 2001 (March to May). Our conclusions differ from Liu and Westphal [2001] who found the 10 m winds did not capture all of the dust events in their study. Despite not finding this sensitivity in our work we believe it is important to include all of the physics related to the surface wind stress, and wind gusts since the physics may be important in cases other than the ones we examined.

The modeled AOT is well correlated with the AERONET retrievals ($R = 0.844$) in the six study sites, and the results are not greatly biased relative to the observations since the slope of their relationship is close to 1. The modeled single scattering albedo is

within the error bars of AERONET retrievals near the dust sources. SSA increased with increasing wavelength in both the model and observations. Comparing the modeled SSA over the Asian dust source region (Dunhuang) to studies elsewhere, I find that the observed single scattering albedo of dust has geographic variations. This variation could be caused by different dust compositions and/or background pollution not included in our model.

The vertical profiles of dust are comparable to the ACE-Asia 2001 NIES-lidar observations in Beijing and Nagasaki. Generally, the model produced almost all the dust events in April 2001, such as the dust storms that occurred on April 2, April 4, April 7-8 (the severe one), April 18, and April 28 in Beijing, and the dust events near the surface on April 12,13, and 14 and the dust in the free troposphere on 2, 23, 26 and 27 April of 2001. However, the model did not predict the dust events near the surface on the 26 and 27 of April at Nagasaki because wet deposition washed out the shallow level dust on 26 of April, which indicates that further work is needed on the model wet deposition process between dust source and downwind regions, such as Nagasaki, Japan.

I have shown here that the model results are consistent with data taken during ACE-Asia. There is also a wealth of satellite data with which the model can be compared. The Cloud Aerosol Lidar and Infrared Pathfinder Satellite Observations (CALIPSO) satellite lidar retrievals will provide new insight into the broad scale dust vertical distribution. However CALIPSO was not operating during the time frame of ACE-Asia. Hence, we present a comparison of model simulations with satellite data in chapter 3 using a different simulation time frame.

Using my model we find that the yearly annual dust flux from Africa is about 3 times greater than that from Asia. In general, it is observed that the dust optical depth is higher over the Atlantic than over the Pacific at similar downwind distances from the two dust sources. The monthly-averaged optical depth is 0.382 and 0.339 over the Pacific at

Osaka in May 2007 for AERONET data and model simulation, respectively. However, the monthly-averaged optical depth is 0.613 and 0.579 over Atlantic at Capo Verde in July 2007 for AERONET data and model simulation, respectively. Hence even during peak months for dust lifting in Asia, smaller dust optical depths occur than during peak months in Africa.

The annual dust flux near the dust source is about 1088Tg/year across 10W (10S-40N, 10W) and 355Tg/year across 105E (25N-55N, 105E) for Sahara and Asia in 2007, respectively. Saharan deserts are largely south of 30N, while Asian ones are primarily north of 30N. This leads them to experience different meteorological regimes. Saharan dust lifting occurs all year long, primarily due to subtropical weather systems. The Saharan dust transport into the Caribbean is controlled primarily by a semi-permanent high, the Azores High. Dust lifting from African dust sources can be triggered and modulated by synoptic systems, such as African easterly waves. The dust outbreaks usually occur within the ridge region of passing easterly waves with a period of 5-7 days. In contrast, 45% of Asian dust was lifted in spring during the modeled year of 2007, when mid-latitude frontal systems lead to high winds. The seasonal variation of dust outbreaks in Asia is associated with the seasonal modulation of the wind speed. Strong winds occur most frequently in spring in Asia due to the activity of the mid-latitude frontal systems. The mid-latitude frontal cyclones associated with intense cold fronts from Mongolia to northeastern China not only generate dust storms, but can also lift Asian dust into the westerly jet in the upper troposphere.

Rainfall is more abundant over Asia during the dust lifting events than over the Sahara, leading to greater local dust removal than over the Sahara. However, wet removal is a small fraction of the total removal of dust, and removal processes do not account for the difference in annual dust flux between the Sahara and Asia. Instead, the Sahara simply has about three times as much area with dust lifting as Asia because Asia

has smaller deserts and also more vegetation and snow cover, which suppresses dust lifting.

During the major lifting season the power averaged winds over Africa and Asia are similar. However in other seasons Africa has stronger winds than does Asia, which further contributes to more dust lifting over Africa. The power-averaged wind contributes about a factor of 1.7 to the differences of the total dust fluxes between the two sources averaged over the year.

The vertical distribution of Asian and African dust also differs in the cases we considered. The Saharan dust is primarily located in a deep layer, the SAL. The top of the layer descends during transport, which we conclude is mainly due to descending air in the Azores High. There are two noticeable layers of Asian dust during transport in May. One layer stays well above boundary layer, and does not descend with time. The other dust layer is in a shallow near surface boundary layer and descends with time. The transport of Asian dust is dominated by the westerlies at high altitudes, while it is controlled by regional weather systems and topography at lower altitudes. Sedimentation does not seem to play a significant role in the descent of long lasting layers. Horizontal wind shear can also play a role in creating elevated dust layers by moving dust horizontally, which is particularly important over Asia.

The size distribution of Asian dust (at Xianghe) is bi-modal while that of Saharan dust (at Dakar) is uni-modal. The volume size distribution of Asian dust peaks around 2 microns, whereas it peaks around 1 micron for Saharan dust. Both model simulations and the AERONET retrievals show similar patterns. We suggest these differences originate from mixing in the boundary layers, and the vertical winds that occur during transport. For the case we studied, winds over Africa were descending in a well-mixed deep boundary layer, while those over Asia were ascending and there was no deep boundary layer. The ascending winds may be strong enough to loft micron sized dust.

I assume the real part of the complex refractive index is independent of wavelength (1.55) both for Asian dust and Saharan dust based on the AERONET retrievals and previous studies. We use data on the imaginary part of the refractive index from AERONET site measurements near the dust source regions. We find that the average single scattering albedo is larger for Asian dust than the Saharan dust. This is consistent with the refractive indices inferred by AERONET for the two dust sources, and with a previous study showing that the dust transported from Asia to the Pacific may not absorb as much light as the dust from the Sahara. As the size distribution evolves downwind of the sources due to the vertical winds experienced during transport, and as pollutants are added to the dust, the single scattering albedos will evolve.

The importance of the uncertainty in the SSA to the radiative effects of dust on the climate of China is explored through two case studies based on the modeled and observed solar diffuse fluxes/irradiances at the surface. The integrated three-dimensional microphysical-climate-radiation model used in this study allows us to consider interactions with the local surface albedo and emissivity, evolution of the size distribution in time, the vertical distribution of the dust as well as transport of dust aerosols vertically and horizontally.

The SSA values are around 0.94 near the dust sources from case-Shi, whereas it's about 0.82 for case-Ge. The SSA values increased during transport away from the source reaching 0.96 for case-Shi and 0.84 for case-Ge in Japan. This increase in SSA is caused by the decreasing size of the particles as they move away from the source, since smaller particles have higher SSA for particles in this size range.

The dust net radiative flux at the TOA is larger in case-Ge than case-Shi, by up to 6 W m^{-2} near dust sources, and decreases during dust transport away from the sourcecs The larger imaginary part of refractive index in case-Ge results in smaller SSA compared with case-Shi. Therefore the dust aerosols from case-Ge absorb more solar energy so

less is reflected at TOA and the shortwave net flux is larger than in case-Shi. The radiative forcing at TOA is very sensitive to the SSA values, and the shortwave radiative forcing is the greatest difference between the Shi and Ge cases. The change in the net fluxes at surface are both negative. As we defined the downward fluxes as positive, the positive radiative TOA flux (downward) and larger negative surface flux (upward) from case-Ge indicates larger dust direct radiative forcing in the atmosphere compared with the one from case-Shi, so there are greater warming effects to the atmosphere from case-Ge.

There is about 3 times larger heating in case-Ge compared with case-Shi for the shortwave heating rates in July 2006. The heating rates of shortwave radiation for case-Ge was up to 6 K day^{-1} on July 12 to 16 and July 28, 2006 in heavy dust layers, and around 3 K day^{-1} on other days in July 2006 over the Taklimakan desert. For case-Shi, the maximum of the shortwave heating rates are about 2 K day^{-1} on July 12 to 16, 2006, and they are 1 K day^{-1} on other days in July 2006.

The longwave radiative heating rates show warming effects in and below dust layers and cooling effects on the top of dust layers both for case-Shi and case-Ge with maximum heating near the surface. There is the same dust heating in case-Ge and case-Shi and it is up to 0.5 K day^{-1} on July 14. The longwave cooling rates on the top of the dust layers are around -0.2 K day^{-1} for both two cases. This longwave cooling is smaller than the dust solar heating rates in the same layers. The longwave radiative heating rates show more cooling near the surface compared with Taklimakan and Beijing cases both for case-Shi and case-Ge. The differences can be explained by the different surfaces for these locations. The Taklimakan desert has a brighter and hotter surface that emits more longwave radiation that can interact efficiently with large particles near the dust sources, whereas the dark and cold ocean emits less longwave

radiation that has less chance to interact with dust aerosols over the Sea of Japan. The net dust heating rates are generally positive.

There are larger negative dust net radiative fluxes at surface in case-Ge compared with case-Shi near dust sources, which results in lower surface temperature (negative) in case-Ge than in case-Shi. This means there is more dust radiative effect on surface temperature if we use a larger imaginary part of the dust refractive index (such as 0.01 at 0.67 um) or a smaller SSA (0.82) in case-Ge compared with case-Shi (around 0.002 for refractive index at 0.67um) and 0.94 for SSA).

Bibliography

Ackerman, A.S., P.V. Hobbs, and O.B. Toon, A model for particle microphysics, turbulent mixing, and radiative transfer in the stratocumulus-topped marine boundary layer and comparisons with measurements. J. Atmos. Sci., 52, 1204-1236, 1995.

Alfaro, S. C., A. Gaudichet, L. Gomes, and M. Maill´e, Modeling the size distribution of a soil aerosol produced by sandblasting, *J. Geophys. Res.*, *102*, 11239–11249, 1997.

Alfaro, S. C., A. Gaudichet, L. Gomes, and M. Maille, Mineral aerosol production by wind erosion: aerosol particle sizes and binding energies, *Geophys. Res. Letters*, *25*, 991–994, 1998.

Alfaro, S. C., and L. Gomes, Modeling mineral aerosol production by wind erosion: Emission intensities and aerosol size distributions in source areas, *J. Geophys. Res.*, *106*, 18,075–18,084, 2001.

Alfaro, S. C., L. Gomes, J. L. Rajot, S. Lafon, A. Gaudichet, B. Chatenet, M. Maille, G. Cautenet, F. Lasserre, and X. Y. Zhang, Chemical and optical characterization of aerosols measured in spring 2002 at Chinese Ace-Asia Supersite (Zhenbeitai) China, *J. Geophys. Res*., 108(D23), 8641, doi:10.1029/2002JD003214, 2003.

Arellano Jr., A., Raeder, K., Anderson, J., Hess, P., Emmons, L., Edwards, D., Pfister, G., Campos, T., and Sachse, G.: Evaluating model performance of an ensemble-based chemical data assimilation system during INTEX-B field mission, Atmos. Chem. Phys., 7, 5695-5710, 2007.

Arimoto, R., X. Y. Zhang, B. J. Huebert, C. H. Kang, D. L. Savoie, J. M. Prospero, S. K. Sage, C. A. Schloesslin, H. M. Khaing, and S. N. Oh, Chemical composition of atmospheric aerosols from Zhenbeitai, China, and Gosan, South Korea, during ACE-Asia, J. Geophys. Res., 109, D19S04, 2004.

Balkanski, Y. J., D. J. Jacob, G. M. Gardner, W. C. Graustein, and K. K. Turekian , Transport and residence times of tropospheric aerosols inferred from a global three-dimensional simulation of 210Pb, *J. Geophys.Res.*, *98*(D11), 20,573–20,586, 1993.

Barth, M. C., P. J. Rasch, J. T. Kiehl, C. M. Benkovitz, and S. E. Schwartz , Sulfur chemistry in the National Center for Atmospheric Research Community Climate Model: Description, evaluation, features, and sensitivity to aqueous chemistry, *J. Geophys. Res., 105*, 1387-1415, 2000.

Bardeen, C. G., O. B. Toon, E. J. Jensen, D. R. Marsh, and V. L. Harvey, Numerical simulations of the three- dimensional distribution of meteoric dust in the mesosphere and upper stratosphere, *J. Geophys. Res.,* doi:10.1029/2007JD009515, 2008.

Betzer et al., Long-range transport of giant mineral aerosol particles, *Nature,* vol. 336, 568-571, 1988.

Bodhaine B. A., Aerosol measurements during the Mauna Loa Photochemistry Experiment 2, *J. Geophys. Res.,* 101, 14,757-14,765, 1996.

Cairo F., Donfrancesco, G., Adriani, A., Pulvirenti, L., and Fierli F.: Comparison of Various Linear Depolarization Parameters Measured by Lidar, Appl. Opt. 38, 4425-4432, 1999.

Carmichael, G. R., et al., Evaluating regional emission estimates using the TRACE-P observations*, J. Geophys. Res.,* 108(D21), 8810, doi:10.1029/2002JD003116, 2003.

Chin, M., P. Ginoux, R. Lucchesi, B. Huebert, R. Weber, T. Anderson, S. Masonis, B. Blomquist, A. Bandy, and D. Thornton, A global aerosol model forecast for the ACE-Asia field experiment, J. Geophys. Res., 108(D23), 8654, doi:10.1029/2003JD003642, 2003.

Chin, M., D. A. Chu, R. Levy, L. A. Remer, Y. J. Kaufman, B. N. Holben, T. Eck, and P. Ginoux, Aerosol distribution in the Northern Hemisphere during ACE-Asia: Results from global model, satellite observations, and Sun photometer measurements, J. Geophys. Res., 109, D23S90, doi:10.1029/2004JD004829, 2004.

Clarke, A. D., W. G. Collins, P. J. Rasch, V. N. Kapustin, K. Moore, S. Howell, and H. E. Fuelberg , Dust and pollution transport on global scales: Aerosol measurements and model predictions, J. Geophys. Res., 106, 32,555–32,569, 2001.

Colarco, P. R., O. B. Toon, O. Torres, and P. J. Rasch, Determining the UV imaginary index of refraction of Saharan dust particles from Total Ozone Mapping Spectrometer data using a three-dimensional model of dust transport, *J. Geophys. Res*., 107 (D16), 4312, doi:10.1029/2001JD000903, 2002.

Colarco, P. R., O. B. Toon, B. N. Holben, Saharan dust transport to the Caribbean during PRIDE: 1. Influence of dust sources and removal mechanisms on the timing and magnitude of downwind aerosol optical depth events from simulations of in situ and remote sensing observations, *J. Geophys. Res*., 108 (D19), 8589, 2003a**.**

Colarco, P. R., et al., Saharan dust transport to the Caribbean during PRIDE: 2. Transport, vertical profiles, and deposition in simulations of in situ and remote sensing observations, *J. Geophys. Res*., 108 (D19), 8590, 2003b.

Collins, W. D., P. J. Rasch, and Others, Description of the NCAR Community Atmosphere Model (CAM 3.0), Technical Report NCAR/TN-464+STR, National Center for Atmospheric Research, Boulder, Colorado, 210 pp., 2004.

Cuesta J., Marsham J. H., Parker D. J.: Flamant C, Dynamical mechanisms controlling the vertical redistribution of dust and the thermodynamic structure of the West Saharan atmospheric boundary layer during summer, Atmos. Sci. Lett. 10: 34-42, 2009.

Dana, T. M., and J. M. Hales, Statistical aspects of the washout of polydisperse aerosols, *Atmos. Environ.*, 10, 45-50, 1976.

Dave, J. V., Report 320-3236, IBM Scientific Center, Palo Alto, Calif, 1968.

Díaz J. P., Exposito, F. J., Torres, C. J., Carreño, V., and Redondas, A.: Simulation of mineral dust effects on UV-radiation levels, Journal of Geophysical Research 105,

pp. 4979–4991, 2000.

Dickinson, R.E. et al., The Community Land Model and it's climate statistics as a component of the Community Climate System Model. *J. Clim.,* 19, w302-2324, 2006.

Doherty, O. M., Riemer, N., and Hameed, S.: Saharan mineral dust transport into the Caribbean: Observed atmospheric controls and trends, J. Geophys. Res., 113, D07211, doi:10.1029/2007JD009171, 2008.

Draxler, R. R., and Rolph, G. D.: HYSPLIT (Hybrid Single-Particle Lagrangian Integrated Trajectory) model, Air Resour. Lab., NOAA, Silver Spring, Md. (Available at http://www.arl.noaa.gov/ready/hysplit4.html), 2003.

Dubovik, O., et al., Accuracy assessments of aerosol optical properties retrieved from AERONET sun and sky radiance measurements, J. Geophys. Res., 105, 9791–9806, 2000.

Dubovik, O., et al., Application of spheroid models to account for aerosol particle nonsphericity in remote sensing of desert dust, J. Geophys. Res., 111, D11208, doi:10.1029/2005JD006619, 2006.

Duce, R.: The atmospheric input of trace species to the world ocean, Global Biogeochem. Cycle, 5, 193–259, 1991.

Duce, R. A., et al., Long-range atmospheric transport of soil dust from Asia to the tropical North Pacific: temporal variability, *Science,* vol. 209, 1522-1524, 1980.

Dunion, J. P., and Velden, C. S.: The impact of Saharan air layer on Atlantic tropical cyclone activity, Bull. Am. Meteorol. Soc., 85, 353–365, doi:10.1175/BAMS-85-3-353, 2004.

Eguchi, K., Uno, I., Yumimoto, K., Takemura, T., Shimizu, A., Sugimoto, N., and Liu, Z.: Trans-Pacific dust transport: integrated analysis of NASA/CALIPSO and a global aerosol transport model, Atmos. Chem. Phys. Discuss., 9, 4013-4034, 2009.

Fan, S. M., W. J. Moxim, and H. Levy II, Implications of droplet nucleation to mineral dust aerosol deposition and transport, *Geophys. Res. Lett.*, *32*, L10805, doi:10.1029/2005GL022833, 2005.

Fan, S. M., L. W. Horowitz, H. Levy II, and W. J. Moxim, Impact of air pollution on wet deposition of mineral dust aerosols, *Geophys. Res. Lett.*, *31*, L02104, doi:10.1029/2003GL018501, 2004.

Fernald F. G., Herman B. M., Reagan J. A.: Determination of aerosol height distributions by lidar. Journal of Atmospheric Meteorology 11: 482-489, 1972.

Fernald, F. G.: Analysis of atmospheric lidar observations: some comments, Appl. Opt., 23, 652–653, 1984.

Ge, J., Su, J., T. P. Ackerman, Fu, Q., Huang, J., and Shi, J.: Dust aerosol optical properties retrieval and radiative forcing over northwestern China during the 2008 China-U.S joint field experiment, J. Geophys. Res., 115, D00K12, doi: 10.1029/1009JD013263, 2010.

Ge, J. M., J. P. Huang, J. Su, J. R. Bi, and Q. Fu, Shortwave radiative closure experiment and direct forcing of dust aerosol over northwestern China, *Geophys.*

Res. Lett., 38, L24803, doi:10.1029/2011GL049571, 2011.

Generoso, S., Bey, I., Labonne, M., and Bréon, F. M.: Aerosol vertical distribution in dust outflow over the Atlantic: Comparisons between GEOS-Chem and Cloud-Aerosol Lidar and Infrared Pathfinder Satellite Observation (CALIPSO), J. Geophys. Res., 113, D24209, doi:10.1029/2008JD010154, 2008.

Gillette, D. A., and R. Passi, Modeling dust emission caused by wind erosion, *J. Geophys. Res.*, *93*, 14233–14242, 1988.

Ginoux, P., M. Chin, I. Tegen, J. M. Prospero, B. Holben, O. Dubovik, and S.-J. Lin:Sources and distributions of dust aerosols simulated with the GOCART model. *J. Geophys.Res.*, 106, 20,255-20,273, 2001.

Ginoux, P.: Aerosol distribution in the Northern Hemisphere during ACE-Asia: Results from global model, satellite observations, and Sun photometer measurements, J. Geophys. Res., 109, D23S90, doi:10.1029/2004JD004829, 2004.

Gomes, L., G. Bergametti, G. Coud´e-Gaussen, and P. Rognon, Submicron desert dusts: A sandblasting process, *J. Geophys. Res.*, *95*, 13927–13935, 1990.

Gong, S. L., X. Y. Zhang, T. L. Zhao, I. G. McKendry, D. A. Jaffe, and N. M. Lu, Characterization of soil dust aerosol in China and its transport and distribution during 2001 ACE-Asia: 2. Model simulation and validation, J. Geophys. Res., 108(D9), 4262, doi:10.1029/2002JD002633, 2003.

Gong, S. L., Zhang, X. Y., Zhao, T. L., McKendry, I. G., Jaffe, D. A., and Lu, N. M.: Characterization of soil dust aerosol in China and its transport and distribution during 2001 ACE-Asia: 2. Model simulation and validation, J. Geophys. Res., 108(D9), 4262, doi:10.1029/2002JD002633, 2003.

Grini, A., and C. S. Zender, Roles of saltation, sandblasting, and wind speed variability on mineral dust aerosol size distribution during the Puerto Rican Dust Experiment (PRIDE). *J.Geophys. Res.*, 109, D07202, 2004.

Grini, A., G. Myhre, C. S. Zender, J. K. Sundet, and I. S. A. Isaksen, Model simulations of dust sources and transport in the global troposphere: Effects of soil erodibility and wind speed variability, J. Geophys. Res., 110, D02205, doi:10.1029/2004JD005037, 2005.

Grousset FE, Ginoux P, Bory A, Biscaye PE, Case study of a Chinese dust pume reaching the French Alps., *Geophysical Resaerch Letters* 30: 1277, DOI:10.029/2002/g1016833, 2003.

Hahn, C. J., J. T. Merrill, B. G. Mendonca, Meteorological influences during MLOPEX, *J. Geophys. Res,* Vol. 97, 10,291-10,309, 1992.

Haywood, J. M., et al.: Can desert dust explain the outgoing longwave radition anomaly over the Sahara during July 2003?, J. Geophys. Res.-Atmos., 110, D05105, 2005.

Haywood, J. M., et al.: Overview of the Dust and Biomass-burning Experiment and African Monsoon Multidisciplinary Analysis Special Observing Period-0, J. Geophys. Res., 113, D00C17, doi:10.1029/2008JD010077, 2008.

Heese, B., and Wiegner, M.: Vertical aerosol profiles from Raman polarization lidar observations during the dry season AMMA field campaign, J. Geophys. Res., 113, D00C11, doi:10.1029/2007JD009487, 2008.

Heintzenberg, J., The SAMUM-1 experiment over Southern Morocco: overview and introduction, Tellus, DOI: 10.1111/j.1600-0889.2008.00403.x, 2-11, 2008.

Holben, B.N. et al., AERONET-A federated instrument network and data archive for aerosol characterization, *Remote Sens. Environ*., 66, 1-16, 1998.

Hsu, N. C., S. C. Tsay, M. D. King, and J. R. Herman, Deep blue retrievals of Asian aerosol properties during ACE-Asia. *IEEE Trans. Geosci. Remote Sens.*, 44**,** 3180-3195, 2006.

Huang, J., Minnis, P., Yi, Y., Tang, Q., Wang, X., Hu, Y., Liu, Z., Ayers, K., Trepte, C., and Winker, D.: Summer dust aerosols detected from CALIPSO over the Tibetan Plateau, Geophys. Res. Lett., 34, L18805, doi:10.1029/2007GL029938, 2007.

Huang, J., Minnis, P., Chen, B., Huang, Z., Liu, Z., Zhao, Q., Yi, Y., and Ayers, J. K.: Long-range transport and vertical structure of Asian dust from CALIPSO and surface measurements during PACDEX, J. Geophys. Res., 113, D23212, doi:10.1029/2008JD010620, 2008.

Huang, J., Fu, Q., Su, J., Tang, Q., Minnis, P., Hu, Y., Yi, Y., and Zhao, Q.: Taklimakan dust aerosol radiative heating derived from CALIPSO observations using the Fu-Liou radiation model with CERES constraints, Atmos. Chem. Phys., 9, 4011-4021, 2009.

Huebert, B., T. Bates, P. B. Russell, G. Shi, Y. J. Kim, K. Kawamura, G. Carmichael, and T. Nakajima, An overview of ACE-Asia: Strategies for quantifying the relationships between Asian aerosols and their climate impacts, J. Geophys. Res., 108(D23), 8633, doi:10.1029/2003JD003550, 2003.

Husar, R. B., et al., Asian dust events of April 1998, J. Geophys. Res., 106, 18,317–18,330, 2001.

IPCC, *Climate Change 2001: The Scientific Basis*, Technical Summary of the Working Group I Report, 2001.

IPCC, *Climate Change 2007*: *The Physical Science Basis,* Contribution of Working Group 1 to the Fourth Assessment Report of the Intergovernmental Panel On Climate Change [Solomon, S., D. Qin, M. Manning, Z. Chen, M. Marquis, K.B. Averyt,M.Tignor and H.L. Miller (eds.)]. Cambridge University Press, Cambridge, United Kingdom and New York, NY, USA, 2007.

Iversen, J., and B. White, Saltation threshold on Earth, Mars and Venus, Sedimentology, 29, 111–119, 1982.

Iwasaka, Y., M. Yamato, R. Imasu, and A. Ono, Transport of Asian dust (kosa) particles: Importance of weak kosa events on the geochemical cycle of soil particles, *Tellus, Ser.* B, 40, 494–503, 1998.

Jacob, D. J., Crawford, J. H., Kleb, M. M., Connors, V. S., Bendura, R. J., Raper, J. L., Sachse, G. W., Gille, J. C., Emmons, L., and Heald, C. L.: Transport and Chemical Evolution Over the Pacific (TRACE-P) aircraft mission: Design, execution, and first results, J. Geophys. Res., 108(D20), 9000, doi:10.1029/2002JD003276, 2003.

Jensen, E. J., O. B. Toon, D. L. Westphal, S. Kinne, and A. J. Heymsfield, Microphysical modeling of cirrus: 1. Comparison with 1986 FIRE IFO measurements, *J. Geophys. Res.,* 99, 10,421–10,442, 1994.

Jones, C., Mahowald, N, and Luo, C.: The role of easterly waves on African desert dust

transport, J. Clim., 16(22), 3617– 3628, 2003.

Justus, C., W. Hargraves, A. Mikhail, and D. Graber, Methods for estimating wind speed frequency distributions, *J. App. Met.*, *17*,350–353, 1978

Kalnay E., M. Kanamitsu, R. Kistler, W. Collins, D. Deaven, L. Gandin, M. Iredell, S. Saha, G. White, J. Woollen, Y. Zhu, M. Chelliah, W. Ebisuzaki, W.Higgins, J. Janowiak, K. C. Mo, C. Ropelewski, J. Wang, A. Leetmaa, R. Reynolds, Roy Jenne, Dennis Joseph. "The NCEP/NCAR 40-Year Reanalysis Project". Bulletin of the American Meteorological Society 77 (3): 437–471, 1996.

Kandler, P., et al.: Size distribution, mass concentration, chemical and mineralogical composition and derived optical parameters of the boundary layer aerosol at Tinfou, Morocco,during SAMUM 2006, DOI: 10.1111/j.1600-0889.2008.00385.x, 32-50, 2008.

Karyampudi, V., et al.: Validation of the Saharan dust plume conceptual model using lidar, Meteosat, and ECMWF data, Bull. Am. Meteorol. Soc., 80, 1045–1075, 1999.

Kaufman, Y. J., D. Tanre, O. Dubovik, A. Karnieli, and L. A. Remer: Absorption of sunlight by dust as inferred from satellite and ground-based remote sensing. *Geophys. Res. Lett.*, **28**, 1479-1483, 2001.

Kaufman, Y. J., and Fraser, R. S.: The effect of smoke particles on cloud and climate forcing, Science, 277, 1636–1639, 1997.

Kistler, R., Kalnay, E., Collins, W., Saha, S., White, G., Woollen, J., Chelliah, M., Ebisuzaki, W., Kanamitsu, M., Kousky, V., van den Dool, H., Jenne, R., Fiorino, M.: The NCEP-NCAR 50-year reanalysis: monthly means CD-ROM and documentation. Bull. Amer. Meteor. Soc., vol. 82 (2) pp. 247-267, 2001.

Laurent, B., Marticorena, B., Bergametti, G., Mei, F.: Modeling mineral dust emissions from Chinese and Mongolian deserts, Global and Planetary Change, 52, 121-141, 2006.
Lee, E.-H., and Sohn, B.-J.: Examining the impact of wind and surface vegetation on the Asian dust occurrence over three classified source regions, J. Geophys. Res., 114, D06205, doi:10.1029/2008JD010687, 2009.
Lee, E.-H., and Sohn, B.-J.: Examining the impact of wind and surface vegetation on the Asian dust occurrence over three classified source regions, J. Geophys. Res., 114, D06205, doi:10.1029/2008JD010687, 2009.

Levin, Z. and E. Ganor, The effects of desert particles on cloud and rain formation in the eastern Mediterranean. In Impact of Desert Dust Across The Mediterranean, Ed. S. Guerzoni and R. Chester, *Kluwer Academic Pub*. 77-86, 1996.

Lin, S.J., and R.B. Rood, Multidimensional flux-form semi-Lagrangian transport schemes, *Mon. Wea. Rev*., 124, 2046, 1996.

Liu, D., Wang, Z., Liu, Z., Winker, D., and Trepte, C.: A height resolved global view of dust aerosols from the first year CALIPSO lidar measurements, J. Geophys. Res., 113, D16214, doi:10.1029/2007JD009776, 2008.

Liu, M., and D. Westphal, A study of the sensitivity of simulated mineral dust production to model resolution, *J. Geophys. Res.*, 106, 18,099–18,112, 2001.

Liu, X., Penner, J. E., and Herzog, M.: Global modeling of aerosol dynamics: Model description, evaluation, and interactions between sulfate and nonsulfate aerosols, J. Geophys. Res., 110, D18206, doi:10.1029/2004JD005674, 2005.

Liu, Z., Hunt, W., Vaughan, M., Hostetler, C., McGill, M., Powell, K., Winker, D., and Hu, Y.: Estimating random errors due to shot noise in backscatter lidar observations, Appl. Opt., 45, 4437–4447, 2006.

Liu, Z., Liu, D., Huang, J., Vaughan, M., Uno, I., Sugimoto, N., Kittaka, C., Trepte, C., Wang, Z., Hostetler, C., and Winker, D.: Airborne dust distributions over the Tibetan Plateau and surrounding areas derived from the first year of CALIPSO lidar observations, Atmos. Chem. Phys., 8, 5045-5060, 2008.

Liu Z., et al.: CALIPSO lidar observations of the optical properties of Saharan dust: A case study of long-range transport. J. Geophys. Res., 113, D07207, doi:10.1029/2007JD008878, 2008b.

Lyamani ,H., Olmo, F. J., Alados-Arboledas, L.: Saharan dust outbreak over southeastern Spain as detected by sun photometer Atmospheric Environment, 39 (38), pp. 7276-7284, 2005.

Liu, Z., Sugimoto, N., and Murayama, T.: Extinction-to-backscatter ratio of Asian dust observed by high-spectral-resolution lidar and Raman lidar, *Appl. Opt*., 41, 2760-2767, 2002.

Mahowald, N., M. Yoshioka, W. Collins, A. Conley, D. Fillmore, D. Coleman, Climate response and radiative forcing from mineral aerosols during the glacial maximum, pre-industrial, current and doubled-carbon dioxide climates, *GRL*, 33, L20705, doi:10.1029/2006GL026126, 2006.

Mahowald, N., Kohfeld, K., Hansson, M., Balkanski, Y., Harrison, S.P., Printice, I.C., Schulz, M., Rodhe, H., Dust sources and deposition during the last glacial maximum and current climate: a comparison of model results with paleodata from ice cores and marine sediments. *J. Geophys. Res.* 104,15895–15916, 1999.

Maring, H., Savoie, D. L., Izaguirre, M. A., and Custals, L.: Vertical distributions of dust and sea salt over Puerto Rico during PRIDE measured from a light aircraft, J. Geophys., 108, doi:10.1029/2002JD002544, 2003.

Marsham, J. H., et al.: Observations of mesoscale and boundary-layer scale circulation affecting dust transport and uplift over the Sahara, Atmos. Chem. Phys., 8, 6979-6993, 2008.

Marticorena, B., and G. Bergametti, Modeling the atmospheric dust cycle: 1. Design of a soil-derived dust emission scheme, *J. Geophys. Res*., 100, 16,415–16,430, 1995.

Marticorena, B., G. Bergametti, B. Aumont, Y. Callot, C. N'Doum´e, and M. Legrand, Modeling the atmospheric dust cycle: 2. Simulation of Saharan dust sources, *J. Geophys. Res.*, *102*, doi:10.1029/96JD02964, 4387–4404, 1997.

Martin, J. H.: Testing the iron hypothesis in ecosystem of the equatorial Pacific Ocean, Nature, 371, 123–129, 1994.

Masson, V., J. Champeaux, F. Chauvin, C. Meriguet, and R. Lacaze, A global database of land surface parameters at 1-km resolution in meteorological and climate models. *Journal of Climate*, volume16, 1261-1282, 2003.

McKendry, I. G., Macdonald, A. M., Leaitch, W. R., van Donkelaar, A., Zhang, Q., Duck, T., and Martin, R. V.: Trans-Pacific dust events observed at Whistler, British Columbia during INTEX-B, Atmos. Chem. Phys. Discuss., 8, 10275-10300, 2008.

McNaughton C. S., et al.: Observations of heterogeneous reactions between Asian pollution and mineral dust, Atmos. Chem. Phys., 9, 8288-8308, 2009.

Mishchenko, M. I., L. D. Travis, and D. W. Mackowski: T-matrix computations of light scattering by nonspherical particles: a review, *J. Quant. Spectrosc. Radiat. Transfer* 55, 535-575, 1996.

Muller, D., et al.: EARLINET observations of the 14–22-May long-range dust transport event during SAMUM 2006: validation of results from dust transport modeling, Tellus, DOI: 10.1111/j.1600-0889.2008.00400.x, 325-339, 2008.

Müller, D., K. Franke, A. Ansmann, D. Althausen, and F. Wagner, Indo-Asian pollution during INDOEX: Microphysical particle properties and single-scattering albedo inferred from multiwavelength lidar observations, J. Geophys. Res., 108(D19), 4600, 2003.

Nowottnick, E., Colarco, P., Ferrare, R., Chen, G., Ismail, S., Anderson, B., and Browell, E.: Online simulations of mineral dust aerosol distributions: Comparisons to NAMMA observations and sensitivity to dust emission parameterization, J. Geophys. Res., 115, D03202, doi:10.1029/2009JD012692, 2010.

Pandithurai, G., Dipu S., Dani K. K., Tiwari S., Bisht D. S., Devara P. C. S., and Pinker R. T.: Aerosol radiative forcing during dust events over New Delhi, India.. J. Geophys. Res., 113, D13209, doi: 10.1029/2008JD009804, 2008.

Patterson E. M., Gillette, D., and Stockton, B. H.: Complex index of refraction between 300 and 700 nm for Saharan aerosols, Journal of Geophysical Research 82, pp. 3153–3160, 1997.

Pfister, L., Selkirk, H. B., Starr, D. O., Rosenlof, K., and Newman, P. A.: A Meteorological Overview of the TC4 Mission, J. Geophys. Res., doi:10.1029/2009JD013316, in press, 2010.

Prospero, J.: Long-term measurements of the transport of African mineral dust to the southeastern United States: Implications for regional air quality, J. Geophys. Res., 104, 15,917–15,927, 1999.

Prospero, J.: The atmospheric transport of particles to the ocean, in Particle Flux in the Ocean, edited by V. Ittekkot et al., pp. 18–152, John Wiley, New York, 1996.

Prospero, J., and Carlson, T.: Saharan air outbreaks over the tropical North Atlantic, Pure Appl. Geophys., 119, 677–691, 1981.

Prospero, J. M. and Carlson, T. N.: Vertical and areal distribution of Saharan dust over the western equatorial North Atlantic ocean, J. Geophys. Res., 77 5255–65, 1972

Prupacher, H.R., and J.D. Klett, Microphysics of Clouds and Precipitation, *Kluwer Academic Publisher*s,1997.

Rajot, J. L., et al.: AMMA dust experiment: An overview of measurements performed during the dry season special observation period (SOP0) at the Banizoumbou (Niger) supersite, J. Geophys. Res., 113, D00C14, doi:10.1029/2008JD009906, 2008.

Ramanathan, V., et al.: The Indian Ocean Experiment: An integrated assessment of the climate forcing and effects of the great Indo-Asian haze, J. Geophys. Res., 106(D22), 28,371– 28,399,doi:10.1029/2001JD900133, 2001.

Rasch, P. J., N. M. Mahowald, and B. E. Eaton, Representations of transport, convection, and the hydrologic cycle in chemical transport models: Implications for the modeling of short-lived and soluble species, *J. Geophys. Res.*, 102, 28,127–28,138, 1997.

Rasch, P. J., W. D. Collins, and B. E. Eaton: Understanding the Indian Ocean Experiment (INDOEX) aerosol distributions with an aerosol assimilation. *J. Geophys. Res*., **106**, 7337-7355, 2001.

Rea, D. K., Leinen, M., and Janecek, T. R.: Geologic approach to the long-term history of atmospheric circulation, Science, 227, 721–725, 1985.

Reid, J. S., Westphal, D. L., Livingston, J. M., Savoie, D. L., Maring, H. B., Jonsson, H. H., Eleuterio, D. P., Kinney, J. E., and Reid, E. A.: Dust vertical distribution in the Caribbean during the Puerto Rico Dust Experiment, Geophys. Res. Lett., 29(7), 1151, doi:10.1029/2001GL014092, 2002.

Reid, J. S., et al.: Analysis of measurements of Saharan dust by airborne and ground-based remote sensing methods during the Puerto Rico Dust Experiment (PRIDE), J. Geophys. Res., 108(D19), 8586, doi:10.1029/2002JD002493, 2003b.

Sassen, K.: Lidar backscatter depolarization technique for cloud and aerosol research, in Light Scattering by Nonspherical Particles: Theory, Measurements, and Geophysical Applications, edited by M. L. Mishchenko, J. W. Hovenier, and L. D. Travis, pp. 393–416, Academic Press, San Diego, 2000.

Schulz, M., Y. Balkanski, W. Guelle, and F. Dulac, Role of aerosol size distribution and source location in a three dimensional simulation of a saharan dust episode tested against stellite derived optical thickness, *J. Geophys. Res.*, *103*, 10579–10592, 1998.

Seinfeld, J. H., et al.: ACE-ASIA—Regional climatic and atmospheric chemical effects of Asian dust and pollution, Bull. Am. Meteorol. Soc., 85(3), 367–380, doi:10.1175/BAMS-85-3-367, 2004.

Seinfeld, J.H., and S.N. Pandis, Atmospheric Chemistry and Physics: From Air Pollution to Climate Change, John Wiley & Sons, 1998.

Shao, Y., and M. Raupach, Effect of saltation bombardment by wind, *J. Geophys. Res*, *98*, 12719–12726, 1993.

Shao, Y., M. R. Raupach, and J. F. Leys, A model for predicting Aeolian sand drift and dust entrainment on scales from paddock to region, *Aust. J. Soil Res*., 34, 309– 342, 1996.

Shao, Y., and I. Lu, A simple expression for wind erosion threshold friction velocity, *J.*

Geophys. Res., *105*, 22437–22443, 2000.

Shaw, G. E., Transport of Asian Desert Aerosol to the Hawaiian Islands, *J. of Applied Meteorology*, vol. 19, 1254- 1259, 1980.

Shi, G., H. Wang, B. Wang, and W. Li, Sensitivity experiments on the effects of optical properties of dust aerosols on their radiative forcing under clear sky condition, JMSJ, Vol. 83A, 333-346, 2005.

Shimizu, A., N. Sugimoto, I. Matsui, K. Arao, I. Uno, T. Murayama, N. Kagawa, K. Aoki, A. Uchiyama, and A. Yamazaki , Continuous observations of Asian dust and other aerosols by polarization lidars in China and Japan during ACE-Asia, *J.* Geophys. Res., 109, D19S17, 2004.

Shinn, E. A., Smith, J. M., Prospero, G. W., Betzer, P., Hayes, M. L., Garrison, V., and Barber, R. T.: African dust and the demise of Caribbean coral reefs, Geophys. Res. Lett., 27, 3029–3032, 2000.

Smirnov A., B.N. Holben, D. Savoie, J.M. Prospero, Y.J. Kaufmann, D. Tanré, T.F. Eck and I.S. Slutsker, Relationship between column aerosol optical thickness and in situ ground based dust concentrations over Barbados, *Geophys. Res. Lett*. 27, pp. 1643–1646, 2000.

Sokolik, I. N., and O. B. Toon: Incorporation of mineralogical composition into models of the radiative properties of mineral aerosol from UV to IR wavelengths. *J. Geophys. Res.,* **104,** 9423–9444, 1999.

Sokolik, I., and O. B. Toon, Direct radiative forcing by anthropogenic airborne mineral aerosols. *Nature* 381,681, 1996.

Stith, J. L., et al.: An overview of aircraft observations from the Pacific Dust Experiment campaign, J. Geophys. Res., 114, D05207, doi:10.1029/2008JD010924, 2009.

Stull, R. B., An Introductiont o BoundaryL ayer Meteorology3, 76-379 pp., Kluwer Acad., Norwell, Mass.,1988.

Su, L., and Toon, O. B.: Numerical simulations of Asian dust storms using a coupled climate-aerosol microphysical model, J. Geophys. Res., 114, D14202, doi:10.1029/2008JD010956, 2009.

Su, L., and O. B. Toon, Saharan and Asian dust: similarities and differences determined by CALIPSO, AERONET, and a coupled climate-aerosol microphysical model, *Atmos. Chem. Phys.,* 11, 3263-3280, doi:10.5194/acp-11-3263-2011, 2011.

Su, L., and O. B. Toon, Radiative effects of Asian dust on climate investigated with an integrated microphysical-climate-radiation model, *in preparation for the Journal of Atmos. Chem. Phys,* 2012.

Takemura, T., T. Nakajima, O. Dubovik, B. N. Holben, and S. Kinne, Single scattering albedo and radiative forcing of various aerosol species with a global three-dimensional model. *Journal of Climate*,15, 333-352, 2002.

Tegen, I., and I. Fung, Modeling of mineral dust in the atmosphere: Sources, transport, and optical thickness, *J. Geophys. Res.*, 99, 22,897–22,914, 1994.

Tegen and R. Miller, A GCM study on the interannual variability of soil dust aerosol. *Journal of Geophysical Research* **103**, pp. 25975–25995, 1998.

Toon, O. B., and T. P. Ackerman, Algorithms for the calculation of scattering by stratified spheres, *Appl. Opt.* 20, 3657- 3660, 1981.

Toon, O. B., R. Turco, D. Westphal, R. Malone, and M. Liu, A multidimensional model for aerosols: Description of computational analogs, *J. Atmospheric Science*, 45, 2123, 1988.

Toon, O.B.: African dust in Florida clouds, Nature 424, pp. 623–624, 2003.

Tratt, D. M., R. J. Frouin, and D. L. Westphal, April 1998 Asian dust event: A southern California perspective, *J. Geophys. Res.,* 106(D16), 18,371–18,379, 2001.

Uno, I., et al., Regional chemical weather forecasting using CFORS: Analysis of surface observation at Japanese Island Station during the ACE-Asia experiment, *J. Geophys. Res*., 108(D23), 8668, doi:10.1029/2002JD002845, 2002.

Uno, I., et al., Numerical study of Asian dust transport during the springtime of 2001 simulated with the Chemical Weather Forecasting System (CFORS) model, *J. Geophys. Res*., 109, D19S24, doi:10.1029/2003JD004222, 2004.

Uno, I., K. Harada, S. Satake, Y. Hara, and Z. Wang , Meteorological Characteristics and dust distribution of the Tarim Basin simulated by the nesting RAMS/CFORS dust model*, J. Meteorol. Soc. Jpn.*, 83A, 219–239, 2005.

Uno, I., et al., Dust model intercomparison (DMIP) study over Asia: Overview, *J. Geophys. Res*., 111, D12213, 2006.

Uno, I., Yumimoto, K., Shimizu, A., Hara, Y., Sugimoto, N., Wang, Z., Liu, Z., and Winker, D. M.: 3D structure of Asian dust transport revealed by CALIPSO lidar and a 4DVAR dust model, Geophys. Res. Lett., 35, L06803, doi:10.1029/2007GL032329, 2008.

Uno et al.: Asian dust transported one full circuit around the globe, Nature Geoscience 2, 557-560, doi:10.1038/ngeo583, 2009.

VanCuren, R. A., Asian aerosols in North America: Extracting the chemical composition and mass concentration of the Asian continental aerosol plume from long-term aerosol records in the western United States, J. Geophys. Res., 108(D20), 4623, 2003.

Warner, T. T., 2004 *Desert Meteorology*, Cambridge University Press, 620 pp. Warner, T. T., Desert Meteorology, *Cambridge University Press*, 620 pp, 2004.

Westphal, D. L., O. B. Toon, and T. N. Carlson, A case study of mobilization and transport of Saharan dust. *J. Atmos. Sci.*, 45, 2145-2175, 1988.

Winker, D. M., Pelon, J. R., and McCormick, M. P.: The CALIPSO mission: Spaceborne lidar for observation of aerosols and clouds, Proc. SPIE, 4893, 1–11, 2003.

Winker, D. M., Pelon, J., Coakley, J. A., Ackerman, S. A., Charlson, R., Colarco, P. R., Flamant, p., Fu, Q., Hoff, R. M., Kittaka, C., Kubar,. T. L., Le Treut, H., MvCormick, M. p., Megie, G., Poople, L., Powell, K., Trepte, C., Vaughan, M. A., Wielicki, B. A.: The CALIPSO mission: a global 3D view of aerosols and clouds. Bull. Amer. Meteor. Soc. vol. 91 (9) pp. 1211-1229, 2010.

Winker, D. M., Hunt, W. H., and McGill, M. J.: Initial performance assessment of CALIOP, Geophys. Res. Lett., 34, L19803, doi:10.1029/2007GL030135, 2007.

Wu, L.: Impact of Saharan air layer on hurricane peak intensity, Geophys. Res. Lett., 34, L09802, doi:10.1029/2007GL029564, 2007.

Wurzler, S., T. G. Reisin, and Z. Levin, Modification of mineral dust particles by cloud processing and subsequent effects on drop size distributions, *J. Geophys. Res.,* 105(D4), 4501–4512, 2000.

Yin, Y., Levin, Z., Reisin, T. G., and Tzivion, S.: The effects of giant cloud condensation nuclei on the development of precipitation in convective clouds: A numerical study, Atmos. Res., 53, 91–116, 2000.

Young, S., Winker, D., Vaughan, M., Hu, Y., Kuehn, R.: Extinction Retrieval Algorithms, CALIOP algorithm theoretical basis document PC-SCI-202 Part 4, Available on http://www.calipso.larc.nasa.gov/resources/pdfs/PC-SCI-202_Part4_v1.0.pdf, 2008.

Zender, C. S., B. Huisheng, and D. Newman, Mineral dust entrainment and deposition (DEAD) model: Description and 1990s dust climatology. *J. Geophys. Res.*, 108(D14), 4416, 2003a.

Zeng, X., and R. E. Dickinson, Effect of surface sublayer on surface skin temperature and fluxes, J. Climate, 11, 537-550, 1998.

Zeng, X., M. Zhao, and R. E. Dickinson, Intercomparison of bulk aerodynamic algorithms for the computation of sea surface fluxes using TOGA COARE and TAO data, *J. Climate,* 11, 2628-2644, 1998.

Zhang, L., S. Gong, J. Padro, and L. Barrie, A size-segregated particle dry deposition scheme for an atmospheric aerosol module, *Atmos. Environ.*, *35*, 549–560, 2001.